WITS
UNIVERSITY

A geological assessment of selected South African concrete aggregates susceptible to alkali-silica reaction

Sivuyile Mkhondweni

Student number:1854115

Supervisors:

Dr. Nonkuselo Madlakana

Prof. Yunus Ballim

A Dissertation submitted to the Faculty of Science, University of the Witwatersrand, Johannesburg, in fulfilment of the requirements for the degree of Master of Science in Geology

10 December 2024

Johannesburg, South Africa

Declaration

I, ___Sivuyile Mbasa Mkhondweni___ (_____1854115_____) am a student registered for _____Master of Science (Dissertation)____ in the year ___2024____. I hereby declare the following:

 I am aware that plagiarism (the use of someone else's work without their permission and/or without acknowledging the source) is wrong.

 I confirm that the work submitted for assessment for the above course is my own unaided work except where I have explicitly indicated otherwise.

 I have followed the required conventions in referencing the thoughts and ideas of others.

 I understand that the University of the Witwatersrand may take disciplinary action against me if there is a belief that this is not my own unaided work or that I have failed to acknowledge the source of the ideas or words in my writing.

Signature:  Date: _____10/12/2024_____

Abstract

Concrete deterioration is one of the biggest concerns in civil and environmental engineering, as it affects the service life of concrete structures. While the sources of concrete deterioration vary, this study focuses on alkali-silica reaction (ASR). ASR is a chemical reaction that can lead to cracking and loss of material integrity. Given the nature of concrete manufacturing and the mechanism of ASR, studying rocks as aggregate is critical for understanding aggregate behaviour in concrete. In South Africa, many concrete structures have been reported to be affected by ASR; however, the reasons behind these effects are not well understood. Additionally, there is a scarcity of geological assessments of South African concrete aggregates concerning ASR. Therefore, the potential impact of petrographic studies on our understanding of ASR in South Africa has led to this research investigation.

This study focuses on seven selected aggregate samples used in South African concrete. The materials were sampled from known quarries around South Africa due to suspected or reported ASR (to varying degrees) in the use of the aggregates. A geological assessment of these aggregates and their constituent minerals at a microscopic level was performed using optical microscopy, X-ray diffraction (XRD), and Tescan Integrated Mineral Analyzer (TIMA). The results of these assessments were compared with the expansion behaviours exhibited by the aggregates during the Accelerated Mortar Bar Test (SANS 6245). The findings reveal that rocks containing high silica concentrations, an abundance of microcrystalline and strained polycrystalline quartz, the presence of microcracking, and intense undulatory extinction of quartz crystals were more expansive. Specifically, the Witwatersrand quartzite and metashale, the Dwyka tillite, and the Malmesbury feldspathic metawacke exhibited expansions greater than 0.1% on day fourteen, indicating potential alkali reactivity. In contrast, the Natal arkosic sandstone and Cape Granite Suite monzogranite, which showed expansions less than 0.1% on day fourteen, were defined by non-reactive silica and medium-grained quartz crystals with minimal microcracking and no deformation features. Although undulatory extinction is globally recognised as an important indicator of ASR susceptibility, this study suggests it cannot be solely relied upon. Instead, a combination of high crystalline lattice distortion, high reactive silica concentrations, the presence of microcracking, and increased surface area of quartz grains is necessary for the occurrence of ASR. The study emphasises the importance of careful selection of concrete aggregates to avoid using potentially alkali-reactive rocks. These results provide valuable insights for engineers and geologists on suitable aggregates for concrete production. If the use of potentially alkali-reactive rocks is unavoidable, mitigation strategies such as using supplementary cementitious materials, a less alkali-rich cement, and a low water/cement ratio should be implemented. In conclusion, integrating geological techniques such as optical microscopy, XRD, and TIMA is essential for a comprehensive understanding of aggregate behaviour in concrete and accurate ASR susceptibility and expansion prognosis. This research contributes to the

limited geological assessments of South African concrete aggregates and the approaches employed make it a first-of-its-kind investigation regarding their susceptibility to ASR.

Acknowledgement

I am overwhelmed with emotions as I write this part because it makes it all real. I would love to firstly, give all the glory to my Lord and personal Saviour, Jesus Christ, for carrying me through my studies. His love, grace, providence, and guidance held me together. I would love to also express my deepest gratitude to parents, family, and loved ones for their prayers, words of encouragement, and endless support. I would like to thank Tirisano Construction for funding my studies, AfriSam, and OMV Stilfontein Crushers for providing the aggregate and rock samples, this project would not have been possible without their generous support. I will forever be grateful.

Secondly, I would like to express the most profound appreciation to my supervisors, Prof. Yunus Ballim and Dr. Nonkuselo Madlakana, for their tireless support and encouragement. Their constructive feedback, expert advice, and trust in my capabilities have been indispensable in shaping the direction of my work and have changed how I view myself as an academic. My heartfelt appreciation goes to Ms. Janina Kanjee, for her unwavering guidance, continuous support, and constructive feedback throughout my studies. To Prof. Mark Alexander, from the University of Cape Town, thank you for your expert advice and shared wisdom.

My special thanks to Mr. Louis Mudalahothe, Mr. Sam Tshabalala, and Mr. Caiphas Majola, from the School of Geosciences, for their support in thin section preparation for both microscopy and TIMA analysis. I would like to thank Prof. Grant Bybee, for his assistance with the calibrations of the Wits Imaging and Microscopy Lab, as well as Dr. Stephanie Enslin for her supportive words during my studies.

I would like to extend my sincerest gratitude to Mr. Ronny Lambani, Mr. Sam, Mr. Chris Nethononda, and Ms. Namhla Maqubela, from the School of Civil and Environmental Engineering, for their assistance in conducting the Accelerated Mortar Bar Test, your continued support through my studies will forever be appreciated. To Ms. Elizabeth Simelane, thank you for always ensuring that I had all I needed for my studies, and for your endless encouragement and jokes, I am beyond grateful.

Many thanks to Ms. Ayesha Jogee for assistance with the Wits Imaging and Microscopy Lab, and to Mr. Borbor Gibson for assistance with the TIMA analysis in the Wits Automated Mineralogy Lab.

Table of contents

List of figures

List of tables

List of abbreviations

AMBT	Accelerated Mortar Bar Test
Ab	Albite
AAR	Alkali-Aggregate Reaction
ACR	Alkali-carbonate reaction
ASR	Alkali-silica teaction
Ap	Apatite
Bt	Biotite

Fsp	Feldspar
Fm	Formation
Mc	Microcline
Mg	Magnesium
Ms	Muscovite
Or	Orthoclase
Pl	Plagioclase
PPL	Plain Polarized Light
Qtz	Quartz
SEM	Scanning Electron Microscopy
Ser	Sericite
TIMA	Tescan Integrated Mineral Analyzer
Wits	Witwatersrand
XPL	Cross Polarised Light
XRD	X-ray Diffraction
XRF	X-ray Fluorescence

Chemical formulas

Al	Aluminium
Ca	Calcium
Fe	Iron
K	Potassium
Mg	Magnesium
Na	Sodium
S	Sulphur
Si	Silicon

CHAPTER ONE

1. Introduction

Concrete deterioration is a major concern in civil and environmental engineering, as it affects the service life of concrete structures (Woodson, 2009; Prasad, 2023). The compromise to the durability and functionality of these structures give rise to safety concerns and leads to costly repairs. As a result, when addressing concrete deterioration, the adage 'prevention is better than cure' holds true (Ben Haha, 2006; Rajabipour *et al*., 2015). While the sources of concrete deterioration are diverse, alkali-silica reaction (ASR) has become one of the globally recognised cause. ASR is a reaction that occurs internally in concrete between cement and certain aggregates, in the presence of moisture. This reaction results in the loss of material integrity, thereby compromising the serviceability and durability of concrete structures (Oberholster, 1966; Ben Haha, 2006; Woodson, 2009). Due to the utilisation of aggregates in concrete and the mechanism of ASR, understanding aggregates at a microscopic level is crucial for comprehending aggregate behaviour in concrete and determining their potential susceptibility to ASR (Rajabipour *et al*., 2015; Leeman *et al*., 2016). In South Africa, many concrete structures are reported to have been affected by ASR. Therefore, the main focus of this thesis is to conduct a geological assessment of selected South African aggregates and their constituting minerals at a microscopic level (Rajabipour *et al.*, 2015; Fernandes *et al*., 2016; Geng *et al*., 2021).

Concrete is a composite material composed of aggregates bonded together with cement and water, which sets and hardens over time (Neville and Brooks, 1987; Woodson, 2009). It is an essential building material widely utilised in construction, including bridges and highways, dams, and buildings (Neville and Brooks, 1987; Crow, 2008; Woodson, 2009; Owens, 2013; Gu *et al*., 2016). This composite material is designed to withstand different structural loads (dead, live, wind, service, tension, and shear loads) and harsh environmental conditions, provided that it remains intact and resists deterioration (Neville and Brooks, 1987; Beushausen and Alexander, 2009; Gu *et al*., 2016). Despite its excellent properties, many concrete structures exhibit signs of deterioration caused by various mechanisms like weathering, erosion, and chemical reactions (Neville and Brooks, 1987; Woodson, 2009). One of the chemical reactions, known as ASR, has received significant attention for causing severe internal deterioration in concrete (Gillot 1995; Beushausen and Alexander, 2009; Blight and Alexander, 2011; Leeman *et al*., 2016; De Grazia *et al*., 2021).

ASR results in the formation of a secondary mobile product called alkali-silica gel (Blight and Alexander, 2011; De Grazia *et al*., 2021; Milanesi *et al*., 2021). This gel often swells in the presence of moisture,

generating internal expansion pressure in concrete, leading to cracking and loss of material integrity (Kawamura and Iwahori, 2004; Werner *et al.*, 2015; Geng *et al.*, 2021; Gholizadeh-Vayghan and Rajabipour, 2021). Thus, understanding ASR allows for the development of adequate mitigation strategies to ensure the long-term performance of concrete.

As mentioned, numerous concrete structures in South Africa are reported to be affected by ASR (Oberholster, 2009; Sims and Poole, 2017). However, the understanding of why these structures are affected is limited. Additionally, there is a scarcity of geological assessments of South African concrete aggregates in terms of ASR. Therefore, the potential impact of petrographic studies on our understanding of ASR in South Africa has given rise to this research investigation. The aim of this dissertation is to conduct geological assessments using integrated techniques (optical microscopy, Tescan Integrated Microscopic Analysis, and X-ray Diffraction Analysis) to study aggregates known to be susceptible to ASR, and to gain geological insights into the characteristics that make them susceptible. The aggregate samples collected for assessment were sampled from the quarries indicated in Figure 1.1.

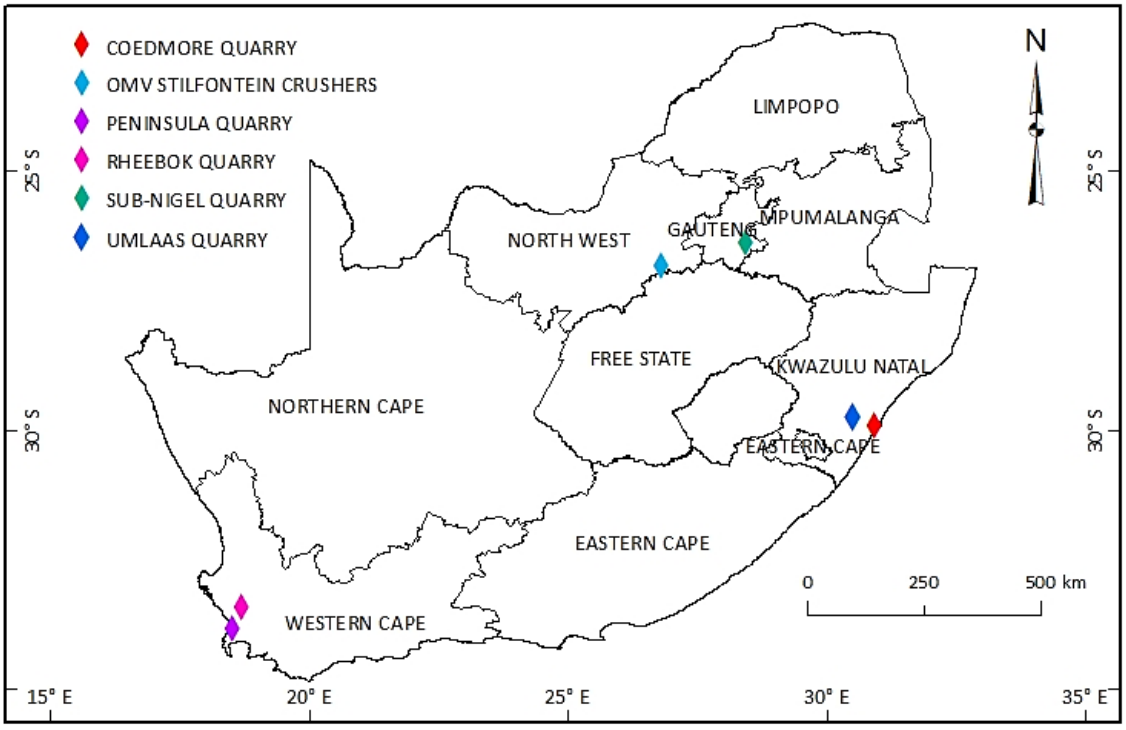

***Figure 1.1**: A map of South Africa showing the location of the quarries, within different provinces, where the aggregate samples used for this research were sampled.*

1.1. Problem statement

ASR is a phenomenon that has increased over the years and its occurrence impedes the longevity of infrastructure. Thus, understanding the susceptibility of different aggregate types is extremely

important in order to mitigate against it. Therefore, this research intends to determine whether geological assessments can predict aggregate susceptibility to ASR.

1.2. Hypothesis

Given that aggregates play a significant role in the occurrence of ASR, it is hypothesised that petrographic studies of the selected aggregates, using geological assessments, provide insight into aggregate susceptibility to ASR.

1.3. Aims and objectives

The general aim of this project is to adopt a geological approach using integrated techniques such as optical microscopy, TIMA, and XRD, to gain insights into ASR. This aim will be achieved through the following objectives:

- Determine the types of aggregates by defining and differentiating their mineral and chemical compositions as well as textures via petrography, XRD, and TIMA.
- Determine the porosity of aggregates via petrography.
- Correlate Accelerated Mortar-Bar Test (AMBT) results to geological characteristics

1.4. Dissertation structure

This section outlines the structure of the dissertation. The thirteen chapters that make up this dissertation include (Figure 1.2):

Chapter 1: an introductory section which provides the study's brief background, highlights the need for the research, contextualises the key concepts of ASR in South Africa and briefly explains the approach that will be taken to conduct this investigation.

Chapter 2: details the literature review.

Chapter 3: details the methods employed to conduct this research.

Chapters 4-9: focus on each aggregate. The chapters will begin with the aggregate's origin (geological setting), followed by the study area, (the quarry where the aggregate was sampled from). The results (hand specimen, optical microscopy, TIMA, and XRD observations as well as AMBT results) are also presented. Following, are two discussion sections looking at the geological characteristics and classification as well as the expansion results for the aggregate. Lastly, a closure section, which briefly summarises the chapters main findings.

Chapter 10: is a discussions section which compares the aggregates' expansion test results against their microscopic characteristics. It also discusses the aggregates use for construction projects.

Chapter 11: summarises the findings of this research to determine if the research aim was met.

Chapter 12: provides recommendations and future research possibilities.

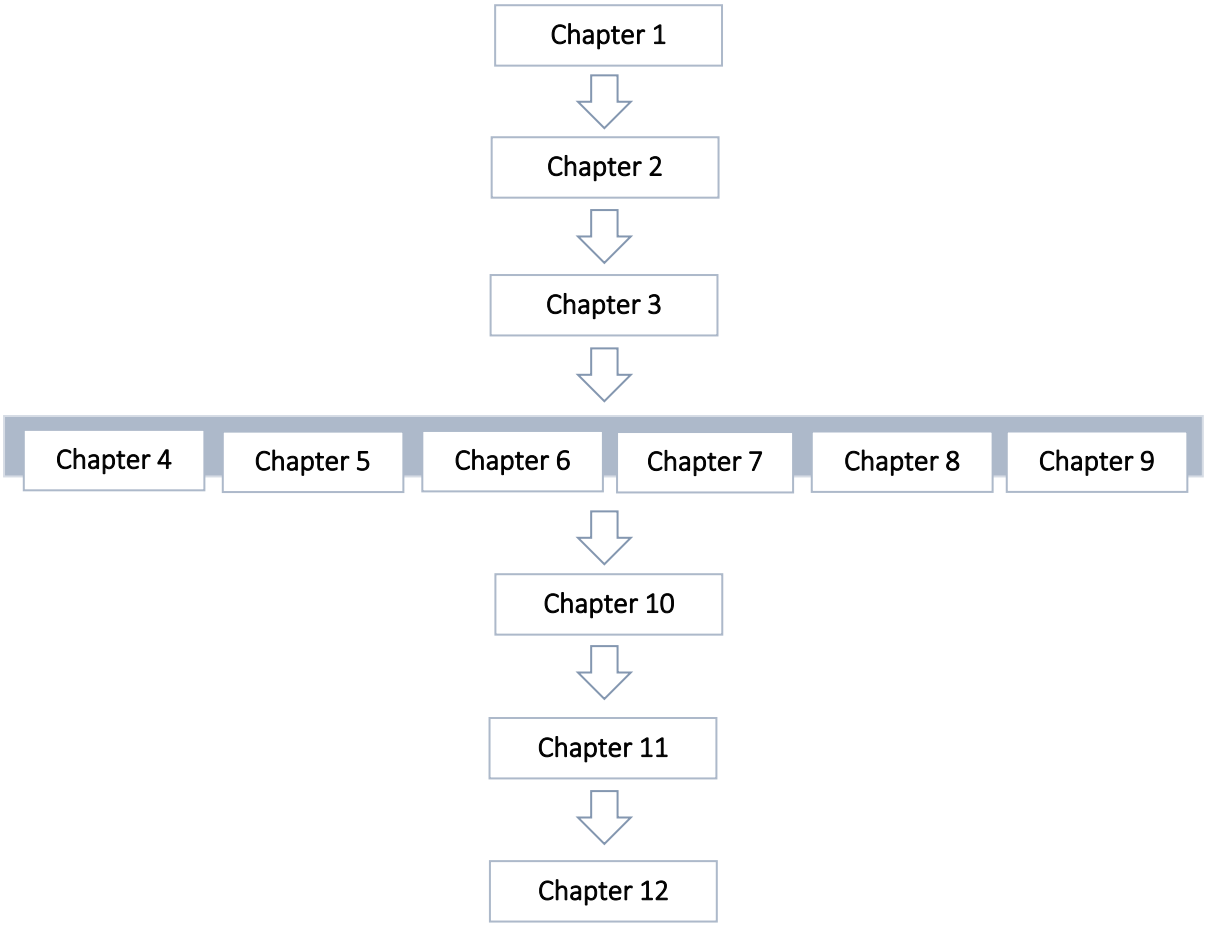

***Figure 1.2**: The structure of the dissertation.*

CHAPTER TWO

2. Literature Review

2.1. Cement-based construction materials

Cement is commonly defined as an adhesive substance that binds sand and gravel, forming concrete. Its composition typically includes limestone, clay, silica, sand, and seashells (Neville and Brooks, 1987; Woodson, 2009; Owens, 2013; Ley, 2018; Beaulieu, 2022). The type of cement selected is based on the desired rate of strength development, the potential chemical attacks, the aggressiveness of the environment, and the structural performance expectations of the concrete (Neville and Brooks, 1987; Owens, 2013). Amongst various types of cementitious materials, Portland cement is the most widely used in construction works (Neville and Brooks, 1987; Woodson, 2009; Ley, 2018). Portland cement is primarily composed of lime, silica, alumina, and iron oxide, which interact to produce a series of more complex products (Neville and Brooks, 1987). In addition to the main compounds, Portland cement contains minor compounds namely, MgO, TiO_2, MnO, K_2O, and Na_2O (Table 2.1) (Neville and Brooks, 1987). Two compounds, in the cement, Na_2O and K_2O, known as alkalis, have been discovered to react with some aggregates, causing concrete disintegration and influencing the cement's rate of strength gain (Neville and Brooks, 1987).

Table 2.1: Approximate composition limits of Portland cement (adapted from Neville and Brooks, 1987).

Oxides	*CaO*	*SiO*	*Al_2O_3*	*Fe_2O_3*	*MgO*	*Alkalis*	*SO_2*
Concentration per cent	60-67	17-25	3-8	0.5-6.0	0.1-4.0	0.2-1.3	1-3

Portland cement is a hydraulic substance that undergoes setting and hardening when mixed with water (Neville and Brooks, 1987; Woodson, 2009). Although considered to be a generic material, when hydrated, cements with different chemical compositions can exhibit distinct properties (Neville and Brooks, 1987; Park *et al*, 2024). There are a variety of Portland cement commercially available (Table 2.2) however the most used is Ordinary Portland (Type I) cement (Neville and Brooks, 1987; Park *et al*, 2024). In contrast to cement is mortar, a blend of cement, water, and fine sand (Ben Haha, 2006). It is commonly used as a binding material in construction involving bricks, stone, and blocks (Ben Haha, 2006). Although mortar shares similarities with concrete, concrete exhibits superior durability (Ben Haha, 2006).

Table 2.2: Summary of the Portland cement types and their distinctive characteristics (adapted from Neville and Brooks, 1987).

Cement Type	*Characteristics*
Ordinary Portland (Type I) cement	-The most common cement used in general concrete construction -Free CaO content 0.8 per cent
Rapid-Hardened Portland (Type III) cement	-Similar to Type I, however, strength develops rapidly as compared to Type I -Is not used in mass concrete structures -Free CaO content is 1.3
Low-Heat Portland (Type IV) cement	-Mainly used in gravity dams -Has a low-heat hydration -Free CaO content is 0.3 per cent
Modified (Type II) cement	-Recommended use is in structures where moderate low heat is generated -Free CaO content is 0.6
Sulfate-Resisting (Type V) cement	-Is a low-heat cement, used in specific instances -Free CaO content is 0.4 per cent
Portland Blast-Furnace (Type IS0 cement	-Similar to Type I however differs in early strength (associated to the differing compositions) -Is made from blending Portland cement with granulated blast-furnace slag
Portland-Pozzolan (Type IP, P And I) cement	-Is made from blending pozzolans with cement. -It gains strength slowly thus, requires long period to cure
White And Coloured Portland cement	-Is made from China clay and contains low amounts of Fe_2O_3 and MnO

2.2. Concrete

2.2.1. What is concrete?

Concrete is a building material consisting of Portland cement, aggregate, and water (Neville and Brooks, 1987; Gu *et al*., 2016). Beyond its basic components, the intricate particle arrangement within concrete, characterised by a densely packed structure, significantly contributes to its inherent strength and durability (Cheng *et al*., 2021). The relationship between cement and concrete, results in the concrete inheriting the chemical properties of the cement, as outlined in Table 2.1 (Gu *et al*., 2016). The curing process, a critical aspect of concrete development over time, involves carefully controlling conditions such as temperature and humidity. This influences the formation of a strong crystalline matrix, enhancing concrete's overall strength and durability (Gu *et al*., 2016).

Concrete exhibits a natural strength in compressive force but is relatively weak in tensile force (Neville and Brooks, 1987; Gu *et al*., 2016), and to address this limitation, reinforcement is commonly introduced, often in the form of steel bars. The incorporation of steel enhances the concrete's tensile strength and resistance to external forces, giving rise to reinforced concrete structures (Woodson, 2009; *Gu et al*., 2016). Engineered to be a versatile and robust construction material, concrete finds application in various structural elements, including beams, slabs, columns, foundations, and walls. Moreover, the use of admixtures in concrete mixes can further modify its properties, with chemicals added to accelerate or retard the setting time, providing adaptability to specific construction needs (Figure 2.1) (Neville and Brooks, 1987; Woodson, 2009; Gu *et al.,* 2016).

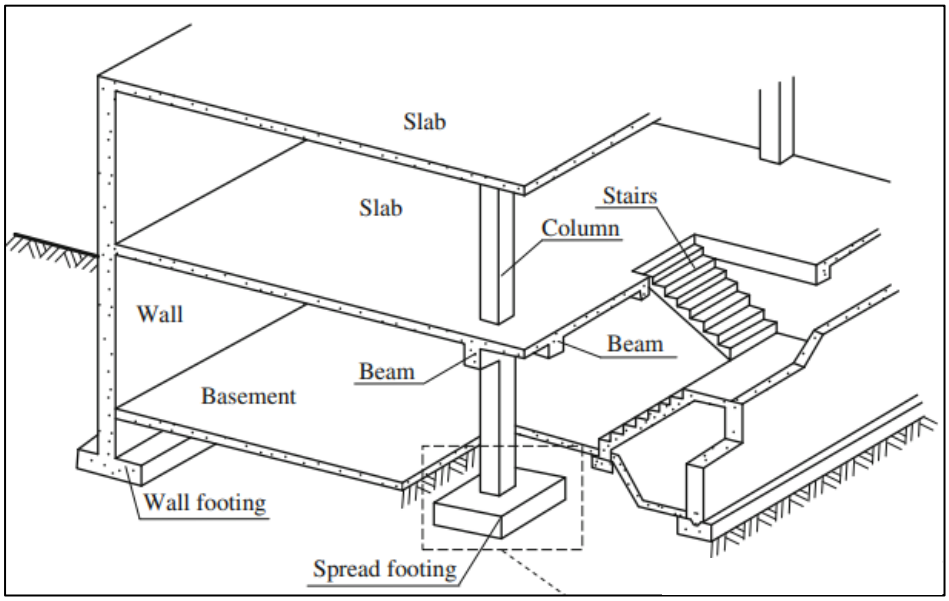

Figure 2.1*: Concrete members in a multistorey reinforced concrete building (modified Gu et al., 2016).*

2.2.1.1. Concrete aggregates

Aggregates account for three-quarters of the volume of concrete and are mainly used to lower the cost of concrete and improve the dimensional stability of cured concrete (Owens, 2013). Although a diverse range of aggregates are used (Table 2.3), the quality of the aggregate is critical as it affects concrete workability (Oberholster *et al*., 1978; Neville and Brooks, 1987; Grieve, 2009; Owens, 2013). Aggregates were initially considered to be inert however it is now known that some aggregates are reactive in concrete (Grieve, 2009). This is because aggregates are characterised by physical, thermal, and chemical properties that influence concrete performance (Neville and Brooks, 1987). The properties that aggregate have in concrete depend on the properties of the parent rock such as the mineral and chemical composition, chemical stability, and pore structure (Grieve, 2009; Owen, 2013). Therefore, the study of rock properties prior to concrete production has been encouraged by several scholars, in order to use more appropriate rocks as aggregate when manufacturing concrete (Oberholster *et al*., 1978; Neville and Brooks, 1987; Grieve, 2009).

Concrete aggregates are partitioned into two categories- coarse aggregates (or stone) and fine aggregates (or sand) (Grieve, 2009). Furthermore, the choice of aggregates differs with country, for example, the aggregate choice in Germany differs from the aggregate choice in South Africa.

Table 2.3: Rock classifications of natural aggregates used in concrete (Oberholster et al., 1978; Neville and Brooks, 1987).

Basalt Group	Flint Group	Gabbro Group	Granite Group	Gritstone Group	Quartzite Group
Andesite	Chert	Hornblende-rock	Gneiss	Arkose	Quarzitic sandstone
Basalt	Flint	Gabbro	Granite	Greywacke	Quartzite
Dolerites		Serpentinite	Syenite	Sandstone	
		Basic diorite	Quartz-diorite	Tuff	
		Norite	Granodiorite		

2.2.1.2. Quarrying of concrete aggregates

The supply of aggregates for concrete production and other uses is achieved through quarrying (Naidoo, 2008; Hustrulid, 2023). Quarrying is surface (or open pit) mining where dimension stone, rocks, concrete aggregates, sand, gravel, or slate are extracted from the ground intended for the utilisation in construction (Naidoo, 2008; Hustrulid, 2023). Quarrying holds economic importance as it is the foundation for infrastructure development and the construction industry (Naidoo, 2008). Although quarrying is a subset of the mining industry, it is fundamentally distinct from mining (Naidoo, 2008). This is because quarrying is done on the exposed surface of natural rock, whereas mining is the extraction of minerals in rocks, done on the surface or underground (Naidoo, 2008). Quarrying can take place in open pits or waste dumps and often involves drilling and blasting before extracting the rock with bulldozers and draglines (Naidoo, 2008; Hustrulid, 2023). The fractured rock is then transported to a processing facility, where it goes through multiple phases of crushing and sizing (Figure 2.2) (Naidoo, 2008). A good concrete aggregate must be clean, chemically inert, durable, hard, homogeneous, rounded to cubic after crushing, and of the appropriate size grade to produce the required physical properties (Naidoo, 2008; Owens, 2013). In South Africa, numerous quarry products are available, and products such as concrete aggregate may be found in abundance near most of the country's major towns (Naidoo, 2008). Quarry products are mostly used in the construction of monuments, buildings, roads, and bridges (Naidoo, 2008)

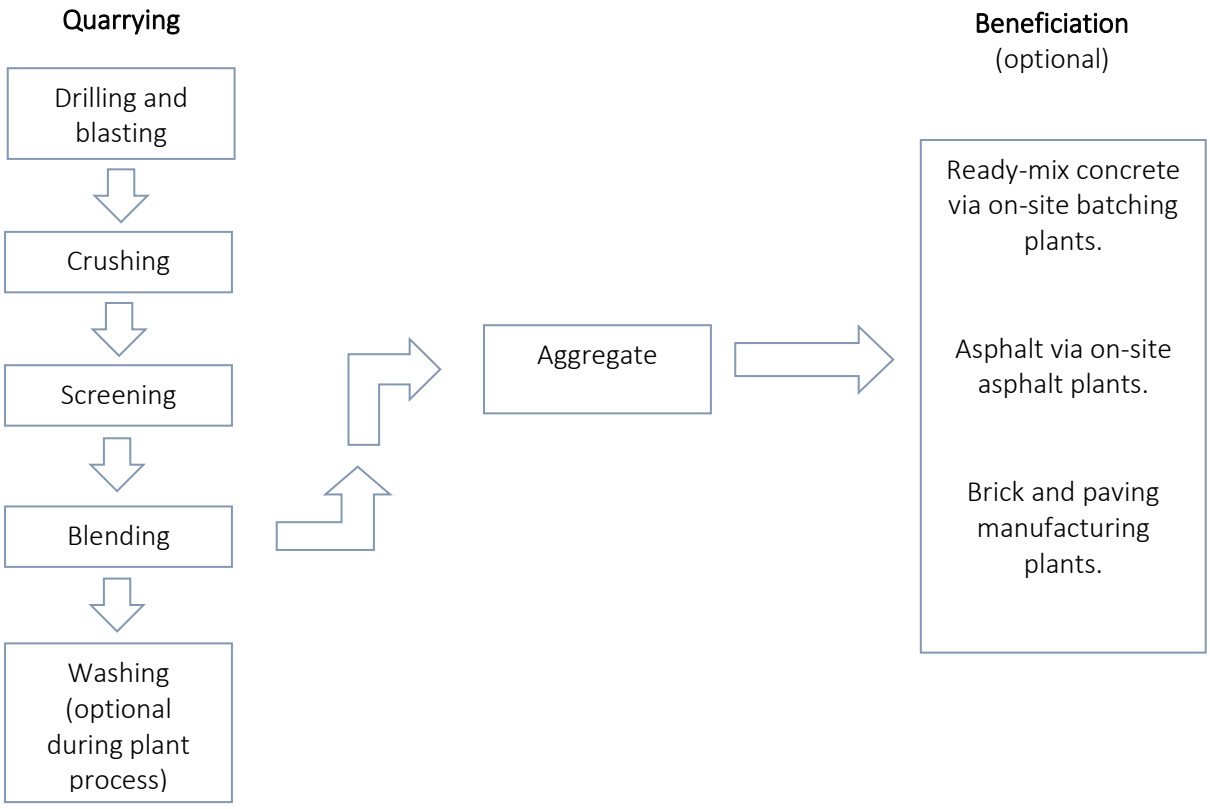

***Figure 2.2**: A systematic diagram showing the value chain of quarrying in South Africa. Initial drilling and blasting of aggregate, followed by crushing, screening and blending. Washing the blended aggregate may be conducted however is not compulsory. Once the blending has occurred, the aggregate be used in a variety of plants (modified Naidoo, 2008).*

2.2.1.3. South African concrete aggregates

In South Africa, the coarse aggregates used in concrete production are mainly derived from solid rock which differ in origin and in type, as included in Table 2.4 (Grieve, 2009). The fine aggregates are dominantly sand from sand dunes however they may also include crushed fragments of the coarse aggregates (Grieve, 2009). Additionally, the fine aggregates vary with location (Grieve, 2009). For example, most of the fine aggregate used in Gqeberha is crusher sand from the Table Mountain Group quartzite whereas in East London, it is metamorphosed quartz-feldspar sandstone from the Adelaide Subgroup (Grieve, 2009).

***Table 2.4**: South African aggregates (coarse) and their source (Grieve, 2009).*

Aggregate	*Origin*
Quartzite and sandstone	Witwatersrand Supergroup; Table Mountain Group
Basic igneous rock (dolerite, gabbro, norite, basalt, and andesite)	Various origins
Granite	Cape Granite Suite
Greywacke	Malmesbury Group
Tillite	Dwyka Group
Miscellaneous (dolomite and felsite)	Various origins

2.2.2. Causes of deterioration and distress of concrete

The bond between aggregate and cement paste determines concrete performance (Neville and Brooks, 1987; Woodson, 2009). Concrete is known for its strength, durability, and resistance and so when these characteristics are compromised through various processes, it raises a call for concern (Neville and Brooks, 1987; Woodson, 2009; Gu *et al*., 2016). Many factors could lead to concrete deterioration and distress such as weathering, corrosion, chemical reactions, and several others noted in Table 2.5 (Neville and Brooks, 1987; Woodson, 2009). Although the results of deterioration and distress are mainly characterised by cracking, the cause of cracking differs, for example chemical reactions, freezing and thawing, and erosion are said to result in the disintegration of concrete whereas corrosion results in spalling (Woodson, 2009; Ley, 2019). Literature proposes that many of the causes of concrete deterioration are also interlinked, whereby one mechanism may initiate another. For example, weathering, the process that involves the breaking down or dissolving of rocks and minerals (Blight and Alexander, 2011), can give rise to secondary or tertiary minerals in aggregates. These minerals may be undesirable in concrete such as active clay minerals, which may on the contrary, be suitable for initiating chemical reactions such as ASR. ASR may subsequently, widen crack widths through expansive gel which may allow for the seepage of fluids through concrete and reaching the reinforcement, thus triggering corrosion (Ben Haha, 2006; Woodson, 2009; Blight and Alexander, 2011; Ley, 2019).

Table 2.5: *A table showing a variety of causes of deterioration and distress in concrete (modified Woodson, 2009).*

Causes of deterioration and distress in concrete	*Examples*
Accidental loading	-
Chemical reactions	Alkali-silica reaction, alkali-carbonate rock reaction, acid attack, aggressive-water attack, sulphate attack, aggressive-water
Construction errors	-
Corrosion of embedded metals	-
Design errors	Poor design details, inadequate structural design
Erosion	Abrasion, cavitation
Freezing and thawing	-
Settlement and movement	-
Shrinkage	Plastic, drying
Temperature changes	Internally generated, externally generated, fire
Weathering	-

2.2.3. Alkali Aggregate Reaction

Alkali-Aggregate Reaction (AAR) is a chemical process that occurs when alkalis in the cement paste react with certain minerals in the aggregate, causing severe deterioration to concrete structures (Blight and Alexander, 2011; Leeman *et al*., 2016; De Grazia *et al*., 2021). The phenomenon of AAR was first noticed in the United States in the 1920s and was officially identified in engineering literature by Stanton in 1941 (Oberholster *et al.,* 1978; Blight and Alexander, 2011; Fernandes *et al*., 2016). Since the 1970s, AAR has received significant attention globally in terms of public awareness and research investment (Gillot, 1995; Blight and Alexander, 2011). To initiate and sustain the phenomenon, sufficient moisture is required, and it can cause substantial damage to concrete structures (Blight and Alexander, 2011). This damage can manifest as both micro- and macro-cracking in the matrix and the aggregates, as well as weakening the bond to reinforcement (Kawamura and Iwahori, 2004; Blight and Alexander, 2011; Werner *et al*., 2015). The external effects of AAR are often unsightly and alarming, with surface cracking, and the crack widths possibly exceeding 10 mm (Gillot, 1995; Blight and Alexander, 2011). Although cracking typically becomes evident several years after construction, any crack is a reason for concern and warrants a thorough investigation (Blight and Alexander, 2011, Kurtis *et al.*, 2017).

AAR has two main forms: alkali-silica reaction (ASR) and alkali-carbonate reaction (ACR) (Gillot, 1995; Fernandes *et al*, 2016; Ley, 2019; Gholizadeh-Vayghan and Rajabipour, 2021; Milanesi *et al*., 2021).

2.2.4. Alkali carbonate reaction

Alkali carbonate reaction (ACR) is a less common type of AAR (mainly encountered in Canada), and its distress mechanism is still enigmatic (Blight and Alexander, 2011; Ley, 2019). However, it is believed that ACR is a reaction between alkalis and certain types of dolomitic rock in concrete (Blight and Alexander, 2011). According to Blight and Alexander (2011), ACR occurs when carbonate rocks are used in concrete and undergo a process known as dedolomitization, which results in the formation of brucite and calcite. The alkali carbonates formed during the dedolomitization process may react with Portlandite from the cement paste to form secondary calcite and regenerate alkali hydroxides, suggesting that ACR might be an endless process (Blight and Alexander, 2011). ACR does not produce a gel (Leeman *et al.,* 2016, Fernandes *et al*., 2016).

2.2.5. Alkali-silica reaction

A large proportion of literature shows that ASR is well understood and several scholars, define ASR as a mechanism that negatively affects the durability and performance of concrete (De Ceukelaire, 1991; Blight and Alexander, 2011; Werner, 2015; De Grazia *et al*., 2021). ASR is a chemical reaction between alkali hydroxides (OH^-, K^+, Na^+) from the cement paste, soluble silica present in large quantities in the aggregate and water (Hobbs, 2002: Fernandes *et al*., 2016; Ley, 2019; De Grazia *et al*., 2021). This

reaction forms a secondary product called alkali-silica gel via the following reaction (Werner, 2015):

$$SiO_2 + 2Na(OH) + 2H_2O = Na_2H_2SiO_4 \bullet 2H_2O.$$

All three components need to be sufficiently present for the alkali-silica gel to form and additional space (pore spaces) is required for the gel to expand in the presence of moisture (Werner, 2015).

2.2.5.1. Dissolution of soluble silica

The initial phase in causing ASR damage is the dissolution of metastable silica (Kao, 2016; Liaudat, 2018; Mohamed, 2018). Silicates, a type of metastable silica, are common minerals found in Earth's rocks (Mohamed, 2018). These are mostly made up of three-dimensional tetrahedral silica units, with one Si atom surrounded by four oxygen atoms (Kao, 2016; Liaudat, 2018; Mohamed, 2018). The units are connected by siloxane bonds that use oxygen vertices, also known as bridging oxygens (Kao, 2016; Liaudat, 2018). The angle of the Si-O-Si bond between SiO_2 tetrahedra can vary, resulting in macro-crystalline, micro-crystalline, or amorphous silica structures (Mohamed, 2018). In alkaline environments, hydroxyl (OH^-) ions can easily attack the ≡Si-O- bonds as opposed to the Si-O-Si bond (Kao, 2016; Liaudat, 2018; Mohamed, 2018). This causes network dissolution of the silica, resulting in the formation of $Si(OH)_4$ ions, and at a high pH, $Si(OH)_4$ ions ionise and become highly soluble (Kao, 2016; Liaudat, 2018; Mohamed, 2018). Ion exchange reactions also typically occur to reduce the pH of the pore solution, for example, ions such as Na^+ may be bound in the reaction products however, and some of the alkalis in the gel can be replaced by Ca^{2+} ions (Kao, 2016; Liaudat, 2018; Mohamed, 2018). This process is known as alkalis recycling (Kao, 2016; Liaudat, 2018; Mohamed, 2018).

2.2.5.2. Alkali-silica reaction products: chemical composition and crystalline structure

ASR is a reaction between alkalis ($Na_2O + K_2O$) and silica (Si_2O) that produces an ASR product (Ben Haha, 2006). This ASR product is chemically composed of silicon, alkalis, and calcium, with minor aluminium, iron, and magnesium (Ben Haha, 2006; Leeman *et al*., 2016). Once the reaction has been initiated, the initial reaction products typically form a rim around the aggregate edge (Ben Haha, 2006; Leeman *et al*., 2016). However, there are two types of ASR products: at the edge of the aggregate and in the aggregate core (Leeman *et al*., 2016). Leeman *et al*. (2016) state that ASR products in the aggregate core are mostly crystalline whereas ASR products at the edge and in cement paste cracks and voids are amorphous. It is said that these two types are chemically distinguishable, with one type having the calcium content of ASR products increasing towards the edge of the aggregate, whereas with the other the alkali content often decreases (Leeman *et al*., 2016).

2.2.5.3. The effects of alkali-silica reaction

ASR is a destructive mechanism that attacks concrete when it occurs (Ben Haha, 2006). It is said that ASR decreases the compressive and tensile strength, the fatigue strength, and the elastic modulus of

concrete (Ben Haha, 2006; Yegon, 2019). It also creates the expansion of concrete structures which causes internal microcracking, which manifests as macrocracking on exposed surfaces (Figure 2.3). The cracking allows for other chemical reactions such as sulphate attacks and chloride attacks to occur thus reducing durability (Ben Haha, 2006; Ley, 2019; Yegon, 2019). The external effects of ASR are often evident through surface cracking, gel weeping, and white staining (Figure 2.3A-D) (Gillot, 1995; Woodson, 2009; Werner *et al.,* 2015). Cracking that exceeds 2.03 mm is categorised as wide thus crack widths that greatly exceed this number such as in Figure 2.3B, warrant investigations.

Figure 2.3: *A) Concrete structure subjected to ASR showing sizeable cracks and white staining below cracks (efflorescence) (Werner et al., 2015). B) Cracking (up to 15 mm wide) of the south abutment bridge near Wits Yale/Empire Road entrance, Johannesburg (photo courtesy Y. Ballim). C) Map cracking of the North abutment M1 bridge on Empire Road, Johannesburg, Gauteng (photo courtesy Y. Ballim). D) ASR damaged structure at weir, Western Cape (photo courtesy of Y. Ballim).*

2.2.5.4. Alkali-silica reaction in South Africa

ASR in South Africa was initially reported in 1974 by Oberholster and Brandt whereby a cement-aggregate reaction in a concrete structure in the Cape Peninsula, was observed (Oberholster *et al*., 1978). Since then, numerous concrete structures (Figure 2.3B-D) have been reported to be affected by ASR (Oberholster *et al*., 1978; Alexander and Blight, 2017). A significant portion of the literature indicates that enough is known about the phenomenon (in South Africa) to reduce the risk of ASR in new structures (Oberholster, 1996). However, the susceptibility of different South African concrete

aggregates to ASR is not well understood and thus the literature on the diagnosis of ASR is quite limited. As a result, this study adds to the limited knowledge available about South African concrete aggregates.

Surface cracking on concrete is an undesirable indication of the deteriorating condition that the concrete is in, and the cracking of the concrete structures shown in Figure 2.3B-C exceeds the 2.03 mm width threshold and thus warrants investigation.

2.2.5.5. Assessment of alkali-silica reaction

2.2.5.5.1. Physical-field assessment

Field investigations are the first step in ASR assessments (Beushausen and Alexander, 2009; Woodson, 2009; Blight and Alexander, 2011). ASR can be physically identified by map cracking, gel weeping, and white stains on the surface of the concrete (Figure 2.3C-D) (Beushausen and Alexander, 2009; Woodson, 2009; Blight and Alexander, 2011). However, further laboratory assessment is needed to investigate the magnitude of ASR within concrete (Blight and Alexander, 2011).

2.2.5.5.2. Laboratory assessment

A systematic procedure is important for an accurate investigation of ASR-affected concrete. Many scholars have stated that three procedures are necessary to determine whether cracks in concrete are ASR-related or not (Figure 2.4) (Blight and Alexander, 2011; Fernandes *et al*., 2016). The initial screening test, consisting of a petrographic examination of aggregates- has been known as an essential part of understanding ASR (Blight and Alexander, 2011; Werner, 2015; Fernandes *et al*., 2016). This procedure includes a microscopical study of the minerals that comprise the aggregates used in concrete and enables the categorisation of these aggregates in terms of their alkali-reactivity (Table 2.6) (Blight and Alexander, 2011; Fernandes *et al*., 2016). Additionally, it allows one to see ASR at a more microscopic scale. The success of the initial screening test requires the use of optical microscopy, XRD, and other appropriate techniques to examine and quantify the presence of deleterious components (Blight and Alexander, 2011; Werner, 2015).

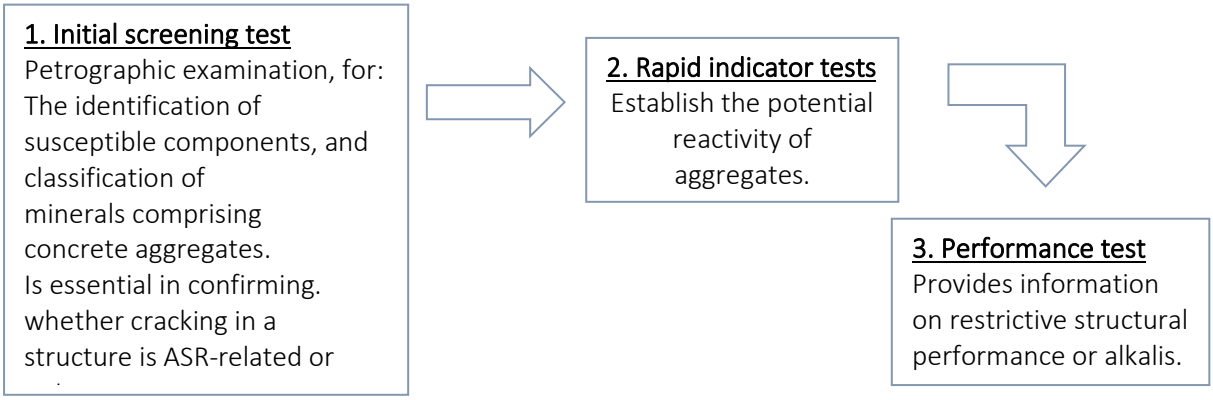

Figure 2.4*: Schematic showing the three procedures required in ASR investigation (adapted and modified Blight and Alexander, 2011).*

Table 2.6: Classification of aggregate alkali-reactivity) (Fernandes et al., 2016).

	Alkali- Reactivity	*Examples*
Class I	Very unlikely	Unstrained quartz
Class II	Potentially or reactive uncertain	Wide range, including shale, quartzite, tillite and greywacke
Class III	Very likely	Opal, opaline silica

2.2.5.6. Initial screening test: petrographic and other geological assessments of alkali-silica reaction-susceptible aggregates

Literature regarding ASR-related studies has collectively highlighted the importance of the use of geological assessments in ASR investigations (Gillot, 1995; Nayal and Singh, 2007; Fernandes *et al*., 2016; Fanijo *et al*., 2021; Venyite *et al*., 2022; Antio *et al*., 2023). The geological assessments which are generally used include, microscopy (optical microscopy and SEM) and XRD with less XRF and TIMA (Gillot, 1995).

Microscopy: Optical Microscopy

Optical microscopy is one of the most used techniques in ASR-susceptible aggregate investigations (Fernandes *et al*., 2016; Fanijo *et al*., 2021; Venyite *et al*., 2022). This analysis has enabled researchers to study and determine the constituents of aggregates, identify the mineralogy of the aggregate, and evaluate ASR reactivity (Fernandes *et al.,* 2016; Fanijo *et al*., 2021; Venyite *et al*., 2022). It has allowed for the identification of selected characteristic forms and textures of silica that appear to be susceptible to alkalis such as strained quartz (undulatory extinction and deformation lamellae) (Figure 2.5A-B), subgraining and recrystallisation (Figure 2.5C-D) (Fernandes *et al.,* 2016; Fanijo *et al*., 2021; Venyite *et al*., 2022).

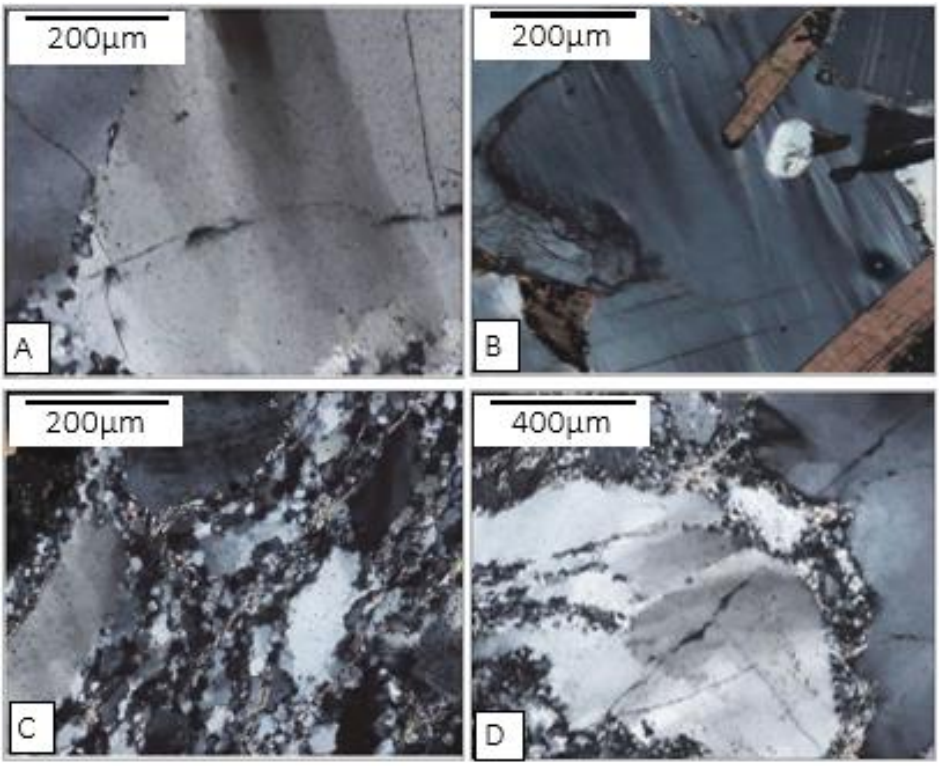

Figure 2.5: *Image showing different textures of quartz crystals observed under the microscope in XPL. A) Undulatory extinction of quartz crystal. B) Deformation lamellae on quartz crystal. C) Sub-graining and recrystallisation on quartz boundary. D) Re-crystallisation is evident on the quartz boundary (Fernandes et al., 2016).*

Microscopy: Scanning Electron Microscopy

Scanning Electron Microscopy (SEM) is another commonly used analysis in ASR-susceptible aggregate investigations (Fernandes *et al*., 2016; Fanijo *et al*., 2021; Venyite *et al*., 2022). This technique is efficient for analysing organic and inorganic materials at the nm to µm range by focusing and scanning materials with a low-energy electron beam (Mohammed and Abdullah, 2018). Although SEM can be employed for geological material, literature on the use of SEM in ASR investigations is mainly used to study the composition, distribution, and micromorphology of ASR as opposed to the microscopic characteristics of the aggregate rock before the reaction (Bektas and Wang, 2012; Fernandes *et al.,* 2016; Mohammed and Abdullah, 2018; Wu *et al*., 2020; Fanijo *et al*., 2021).

X-ray Diffraction Analysis

X-ray Diffraction (XRD) is another geological technique that has been employed to conduct ASR-related investigations (Dähn *et al*., 2016). XRD is used to characterise the mineral phases in aggregates by recording mineral peaks (Ben Haha, 2006; Dähn *et al*., 2016; Venyite *et al.,* 2022). Academics such as Cole and Lancucki, (1983) and Venyite *et al*. (2022) conducted studies which used XRD. Cole and Lancucki (1983) employed XRD to identify crystalline ASR products from an Australian dam and the study revealed that ASR products have different peaks when wet versus when dry. Venyite *et al.* (2022)

used XRD to determine the mineralogical and microstructural characteristics of aggregates, and this study revealed that minerals such as biotite, and pyrite are also alkali reactive.

X-ray Fluorescence Analysis

X-ray Fluorescence (XRF) is an analytical technique commonly used to determine the chemical composition of the mineral present in rocks (Brouwer, 2006; Nayal and Singh, 2007; Venyite *et al*., 2022), and scholars such as Dähn *et al*. (2016) and Antio *et al*. (2023) adopted this technique to conduct aggregate investigations. Dähn *et al*. (2016) used XRF to locate the reaction products formed in veins within the concrete aggregate and XRF showed that ASR products have higher Ca concentrations than the alkalis (Na + K). Antio *et al*. (2023) conducted a study to investigate the potential alkali-silica reactivity of selected Namibian aggregates, and his study revealed that an elevation in SiO_2 concentration in aggregate resulted in a corresponding elevation in the susceptibility to ASR and the percentage expansion.

TESCAN Integrated Mineral Analyser

TIMA is an automated system which has gained attention in geological research because of its distinct capabilities, high level of automation, specialised hardware, and software integration which are applicable for geological applications (Hrstka *et al.,* 2018). TIMA has enabled the visualisation and quantification of petrological features- such as alteration, fractures, deformation re-crystallisation, inclusion distribution mapping, exsolution structures, and contact zones- of rocks and other materials (Hrstka *et al*., 2018). It has also identified mineral species and properties (Hrstka *et al.,* 2018). Literature on TIMA as one of the techniques used in geological research is quite accessible however is limited in ASR-related research.

2.2.5.7. Rapid indicator test

The potential alkali reactivity of siliceous aggregates can be determined using various methods, including the accelerated mortar bar test, concrete prism test, quick chemical test, and gel pat test (Oberholster and Davies, 1986).

2.2.5.7.1. Gel Pat Test

The Standard Gel Pat Test (BS 7943) is a preliminary screening test, designed to detect the presence of microcrystalline, cryptocrystalline, highly strained, and microcracked quartz in just three days (Oberholster and Davies, 1986; Lanza and Alaejos, 2012). Though the test previously occurred at low temperatures, the standard test's effectiveness was improved by raising the storage temperature to 80°C to accelerate the chemical reactions (Lanza and Alaejos, 2012). The test is conducted by casting a "pat" sample with many voids between the aggregate particles to facilitate gel accumulation (Lanza and

Alaejos, 2012; Munir *et al*., 2018). If the aggregates are reactive at the end of the third day, gels form on the surface of the pat and fill the voids (Oberholster and Davies, 1986; Lanza and Alaejos, 2012). A visual inspection of gel growth can also be used to distinguish between slow and fast reactive aggregates and reactive particles can be identified and easily removed from the pat (Lanza and Alaejos, 2012; Munir *et al*., 2018).

2.2.5.7.2. Quick Chemical Test

The Quick Chemical Test, ASTM C 289, is one of the quickest of the methods used, taking only one day to complete (Munir *et al*., 2018). The test measures the amount of dissolved reactive silica by sealing crushed material in a 1N NaOH solution at 80˚C for 24 hours (Munir *et al.*, 2018). The results obtained then classify the aggregate source as reactive or nonreactive (Munir *et al*., 2018). However, using this method, some quartz-bearing rocks (such as greywacke, granite, and quartzite) which have a track record of being deleteriously reactive, typically obtain results that classify them as non-deleterious (Oberholster and Davies, 1986).

2.2.5.7.3. Concrete Prism Test

The Concrete Prism Test, ASTM C 1293, is an internationally recognised indicator test used for determining the potential alkali-silica reactivity of aggregate in concrete (Ideker *et al.*, 2010; Munir *et al*., 2018). In the test, concrete specimens, stored in water at 35 +/-2˚C or 60 +/-2˚C, are periodically measured for expansion over 52 weeks (Ideker *et al.*, 2010; Munir *et al*., 2018). From the test, potentially reactive aggregates have an expansion limit of >0.04% after 365 days (Table 2.7) (Oberholster and Davies, 1986; Ideker *et al.*, 2010).

Table 2.7: Expansion criteria for ASTM C 1293 (Ideker et al., 2010).

Expansion (%)	*Aggregate interpretation*
<0.04%	None-reactive aggregate
>0.04%	Reactive aggregate

2.2.5.7.4. Accelerated Mortar Bar Test

The Accelerated Mortar Bar Test (AMBT), also known as SANS 6245 (South African standard), ASTM C 1260 (American standard) or AAR.2, is a globally accepted indicator test known to differentiate between deleterious, potential, and innocuous aggregates through monitoring the expansion of mortar specimens (Ideker *et al.*, 2010; Alexander and Blight, 2017; Munir *et al*., 2018). Test aggregates are contained within the mortar specimens, and the mortar specimens are immersed in a 1M NaOH solution at 80˚C (Oberholster and Davies, 1986; Ideker *et al.*, 2010; Munir *et al*., 2018). The specimens are then monitored for 12-14 days (Ideker *et al.*, 2010; Munir *et al*., 2018). According to this method,

specimens with an expansion of 0.1% after 14 days are considered to be potentially reactive, as classified in Table 2.8 (Oberholster and Davies, 1986).

Table 2.8: Expansion criteria for AMBT (SANS 6245 or ASTM C1260) (adapted from Oberholster and Davies, 1986; Alexander and Blight, 2017).

Expansion (%)	*Aggregate interpretation*
<0.1%	None-reactive aggregate
0.1-0.2%	Potentially reactive or slowly reactive
>0.2%	Reactive aggregate

2.2.6. Aggregates known to be associated with alkali-silica reaction

The type of silica (reactive or non-reactive) within concrete aggregates is crucial in ASR (Ben Haha, 2006). The degree of crystallinity determines whether silica will dissolve, and disordered silica seems to be the accepted criteria for silica to be part of ASR. (Blight and Alexander, 2011; Fernandes *et al*., 2016; Leeman *et al.,* 2016). Minerals known to be reactive include opal; cristobalite; tridymite; chalcedony; cryptocrystalline, microcrystalline, or glassy quartz; intensely fractured coarse-grained quartz; granulated and strained internally coarse-grained quartz or coarse-grained quartz rich in secondary inclusions and siliceous, intermediate, and basic volcanic glasses (Oberholster *et al*., 1978; Hobbs, 2002; Leeman *et al.,* 2016, Fernandes *et al*., 2016). The typical rocks in which these reactive minerals occur are greywacke, volcanic rocks, quartzite, granite, phyllite, and hornfels (Oberholster *et al*., 1978; Hobbs, 2002; Ben Haha, 2006; Leeman *et al.,* 2016, Fernandes *et al*., 2016). Defects, such as mechanical deformation and chemical impurities introduced during growth, in the quartz crystalline structure, promote dissolution (Leeman *et al*., 2016). It has been emphasised that rocks which are siliceous in character are not automatically reactive unless the silica within them is alkali-reactive (like those listed above) (Hobbs, 2002; Leeman *et al.,* 2016). In addition, aggregate size and porosity contribute to reactivity (Neville and Brooks, 1987; Blight and Alexander, 2011; Fernandes *et al*., 2016). For example, fine aggregates are more likely to facilitate the reaction than coarse aggregates, and more porous aggregates will allow for alkali attack to occur throughout the particle as opposed to less porous aggregates (Neville and Brooks, 1987; Blight and Alexander, 2011).

2.2.7. Mineral associated with alkali-silica reaction

Literature regarding ASR-related studies reveals that quartz is the primary mineral in aggregates that contribute to ASR in concrete. Quartz is a tectosilicate mineral, classified under the silica group (Klein, 2003). It has a framework of tetrahedra in which Si and each of the four oxygen anions are shared with another tetrahedra (Klein, 2003; Science First, 2017). The bond between Si-O is both ionic and covalent thus making quartz strong and difficult to break, however, its crystalline structure can be displaced and deflected through tectonic stresses (Law, 1986; Klein, 2003; Fernandes *et al*., 2016; Leeman *et al.,*

2016). Tiecher *et al*. (2018) stated that the displacement of quartz's crystalline structure changes the distances between its atoms, resulting in "fragile zones" that tend to subdivide and create new grains due to increased internal stresses. The displaced quartz crystalline structure is observed as undulatory extinction under an optical microscope (MacKenzie *et al*., 2017). Therefore, the degree of undulatory extinction in quartz can be used to determine how much displacement has occurred, and thus how potentially reactive an aggregate can be (Blight and Alexander, 2011; Fernandes *et al*., 2016; Leeman *et al.,* 2016; Tiecher *et al*, 2018).

2.2.8. South African aggregates known to be potentially susceptible.

Not all aggregates used in concrete are innocuous nor are they all reactive however aggregate origin promotes ASR susceptibility (even of the same type) (Oberholster, 2009). For example, a Witwatersrand quartzite is more susceptible to ASR than a Natal Group quartzite (Oberholster, 2009). A study conducted by Oberholster (2009) as well as Fernandes *et al*. (2016) whereby they identified reactive South African aggregates (Table 2.9) enabled concrete manufacturers to be cautious when choosing concrete aggregate.

Table 2.9*: South African aggregates known to be susceptible (modified: Oberholster 2009; Fernandes et al., 2016).*

	Geological origin	*Reactive examples*
Western Cape	Malmesbury Group	hornfels, sandstone, lava, spotted hornfels, quartzite, meta-greywacke, mylonite
	Cape Supergroup	orthoquartzite (Table Mountain Group = TMG) arkose (Bokkeveld Group)
Eastern Cape	Quaternary Period	river gravels
	Cape Supergroup	orthoquartzite (TMG)
	Enon Formation	quartzite pebbles
	Quaternary Period	quartzite pebbles
Gauteng and Free State	Witwatersrand Supergroup	quartzite and shale
Mpumalanga	Archean	granite, gneiss
KwaZulu Natal	Natal Group	-
Others		felsic porphyry, granofels, and calc-silicate

2.2.9. Mitigating against alkali-silica reaction

The process of repairing concrete necessitates a higher level of experience and expertise compared to installing new concrete structures (Blight and Alexander, 2011; Rajabipour *et al.*, 2015). As a result, mitigating against ASR requires experience and expertise (Rajabipour *et al.*, 2015; Ley, 2019). Repairing of damaged concrete structures is quite costly however the financial implication of poorly executed mitigation strategies is worse (Beushausen and Alexander, 2009). Thus, the best mitigation strategy is said to be prevention, however, other strategies have been presented. These strategies differ for new concrete versus existing concrete structures that already suffer from ASR (Oberholster *et al.,* 1978; Gillot, 1995; Blight and Alexander, 2011; Rajabipour *et al*., 2015).

Existing concrete

Remedial measures against ASR in existing concrete are limited, however it is suggested that the most adequate strategy is to avoid external water from penetrating through concrete by crack filing, as the closing of existing ASR-related cracks prevent further concrete deterioration (Oberholster *et al*., 1978; Gillot, 1995; Rajabipour *et al*., 2015). The use of vapour permeable membrane such as silane sealer or silicone sealer (Blight and Alexander, 2011; Ley, 2019). Another measure is to use a sealer which prohibits infiltration of external water while allowing water internally to be evaporated (Blight and Alexander, 2011; Ley, 2019). Improving drainage such as directing run-off water away from load-bearing members of bridge structures and fixing burst pipes (Rajabipour *et al*., 2015). Another strategy is to use extra reinforcement while partially or completely replacing damaged concrete with new concrete (Gillot, 1995).

New concrete

There have been several mitigation strategies, against ASR of new concrete, proposed in literature and these include using less alkali-rich cement by using Portland cement with a maximum alkali content of 0.6 per cent or supplementary cementitious materials with low CaO and low alkalinity (Blight and Alexander, 2011; Rajabipour *et al*., 2015; Ley, 2019). Using a combination of innocuous (non-reactive) aggregates (Oberholster *et al*., 1978; Blight and Alexander, 2011; Rajabipour *et al*., 2015; Ley, 2019). Using a low water/cement ratio, is important when making concrete because not only does it determine the strength of the concrete, but it also governs how the concrete will cure (Neville and Brooks. 1987; Ley, 2019). Another strategy is the use of supplementary cementitious material such as fly ash and slag (Neville and Brooks, 1987; Oberholster, 2009), the use of a 50/50 mix of ordinary Portland cement (Type I) and ground granulated blast furnace slag as well as the use of a mixture of ordinary Portland cement (Type I) and fly ash (Class F) that contains a minimum of 25% of fly ash (Neville and Brooks, 1987). An additional mitigation strategy is to add lithium compounds in the concrete mixture (LiOH, $LiCO_3$, and

$LiNO_3$) because lithium can decrease the dissolution rate of silica, impeding alkali-silica gel from forming, and altering the properties and expansion of alkali-silica gel when incorporated into alkali-silica gel (Oberholster, 2009; Rajabipour *et al*., 2015).

CHAPTER THREE

3. Methodology

This experiment involved the use of rock samples and aggregate. The materials were sampled from known quarries around South Africa due to suspected or reported ASR (to varying degrees) in the use of the aggregates. Secondly, this investigation intends to compare aggregates of the same type. The selected quarries include Sub-Nigel Quarry, Umlaas Quarry, Coedmore Quarry, Rheebok Quarry, Peninsula Quarry, and OMV Stilfontein Crushers. After collection and appropriate storage, the samples were transported to the University of the Witwatersrand, where tests and analyses such as the accelerated mortar bar test, TIMA analysis, XRD analysis, and optical microscopy were conducted.

3.1. Optical microscopy

Thin sections were prepared for the microscopic identification of minerals at the School of Geoscience at the University of the Witwatersrand, South Africa. Rock samples were sliced and mounted on a glass slide and polished to the appropriate thickness of 30 µm (Figure 3.1A). The samples were cut and trimmed into slabs appropriate for mounting using the cutting machine. The slabs were initially lapped and then ground progressively using 60, 120, 240, 400, 600, and 1200 grit sizes. Subsequently, the polished surfaces were mounted on glass slides using epoxy glue. Then, excess rock was cut using the thin section machine, and other surfaces were lapped on the grinding machine and prepared to the required 30 µm thickness.

The identification and documentation of modal abundance, mineral assemblages, textural characteristics, reactions textures, and cracks were conducted by using the Olympus microscope (Olympus TH4-200) (transitioning between Plain Polarised Light (PPL) and Cross Polarised Light (XPL)). Additionally, detailed microscopic images were captured using the Olympus SC50 camera (Figure 3.1B).

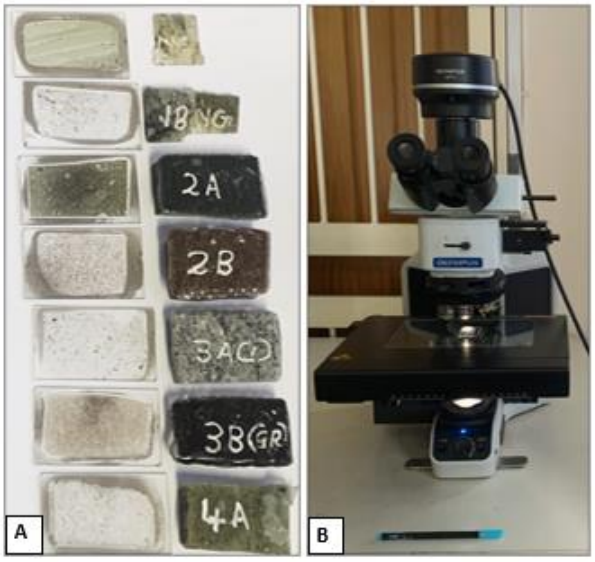

Figure 3.1: Image showing. A) Thin sections of rocks next to cut rock samples mounted on glass slides.1A= Witwatersrand shale, 1B (NG)= Witwatersrand quartzite, 2A= Dwyka tillite, 2B= Natal quartzite, 3A (1)= Cape Granite Suite granite, 3B (GR)= Malmesbury wacke, and 4A= Witwatersrand quartzite. B) Olympus Microscope with the Olympus TH4-200 and Olympus SC50 camera used for petrographic analysis and capturing petrographic images.

3.2. TESCAN Integrated Mineral Analyzer (TIMA) analysis

In this research, the characterisation of the different minerals present in the concrete aggregate rock samples was conducted using the Tescan VEGA's 3rd generation (VegaTCx64) Scanning Electron Microscope (SEM) and an EDAX Element 30 detector equipped with TIMA software version 2.9.0. Phase and elemental maps were quantified via energy-dispersive X-ray spectroscopy (EDS) using a VegaTCx64 Scanning Electron Microscope (SEM) and an EDAX Element 30 detector at the University of the Witwatersrand (Wamlab). The same SEM was utilised with TESCAN Integrated Mineral Analyzer (TIMA) software to complement transmitted light microscopy and aid in establishing the mineralogical composition of each sample.

TIMA is an automated system for rapidly analysing the mineralogical content of samples, utilising both EDS and Backscattered electron (BSE) signals to identify minerals. Additionally, TIMA measures the grain size distribution of minerals and generates high-resolution mineral images. The TIMA analysis was conducted after petrographic analysis, and the results from both transmitted light microscopy and TIMA were compared. Before data acquisition, the VegaTCx64 and the TIMA software were carefully calibrated to ensure accurate and reliable measurements. The beam conditions during quantitative analyses on the VegaTCx64 were 25 kV accelerating voltage, 17.0 beam intensity, 4.2 nA beam current, with a spot size of 533.62 nm, while maintaining a working distance of 15.00 mm. The scanning conditions on the TIMA software version 2.9.0 were set to RESOLUTION mode. The measurement type was specifically designed for liberation analysis, conducted through dot mapping acquisition mode with dot spacing adjusted to 20.00 µm and field width at 750 µm. While the pixel spacing was set at 4.00

µm, and x-ray counts at 1000. Further small scans were taken in high resolution acquisition mode with a field width of 1000 µ, pixel spacing set to 2.00 µm, and x-ray counts at 1000. The estimated acquisition time varied for each sample, with the total analysis time being approximately 25 hours.

3.3. X-ray diffraction (XRD) analysis

To conduct XRD analysis, each aggregate underwent a meticulous preparation process. Initially, each aggregate sample was crushed at room temperature using a Geo Crusher. Subsequently, the TS 250 Mill machine was used for milling, with each sample milled for at least 90 seconds, also at room temperature. Care was taken to prevent contamination by thoroughly cleaning the milling pot between samples. The pulverised material was transferred into a small, clean plastic bag for storage and submitted for XRD analysis at an external specialist testing facility.

For XRD analysis, a back-loading preparation method was employed on the pulverized samples. Diffractograms were obtained using a Malvern Panalytical Aeris diffractometer with a PIXcel detector and fixed slits with Fe-filtered Co-Kα radiation. Minerals were identified using X'Pert Highscore Plus software and PAN-ICSD. The relative phase amounts (in weight %) were estimated using the Rietveld method.

3.4. Expansion test: Accelerated Mortar-Bar Test (SANS 6245)

To conduct the AMBT test, each aggregate was meticulously prepared. Initially, aggregates were graded according to the grading requirements outlined in Table 3.1. The sieves used were from AAR.2 series B and had sizes of 4.75 mm, 2.36 mm, 1.18 mm, 600 µm, 300 µm, and 150 µm (Figure 3.2A). The dry aggregate particles were poured into the sieves with a pan at the bottom and then shaken for 10 minutes (Figure 3.2B). The particles retained on the 4.75 mm sieve and pan were discarded, while the content retained on the remaining sieves was stored in clean, well-labelled plastic bags. After an aggregate type was successfully graded and stored, the sieves were cleaned to prevent contamination. This process was repeated for all aggregate samples.

Table 3.1: Table displaying grading requirements for aggregates (SANS 6245).

Sieve sizes		*Mass %*
Passing	*Retained*	
4.75 mm	2.36 mm	10
2.36 mm	1.18 mm	25
1.18 mm	600 µm	25
600 µm	300 µm	25
300 µm	150 µm	10

In preparation for making mortar samples, mortar bar moulds sized, 160 mm x 40 mm x 40 mm were cleaned and lubricated with mould oil. 557.8 g of CEM I [5] plain Portland cement and 1300 g of graded aggregate were combined in a bowl, and the "dry" ingredients were thoroughly mixed. 225.1 g of water was then gradually added to the dry mix and mixed for 2-3 minutes until a uniform consistency was achieved (Figure 3.2C). The thoroughly mixed mortar was poured into three lubricated moulds and tampered for two minutes to compact it. Each mould was then labelled according to the quarry location and rock type (for example, RG= Rheebok granite, UT= Umlaas tillite, PG= Peninsula wacke) (Figure 3.2D) and left to cure for approximately 24 hours.

After 24 hours, the specimens were demoulded, and two Demec targets, 100 mm apart, were glued (as adhering to wet concrete) on each side of each specimen, indicated as A (side) and B (side). Once the targets were placed, the prisms were immersed in deionised water in a closed container that was heated in a water bath at a constant temperature of 80°C. After 24 hours in the water bath, the specimens were removed, and their strain was measured using gauge length (Figure 3.2E) with a 1 division = 2 x 10^{-5}. This reading served as the zero reading. Following the initial reading, the prisms were immersed in a 1M NaOH solution maintained at 80°C. The solution was kept in a securely sealed plastic container large enough to fully immerse the prisms (because the caustic solution corrodes glass and metal; plastic was used instead). The specimens were then measured daily for fourteen days. The strain measurements on each specimen–an average of the strain measurements on both sides–were recorded and subsequently converted into expansion percentages to create a time vs expansion graph:

$$Expansion = (D_n - D_0) \times (2 \times 10^{-5}) \times 100\%$$

D_n= the average division reading on the gauge measured on day n

D_0= the initial division reading on the gauge measured before being stored in NaOH solution

Gauge factor= 2 x 10^{-5}

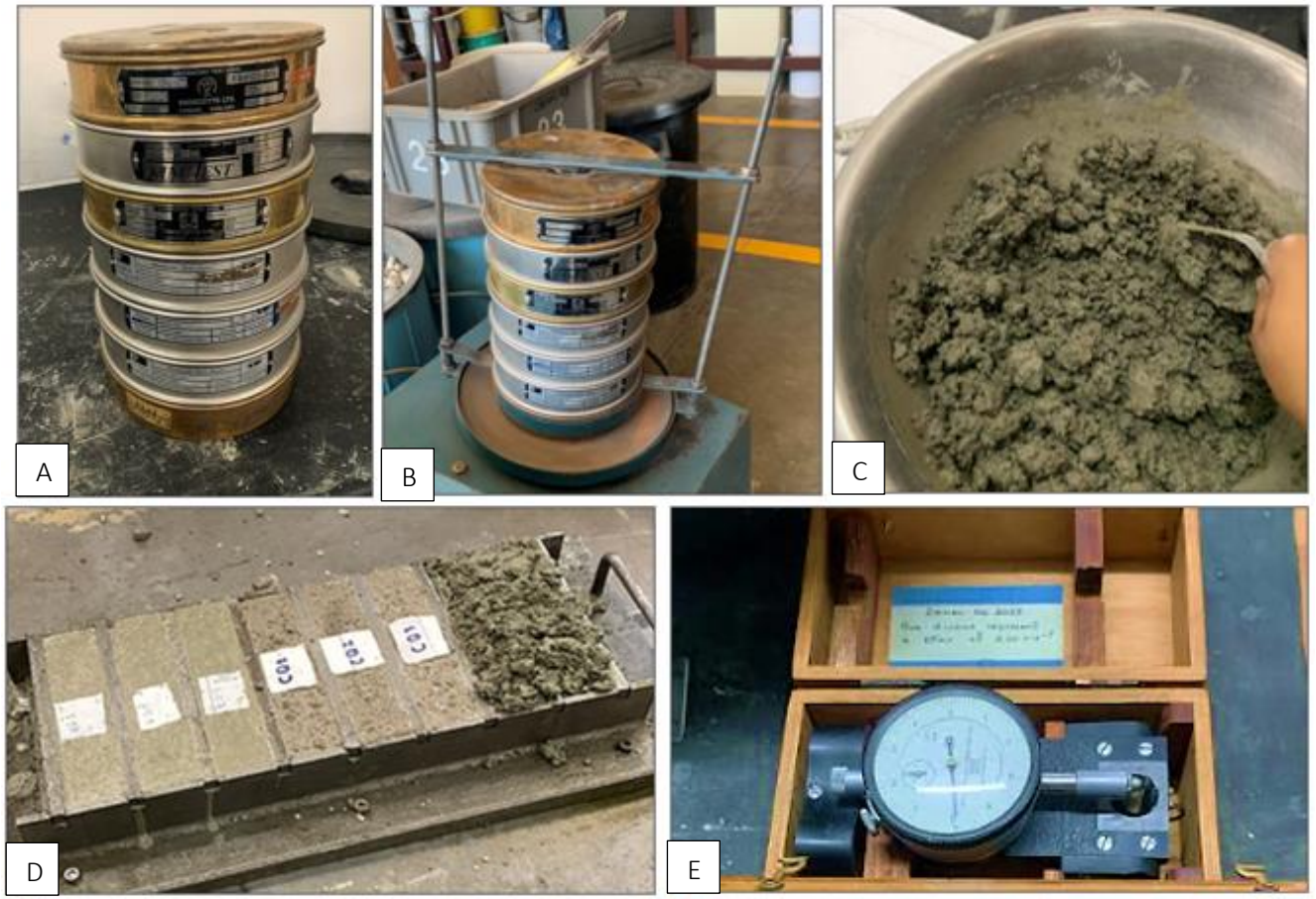

Figure 3.2: *Images obtained from SANS 6245 methodology. A) Sieves used to grade aggregate with the opening from 4.75 mm, 2.36 mm, 1.18 mm, 600 µm, 300 µm, and 150 µm according to SANS 6245. B) Sieves on the shaker are used to adequately grade the aggregates. C) Cement, aggregate, and water mixed well to produce mortar. D) Compacted mortar with labels after tampering. E) Demec gauge instrument used to measure strain (with a factor of 2 x 10 $^{-5}$).*

CHAPTER FOUR

4. The Witwatersrand quartzite (Randfontein Formation) and shale (Booysens Formation)

4.1. Geological setting

The Witwatersrand (Wits) Supergroup, famously known for being the world's largest gold repository, is a 2.9 Ga (billion year) old Archaean intracratonic sedimentary sequence that is located in the centre of South Africa's Kaapvaal Craton (Figure 4.1) (Robb and Meyer, 1995; McCarthy, 2006). The Witwatersrand basin formed as a result of a succession of crustal plate motions from the north and west in a foreland basin environment (McCarthy, 2006; Tucker *et al*., 2016). The deposition of this sedimentary sequence is described as gradual and associated with inland coastlines **(**McCarthy, 2006). This world-class gold-bearing basin was metamorphosed and reshaped by three major events, 1) lateral crustal movement, 2) the Vredefort meteorite impact, and 3) the emplacement of the Bushveld Complex (Robb and Meyer, 1995; Tucker *et al*., 2016). The first event caused severe folding and faulting along the northern and western regions of the basin (Robb and Meyer, 1995; McCarthy, 2006; Tucker *et al*., 2016). The second event resulted in the movement of fluids that penetrated the basin strata which led to pervasive metasomatic alteration (Robb and Meyer, 1995; McCarthy, 2006; Tucker *et al*., 2016). The third event resulted in the recrystallisation, alteration, and remobilisation of minerals due to extensive contact metamorphism (Robb and Meyer, 1995; McCarthy, 2006; Tucker *et al*., 2016). The Witwatersrand Supergroup is divided into the upper Central Rand Group and lower West Rand Group (Figure 4.1) (Tucker *et al*., 2016). The West Rand Group consists of quartzites, shale, and iron-rich shale horizons of shallow marine environments and is partitioned into three subgroups: Hospital Hill, Government, and Jeppestown Subgroup (Robb and Meyer, 1995; McCarthy, 2006; Tucker *et al*., 2016). The sequence which makes up the West Rand records a major marine transgression (McCarthy, 2006; Frimmel, 2019). Overlying the West Rand Group is the sequence of the Central Rand Group (Frimmel, 2019).

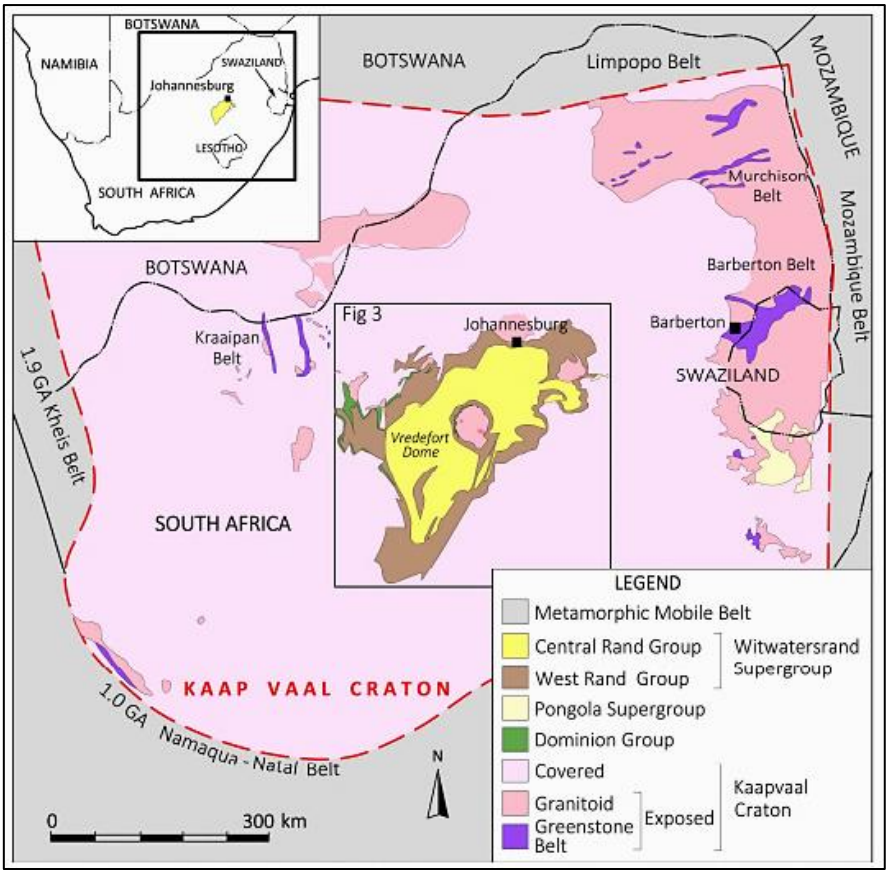

Figure 4.1*: Image showing the geological setting of the Witwatersrand Basin, in the central section of the Kaapvaal Craton, including the Limpopo, Mozambique, and Namaqua-Natal Mobile Metamorphic belts on the craton edge (Tucker et al., 2016).*

The Central Rand Group is an arenaceous succession composed of quartz-pebble conglomerates, quartzites, quartzwackes, and minor shales (Tucker *et al*., 2016; Frimmel, 2019). It displays deposition mostly under alluvial-braid-plain and minor alluvial fan conditions (McCarthy, 2006). This Group is split into two-fold subdivisions, the lower Johannesburg Subgroup and the upper Turffontein Subgroup (McCarthy, 2006; Tucker *et al*., 2016; Frimmel, 2019). The Turffontein Subgroup represents the final stage of sedimentation in the Wits Basin and is characterized by general upward coarsening caused by tectonics (McCarthy, 2006; Frimmel, 2019). This Subgroup is partitioned into the Mondeor Formation, Elsburg Formation, and Kimberly Formation (McCarthy, 2006; Frimmel, 2019). Prograding braid-plains gave rise to the basal Kimberly Formation, which coarsens upward and has multiple conglomeratic units (McCarthy, 2006; Frimmel, 2019). The Elsburg Formation is characterised by erosional reworking, whereas the upper Mondeor Formation was formed by alluvial fans that prograded into the basin (McCarthy, 2006; Frimmel, 2019). The Turffontein overlies the Johannesburg Subgroup (McCarthy, 2006; Frimmel, 2019).

The lower Johannesburg Subgroup of the Central Rand Group is quartzite dominant and was deposited in a fluvial braid-plain environment (McCarthy, 2006; Frimmel, 2019). This Subgroup is distinguished by

multiple cycles of degradation caused by either transgression or progradation of braid plains (McCarthy, 2006; Frimmel, 2019). The multiple cycles gave rise to the five formations found in this Subgroup, namely: the Main Formation, Randfontein Formation, Luipaardsvlei Formation, Krugersdorp Formation, and Blyvooruitzicht Formation (McCarthy, 2006; Frimmel, 2019). The basal Blyvooruitzicht Formation represents the first cycle, followed by erosive periods during transgression which resulted in the Main Formation, further cycles produced Randfontein Formation, Luipaardsvlei Formation, and Krugersdorp Formation (McCarthy, 2006; Frimmel, 2019). While the Krugersdorp Formation was being deposited, the Bird Member's lava eruption occurred (McCarthy, 2006; Frimmel, 2019). The volcanics of the Bird Member unit only developed over a portion of the basin from the West Rand eastwards (West Rand area to Evander area) (McCarthy, 2006; Frimmel, 2019). Toward the conclusion of the Krugersdorp Formation period, a basin extensive transgression occurred, during which shales of the Booysens Formation were deposited near the top of the Johannesburg Subgroup (McCarthy, 2006; Frimmel, 2019). Depositional conditions varied within the basin, resulting in regions with lithological variations (Table 4.1) (McCarthy, 2006; Frimmel, 2019). These variations gave rise to the eight areas of the Wits Supergroup, namely: the Welkom area, Klerksdorp area, Carletonville area, West Rand area, Central Rand area, South Rand area, Evander area, and East Rand area (Table 4.1) (McCarthy, 2006; Frimmel, 2019).

Table 4.1*: The stratigraphy of the Central Rand Subgroup and different areas with associated Formation (Fm) (the black areas indicate an absence of the Fm). The far right shows a simplified lithostratigraphy of the East Rand area in the Johannesburg Subgroup of the Central Rand Group (adapted from McCarthy, 2006).*

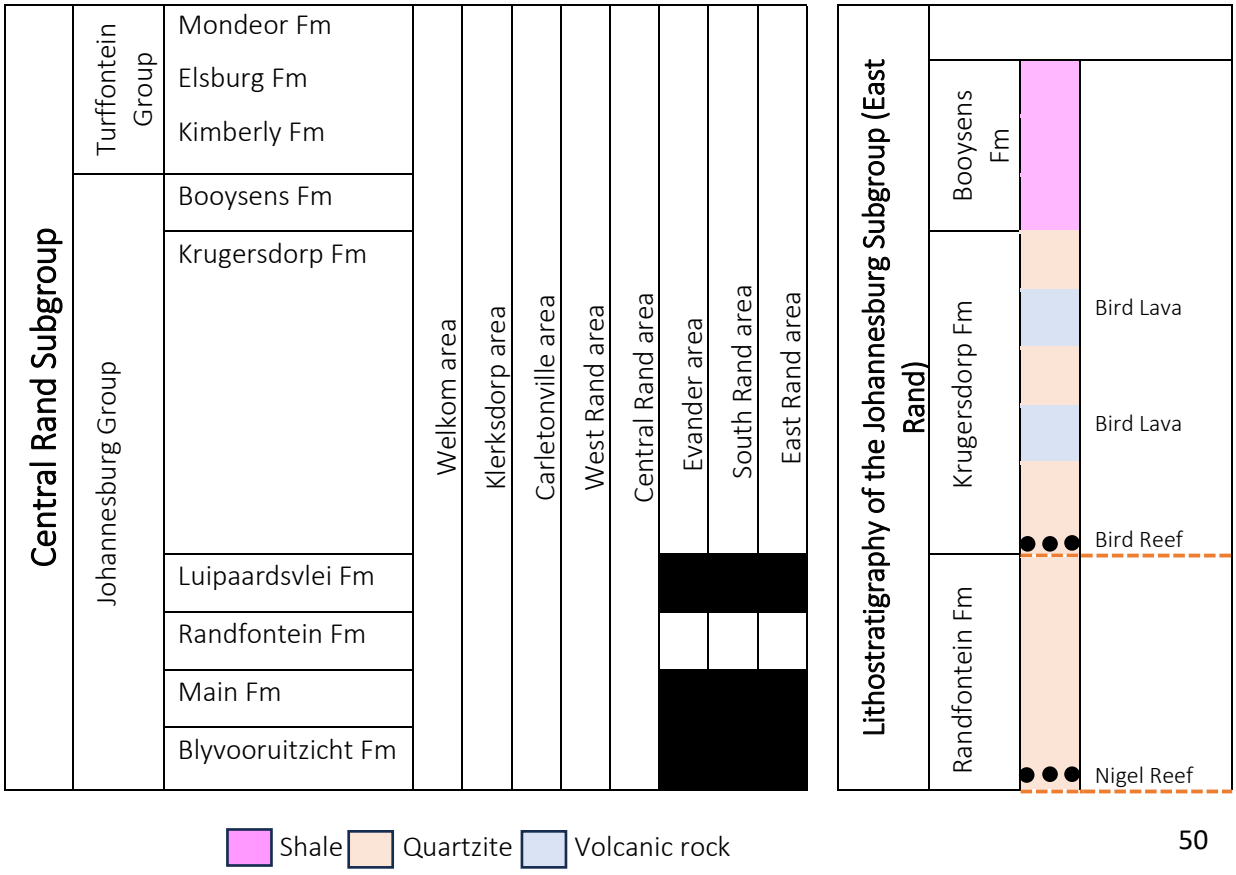

The East Rand is a shallow sub-basin area located in the eastern section of the Central Rand Subgroup (McCarthy, 2006). It is characterised by gentle folds, striking north-westerly, and a disconformity truncating the lower Blyvooruitzicht Formation and Main Formation as well as the middle Luipaardsvlei Formation (McCarthy, 2006; Frimmel, 2019). The remnant of the lower Johannesburg Group for the area is, therefore, the Randfontein Formation, followed by the Krugersdorp Formation (which is also characterised by volcanic units of the Bird Lava) and overlain by shales of the Booysens Formation (Table 4.1) (McCarthy, 2006; Frimmel, 2019). The aggregates used in this study are sampled from this area.

4.2. Area of interest

The Sub-Nigel Quarry, with coordinates: 26˚22'0.00" S 28˚27'0.00" E (Figure 4.2A), is an opencast mine known for its services as a supplier of concrete aggregate and crusher sand (Figure 4.2B-(i)) (AfriSam, 2021). The AfriSam owned quarry is in Sub-Nigel, an area located approximately 4 km away from Nigel. Nigel is a small town situated in the Gauteng province of South Africa (Figure 4.2A) and is known for gold mining dating back to the 1800s (Kleinhans, 2016). This town is classified under the East Rand as it is positioned southeast of Johannesburg and south of Springs (Figure 4.2A) (Kleinhans, 2016). Geologically, Nigel is part of the Witwatersrand Supergroup (McCarthy, 2006; Kleinhans, 2016).

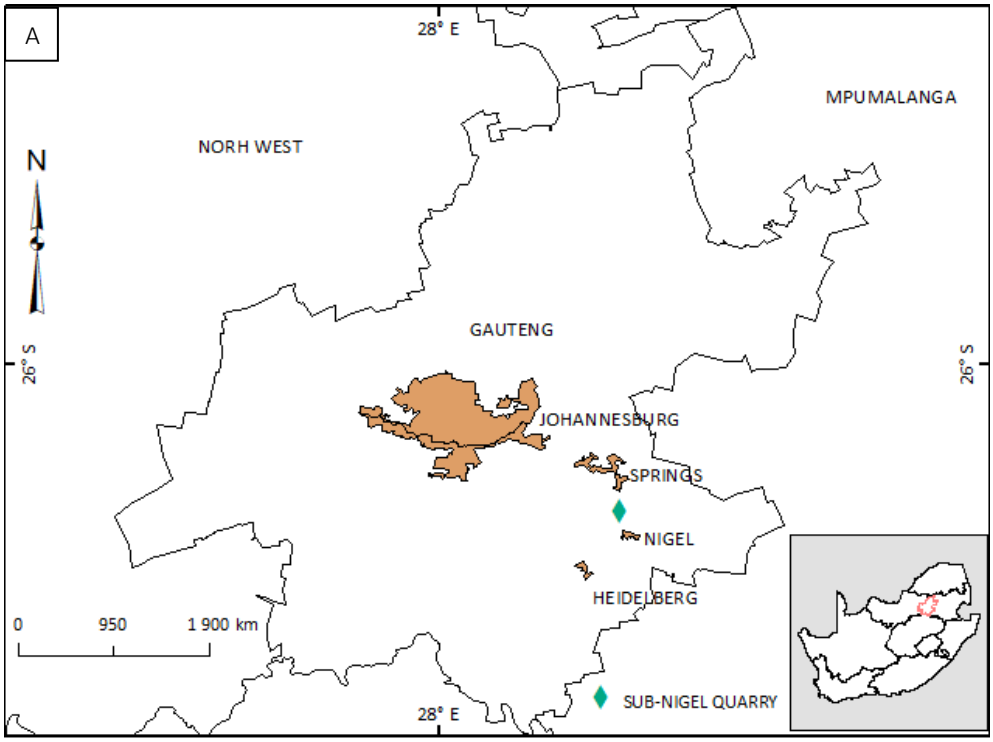

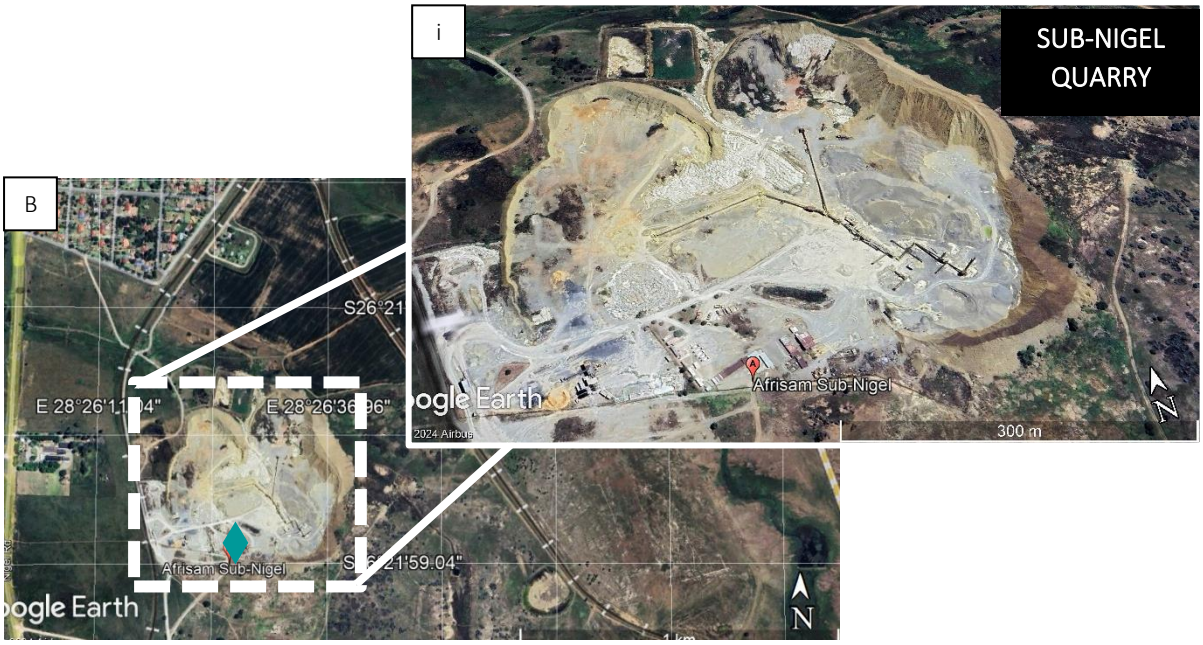

Figure 4.2*: Images showing the area of interest. A) Map showing the location of the study area, the Sub-Nigel Quarry, and the surrounding cities and towns within Gauteng Province. B) A Google Earth image of the bird's eye view of the Sub-Nigel Quarry. i) An image of the open pit mining quarry.*

4.3. Results

4.3.1. Shale sample

4.3.1.1. Macroscopic (hand specimen) observations

In hand specimen (Figure 4.3A), the shale appears greenish grey to greyish black. It consists of extremely fine-grained minerals, each less than 0.063 mm in size, which are too small to be seen with the naked eye. The rock is characterized by slaty cleavage, with domain spacing of less than 1 mm. Additionally, the weathered surface of the rock exhibits a reddish-brown rust (Figure 4.3A(i)).

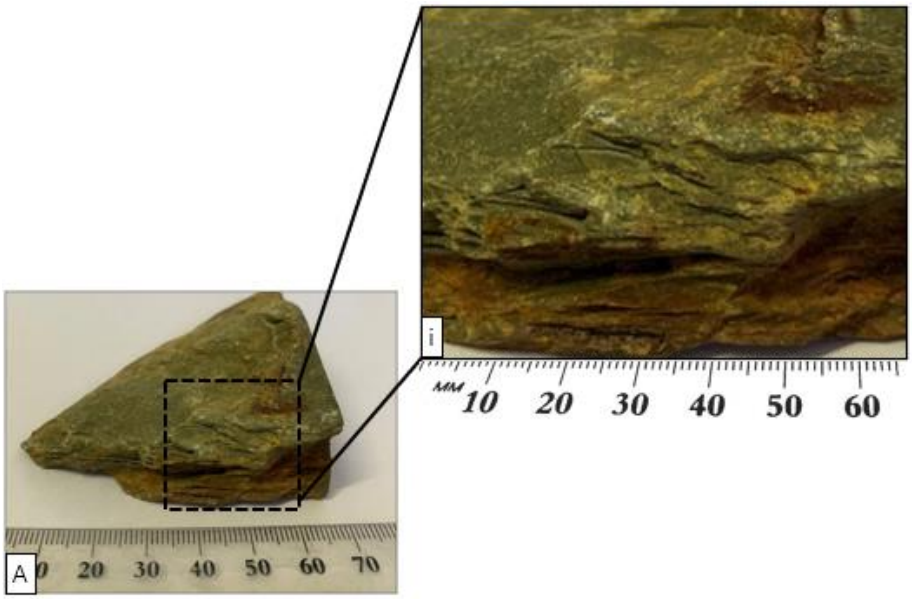

Figure 4.3: *Hand specimen image of shale. A) The rock is greenish grey to greyish black rock with extremely fine-grained (less than 0.063 mm) minerals. i) Slight slaty cleavage with a domain spacing of less than 1 mm and a reddish-brown rust is observed in specific areas.*

4.3.1.2. Petrographic analysis

In this section, the shale is examined under the microscope, revealing its composition and texture. The rock consists of extremely fine-grained muscovite and quartz crystals, each less than 0.05 mm in size. The minerals are aligned in a disjunctive spaced cleavage texture, as illustrated in Figure 4.4A. The Plain Polarised Light (PPL) and Cross Polarised Light (XPL) microscopic images (Figure 4.4B-C) show that quartz occurs as microscopic particles (too small to see undulatory extinction), which are arranged in semi-lenticular layers between the muscovite crystals. Further analysis indicates that the rock is composed of approximately 65% mica, 33% quartz, 2% feldspar, and 1% opaque minerals (Figure 4.4D). This detailed petrographic study highlights the fine-grained nature and distinct mineral alignment of the rock.

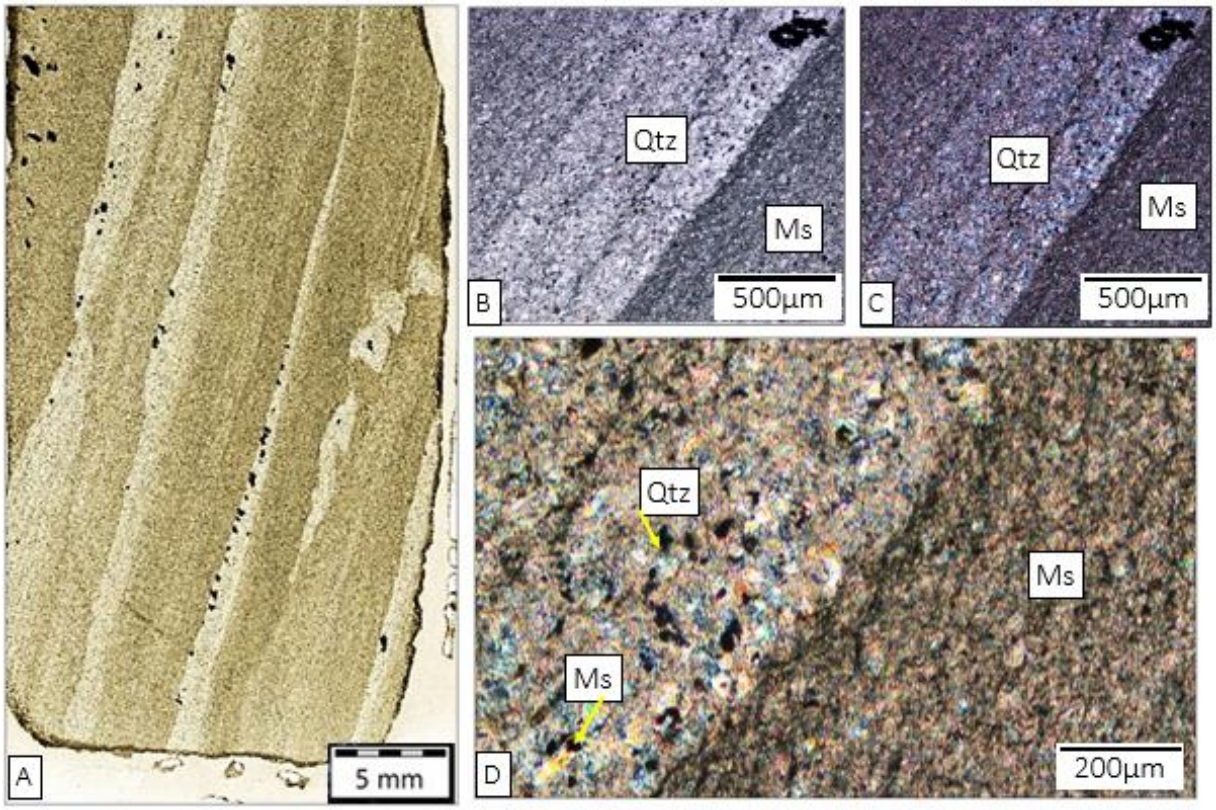

Figure 4.4: Petrographic images of shale. A) A petrographic image in Plain Polarised Light (PPL) showing extremely fine-grained (less than 0.05 mm) muscovite and quartz. B) A microscopic image in PPL (of 4x magnification), showing textures of light layers of quartz and darker muscovite layers. C) A microscopic image in XPL (of 4x magnification), confirms the quartz rich layer and muscovite-rich layers that define the rock. D) A microscopic image in XPL (of 10x magnification), shows that quartz-rich layers also contain muscovite (Qtz= quartz and Ms= muscovite).

4.3.1.3. TIMA analysis: phase maps and elemental maps

Phase maps (Figure 4.5A-B) reveal that the rock is primarily composed of muscovite and lesser amounts of quartz. Muscovite is homogeneously distributed, whereas quartz is found in layered clusters. Pyrrhotite shows a disseminated distribution.

Elemental maps (Figure 4.5C-E) show the layers enriched in quartz and muscovite as depicted by high concentrations of silicon (Si), potassium (K), and aluminium (Al) (Figure 4.5E).

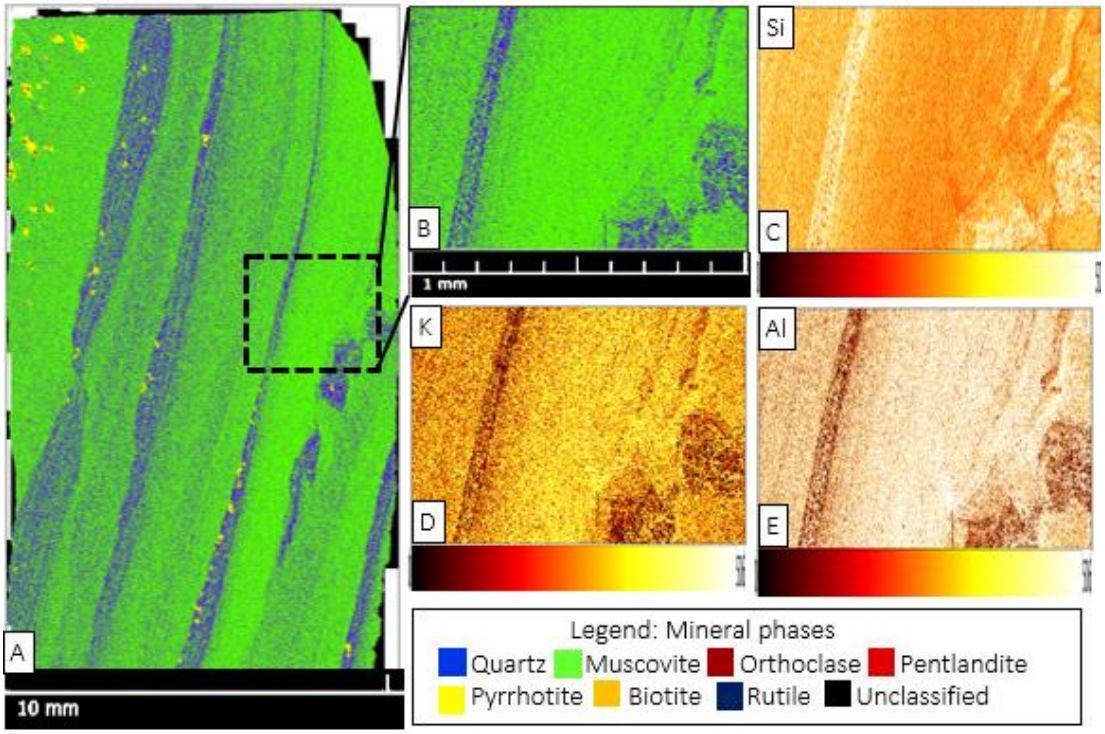

Figure 4.5*: TIMA images of shale. A) Phase maps showing the dominance of muscovite and bands of quartz. B) Magnified phase maps showing bands of quartz are also associated with muscovite. C) Si elemental map, revealing that Si occurs in moderate concentrations (orange) associated with muscovite, higher concentrations are found to be associated with quartz. D) K elemental map, showing the K occurs in high concentrations (yellow) associated with muscovite. E) Al elemental map, showing that Al occurs in extremely high concentrations (white), associated with muscovite.*

4.3.1.4. Modal abundance

Modal abundances were obtained using TIMA and XRD analyses (Figure 4.6). Both analyses reveal that the rock is muscovite rich. However, XRD results (Figure 4.6A, Appendix 3 and 4) show an equal proportion of muscovite and quartz in the rock, whereas TIMA found muscovite to be the most dominant mineral and quartz to be less abundant (Figure 4.6B). Additionally, TIMA identified accessory amounts of biotite, rutile, pyrrhotite, and pentlandite, which could not be identified by XRD.

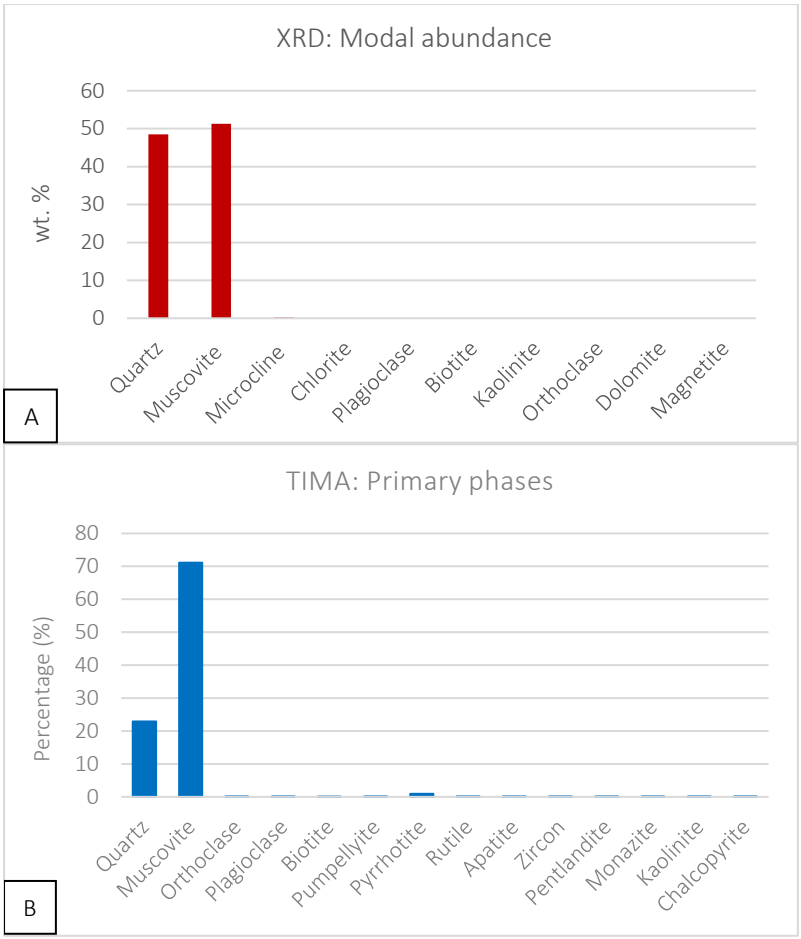

Figure 4.6: *Graphs showing the mineral abundance of shale. A) XRD results (in wt. %) show that muscovite and quartz make up the bulk composition of the rock. B) TIMA results (in %) show that muscovite is the dominant primary phase, followed by quartz, accessory biotite, and pyrrhotite.*

4.3.2. Quartzite sample

4.3.2.1. Macroscopic (hand specimen) observations

The quartzite sample appears bluish grey to greenish-grey and is non-foliated with glassy quartz grains (Figure 4.7A). and the annealing of quartz grains is evident (Figure 4.7(i)). The rock is composed of approximately 90% quartz, with disseminated sulphide grains randomly distributed throughout the sample.

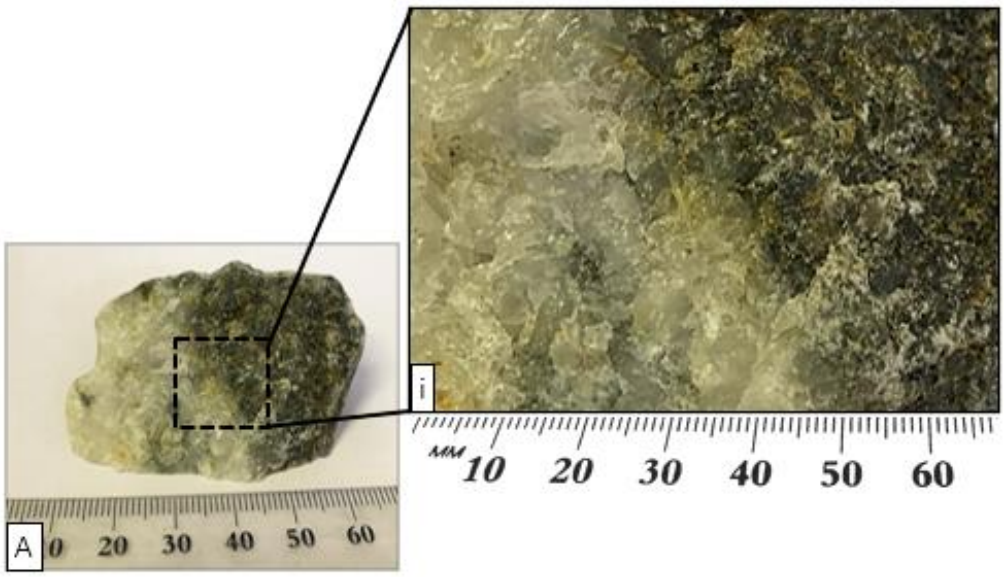

Figure 4.7: Hand specimen image of quartzite. A) A bluish grey to greenish grey, non-foliated rock with glassy quartz grains. i) A magnified image showing the annealing of quartz.

4.3.2.2. Petrographic analysis

Petrographic examination (Figure 4.8A-D) reveals that the quartzite is fine- to coarse-grained and predominantly composed of medium-grained (more than 0.5 mm) quartz crystals, which constitute about 95% of the sample. The quartz crystals are subhedral and lack mineral alignment. The magnified XPL images (Figure 4.8B-D) show the presence of minor amounts of sericite, muscovite, and plagioclase in the interstitial spaces. The rock exhibits granoblastic textures and sutured grain boundaries (Figure 4.8C). Quartz appears as sub-rounded monocrystalline and polycrystalline grains, exhibiting intense undulatory extinction, subgraining, and recrystallization along its boundaries (Figure 4.8D). Additionally, microcrystalline and cryptocrystalline quartz (less than 0.05 mm crystals) is seen within interstitial spaces. Muscovite is present as elongated, finely grained crystals, with some grains showing slightly curved contacts against medium-grained quartz. Intragranular and intergranular microcracking is observed within larger quartz grains.

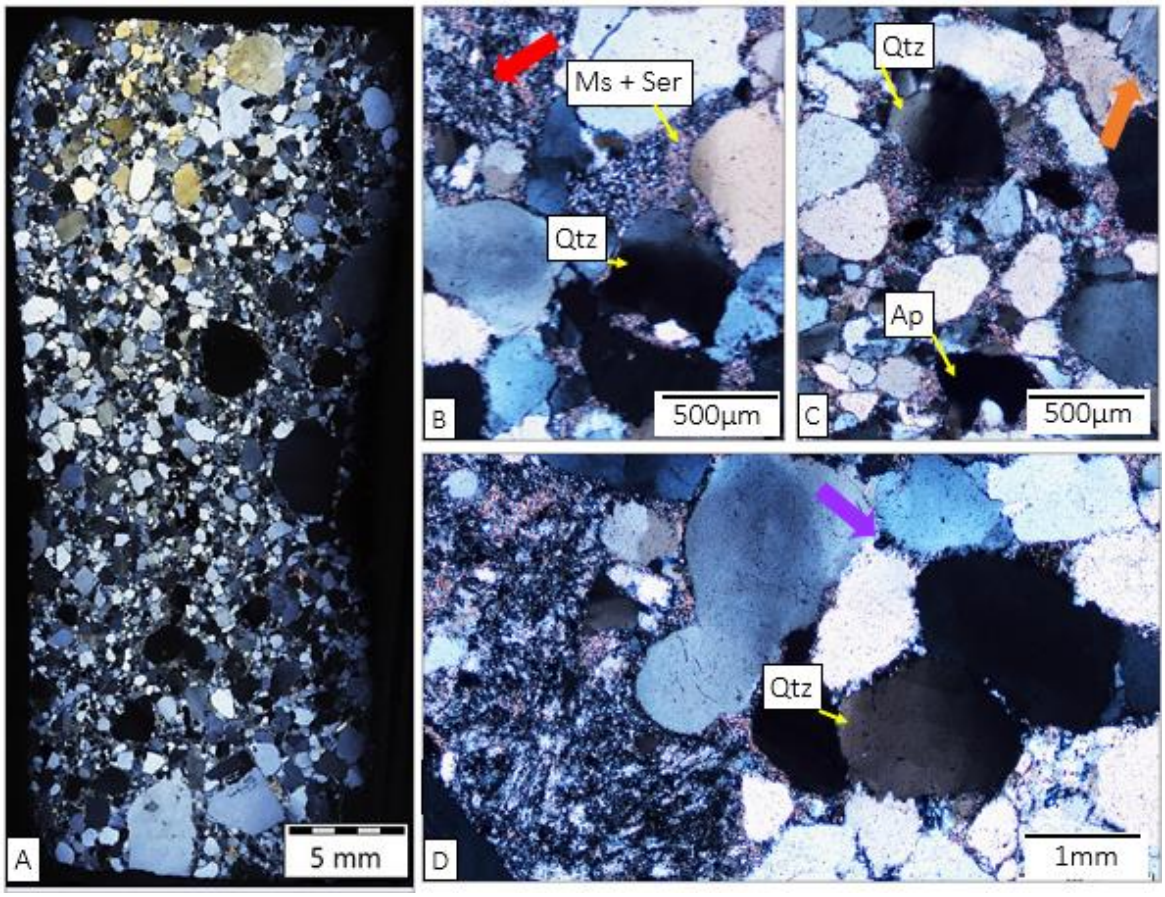

Figure 4.8: *Petrographic images of quartzite. A) XPL image showing the abundance of medium-grained (more than 0.5 mm) quartz and mineral alignment. B) Microscopic image in XPL with magnification 4x; showing intense undulose extinction of quartz crystal, and microcrystalline quartz (red arrow). Interstitial spaces filled with fine-grained sericite (Ser), muscovite (Ms), plagioclase, and pyrite. C) Microscopic image in XPL with magnification 4x showing medium-grained quartz with serrated boundaries (orange arrow) and undulose extinction of quartz. D) Microscopic image in XPL with magnification 4x showing microcrystalline quartz and recrystallisation along quartz boundary (purple arrow).*

4.3.2.3. TIMA analysis: phase maps and elemental maps

TIMA phase maps (Figure 4.9A) reveal that the sample is composed predominantly of quartz, with minor concentrations of muscovite, pyrrhotite, biotite, chlorite, and pyrite in the interstitial spaces. The spatial relationship shows that quartz is homogeneously distributed, while muscovite is more dispersed. The magnified phase maps (Figure 4.9B) further indicate that smaller quartz grains are around larger quartz particles.

Elemental maps (Figure 4.9C-E) show that Si occurs in high concentrations, with the highest concentrations associated with quartz. K and Al occur in low concentrations associated with muscovite. The domains of high Al concentrations show muscovite domains (Figure 4.9E).

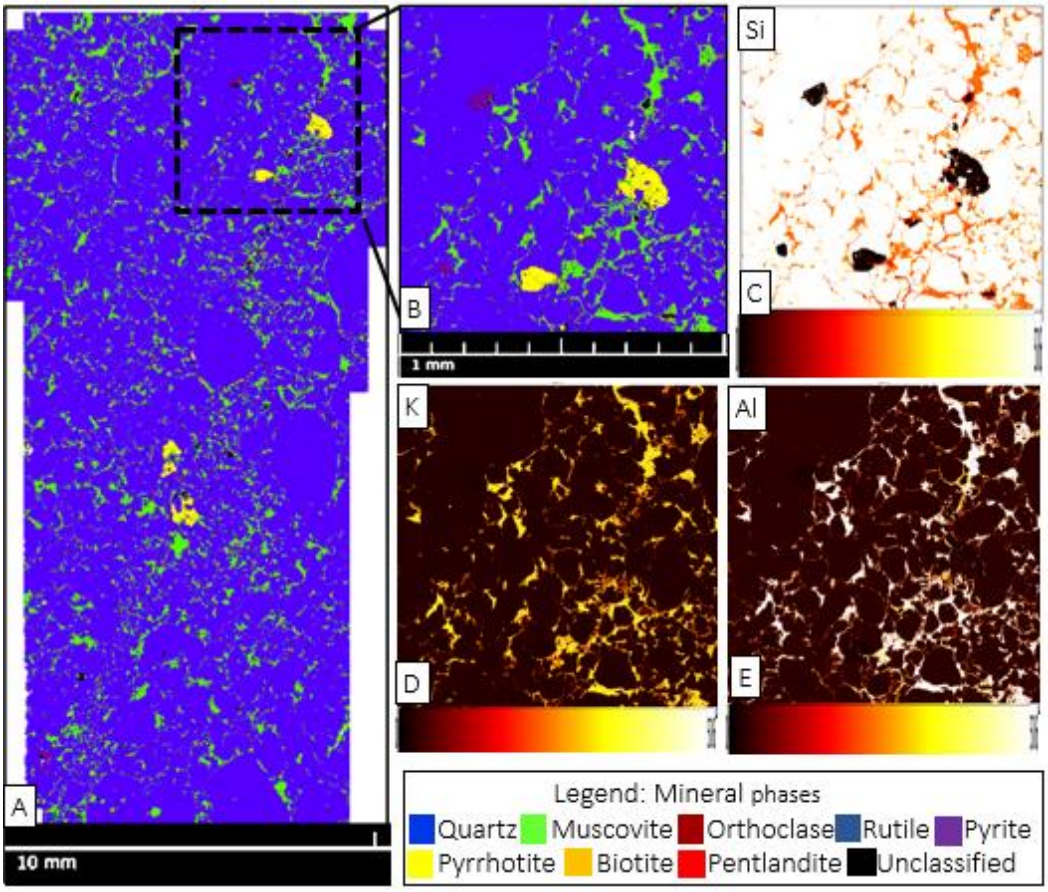

Figure 4.9: TIMA image for quartzite. A) Phase maps showing an abundance of quartz disseminated muscovite and dispersed pyrrhotite textures. B) Magnified phase maps of the rock are defined by quartz grains more than 1 mm, pyrrhotite, and pyrite grains contained in the quartz grains. C) Si elemental map showing variations in Si concentrations, with the highest concentrations associated with the quartz, lowest the pyrrhotite, and pyrite. D) K elemental map, showing that K occurs in low concentrations. E) Al elemental map, showing that high Al concentrations (white), are associated with muscovite.

4.3.2.4. Modal abundance

Modal abundances for the quartzite sample were obtained using TIMA and XRD analyses (Figure 4.10A-B, Appendix 3 and 4). Both analyses reveal that the rock is quartz-dominant with minor muscovite. TIMA also detected accessory amounts of chlorite, pyrite, and pyrope (Figure 4.10B).

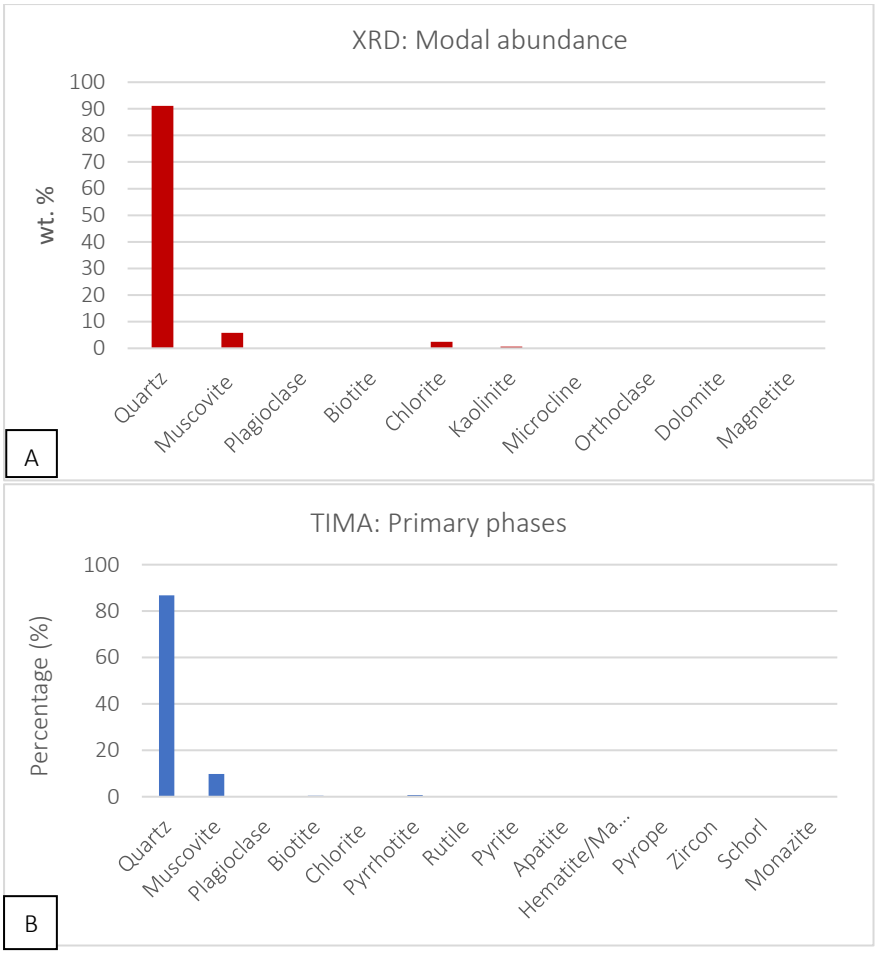

***Figure 4.10**: Graph showing the mineral abundance of quartzite. A) XRD results (in wt. %) show that quartz makes the bulk composition with less amounts of muscovite. B) TIMA results (in %) show that quartz is the dominant primary phase, followed by muscovite. The rock also contains accessory amounts of pyrrhotite, biotite, chlorite, pyrite, and pyrope.*

4.3.3. Accelerated Mortar Bar Test (SANS 6245)

Three specimens (composed of the Witwatersrand quartzite and Booysens shale aggregates) were immersed in NaOH solution for fourteen days and monitored. Test results for the specimens were averaged as follows: after day one of immersion, the average expansion was 0.02%. After seven days of immersion, the average expansion increased to 0.09%, and on day fourteen, the average expansion of 0.17% (Table 4.2). The graph in Figure 4.11 illustrates a general increasing trend of expansion over the fourteen days.

***Table 4.2**: Mean expansion percentages with days for the quartzite and shale aggregate (SN)*

Time	*Expansion %*
D1	0.02
D7	0.09
D14	0.17

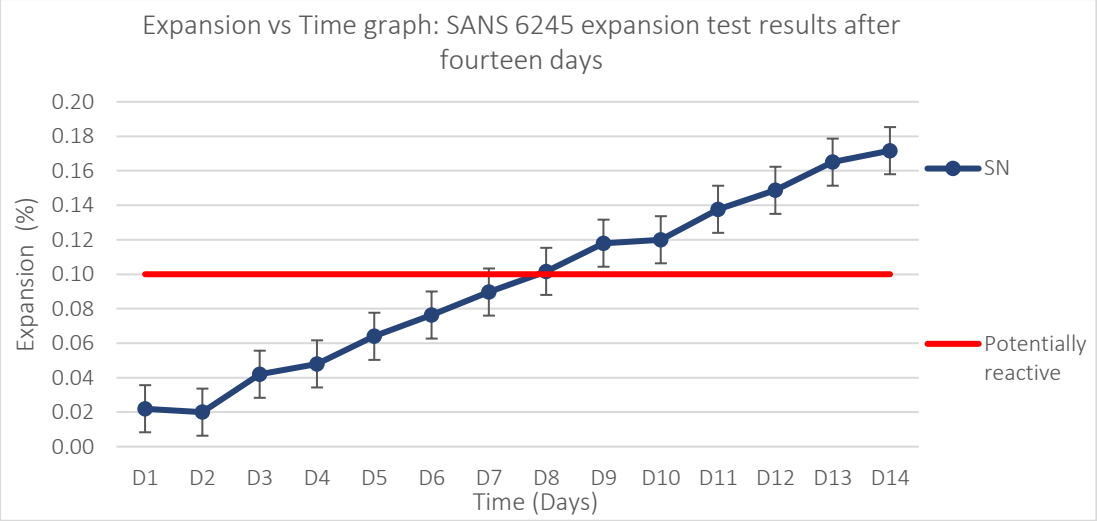

Figure 4.11: *Image showing a graph for the expansion test results using quartzite and shale aggregate for SANS 6245 after fourteen days of immersion in NaOH solution.*

4.4. Discussions

4.4.1. Geological characteristics and classification of the Witwatersrand shale

The Witwatersrand shale used in this study is an extremely fine-grained greenish-grey rock with slightly slaty cleavage. It is predominantly composed of muscovite, classifying it as a micaceous shale. The rock is textured with an alignment of quartz exhibiting a disjunctive cleavage and contains accessory amounts of pyrrhotite, pentlandite, and rutile (Figure 4.5 and Appendix 4). These attributes suggest that the rock experienced low-grade metamorphism, with slightly higher pressure conditions than temperature (Powell, 1979; Twiss and Moores, 1992; Best, 2003; Frost and Frost, 2019). Therefore, the rock can be further classified as a micaceous metashale. Given that the micaceous metashale is abundantly composed of muscovite and less quartz, the rock is richer in aluminium than silica.

4.4.2. Geological characteristics and classification of the Witwatersrand quartzite

The Randfontein Formation quartzite is an impure quartzite characterised by medium quartz grains and a mica-rich matrix filling the interstitial spaces. It also consists of recrystallised quartz edges, intense undulose extinction and an abundance of microcrystalline quartz. Although high-temperature conditions are the primary cause for the formation of the rock, the serrated boundaries and the slightly curved muscovite contacts (muscovite has an elastic tenacity), as well as the brittle tenacity of quartz evident through intragranular and intergranular microcracking, suggest that the rock was subjected to additional strain (Twiss and Moores, 1992; Best, 2003; MacKenzie *et al.*, 2017; Frost and Frost, 2019). This indicates a maximal displacement of quartz crystalline structure (Blight and Alexander, 2011; Fernandes *et al.*, 2016; Leeman *et al.,* 2016; Tiecher *et al*, 2018). Due to the abundance of quartz, the rock contains high silica concentrations (Figure 4.9 and Appendix 2)

4.4.3. Expansion results for the Witwatersrand quartzite and micaceous metashale

The Accelerated Mortar Bar Test, SANS 6245, was conducted over a fourteen-day period, during which three specimens containing, a composite sample of, both the quartzite and metashale aggregates were immersed in a NaOH solution, and strain changes were recorded daily (Appendix 5). Minor changes were observed on the first two days; however, on the third day, strain increased significantly, nearly doubling. As the days of immersion increased, so did expansion, following an almost linear trend (Figure 4.11). Although average results were presented (in Table 4.3 and Figure 4.11), all specimens behaved similarly, and by day eight, they had experienced a 0.1% expansion (Appendix 5). According to Oberholster and Davis (1986) (Table 2.8), specimens with expansions of more than 0.1% are potentially deleterious. The expansion experienced by these specimens at the end of the experiment (day fourteen) was 0.17%. Therefore, the Randfontein Formation quartzite aggregate and Booysens Formation micaceous metashale aggregate (in the East Rand area) of the Witwatersrand are potentially alkali reactive.

4.5. Closure

This chapter looked at the Witwatersrand quartzite and metashale aggregates sampled from the Sub-Nigel Quarry. The micaceous metashale is characterised by cryptocrystalline and microcrystalline quartz exhibiting disjunctive cleavage alignment. Mineral extinction could not be observed due to its extremely fine-grained texture, however with the employment of XRD and TIMA, muscovite was identified to be the dominant mineral.

The quartzite is a quartz-rich, medium-grained rock, interstitially filled by a mica-rich matrix. It is characterised by monocrystalline and microcrystalline quartz with intense undulose extinction, as well as subgraining and recrystallisation along quartz boundary. The medium- to coarse-grained quartz also have intergranular and intragranular microcracking. A composite sample (consisting of the quartzite and micaceous metashale) was used for the AMBT (SANS 6245) and exhibited expansive behaviour (with an expansion of 0.17%). The expansion results thus, classify, the Witwatersrand quartzite (Randfontein Formation) and micaceous metashale, as potentially alkali-reactive aggregates.

CHAPTER FIVE

5. The Dwyka tillite

5.1. Geological setting

During the late Carboniferous, glacial sediments were deposited to form the basal Karoo Supergroup in South Africa (Von Brunn, 1996; Bussio, 2012). The Karoo is distinguished by volcanic deposits as well as diverse sedimentary sequences spanning from late Carboniferous to early Jurassic and covers 550 000 km^2 (Rubidge and Hancox, 2002; Bussio, 2012). The Karoo is made up of the lower Dwyka Group, Ecca Group, Beaufort Group, and upper Stomberg Group (Table 5.1) (Rubidge and Hancox, 2002). The upper Stomberg Group comprises of three formations attributed to the changes from arid to semi-arid conditions (Johnson *et al*., 1996; Selden and Nudds, 2012). The occurrence of arid conditions and Permo-Triassic extinction during the late Triassic resulted in the lower Molten Formation (Johnson *et al*.,2006; Selden and Nudds, 2012). Semi-arid conditions resulted in the Elliot Formation's red marls, whereas Jurassic dune sandstones formed the Clarens Formation (Selden and Nudds, 2012). The sudden transition from humid to arid environments resulted in the formation of the underlying Beaufort Group sediments (Selden and Nudds, 2012). These sediments indicate a period of expansive flood plains in drier and warmer climatic conditions with sedimentary contribution coming from every direction (Selden and Nudds, 2012). Following is the Ecca Group, which is strongly associated with the Ice Age and its sediments representing shallow, landlocked marine environments (Selden and Nudds, 2012). The coal-rich Ecca Group conformably overlies the Dwyka Group (Johnson *et al*.,2006; Selden and Nudds, 2012).

The deposition of the 400 m thick Dwyka occurred during the Gondwana glaciation as a result of the transition from the ice age to shallow marine (Johnson *et al*.,2006; Dietrich and Hofmann, 2019). The lower Dwkya Group consists of the oldest Karoo rocks and is characterised by various glacial sediments consisting of diamictites, conglomerates, fluvioglacial pebbly sandstones, rhythmite, and mud rock (Thomas *et al*., 1990; Modie and Le Hérissé, 2009). The Permo-Carboniferous Dwyka Group exhibits considerable lithological differences across the basin, leading to the identification of a southern and northern facies (Johnson *et al*., 2006; Dietrich and Hofmann, 2019). The northern facies are mostly composed of the Mbizane Formation and is distinguished by vast thickness variations, a lack of massive diamictite, and a high mudrock component (Johnson *et al*., 2006). The southern facies, hosting the Elandsvlei Formation, is characterized by a gradual increase in thickness, consistent lithology, and a high massive diamictite and low mudrock component (Johnson *et al*., 2006; Modie and Le Hérissé, 2009).

***Table 5.1**: A table showing a simplified lithostratigraphy of the Karoo Supergroup and sediments associated to each Formation (Fm). The basal Dwyka is characterised by glacial sediments, where the Umlaas tillite aggregate is sourced (adapted and modified from Johnson et al., 2006; Modie and Le Hérissé, 2009).*

Karoo Supergroup	Stomberg Group	Clarens Fm	Sandstone, red beds, silt-mudstone and conglomerates Silt-mudstone-lime
		Elliot Fm	
		Molteno Fm	
	Beaufort Group		
	Ecca Group	Volkrust Fm	Marine to deglaciation climates sediments (mudstone)
		Vryheid Fm	
		Pietermaritzburg Fm	
	Dwyka Group		Glacial sediments (tillites, siltstones, sandstones, mudstone)

5.2. Area of interest

The Umlaas Quarry, also known as the Umlaas Road Quarry, coordinates 29˚42'26.66"S 30˚30'09.84"E (Figure 5.1A) (AfriSam, 2021) is a concrete aggregate supplier, neighbouring the National Road N3 (Figure 5.1B). This open pit mining quarry (Figure 5.1B(i)) is located approximately 20 km southeast of Pietermaritzburg, in the KwaZulu Natal province of South Africa (Britannica, 2023). Although the province is characterised by lithological variations, Pietermaritzburg falls under the Karoo Supergroup, with the Umlaas Quarry mining tillite from the Dwyka Group (AfriSam, 2021).

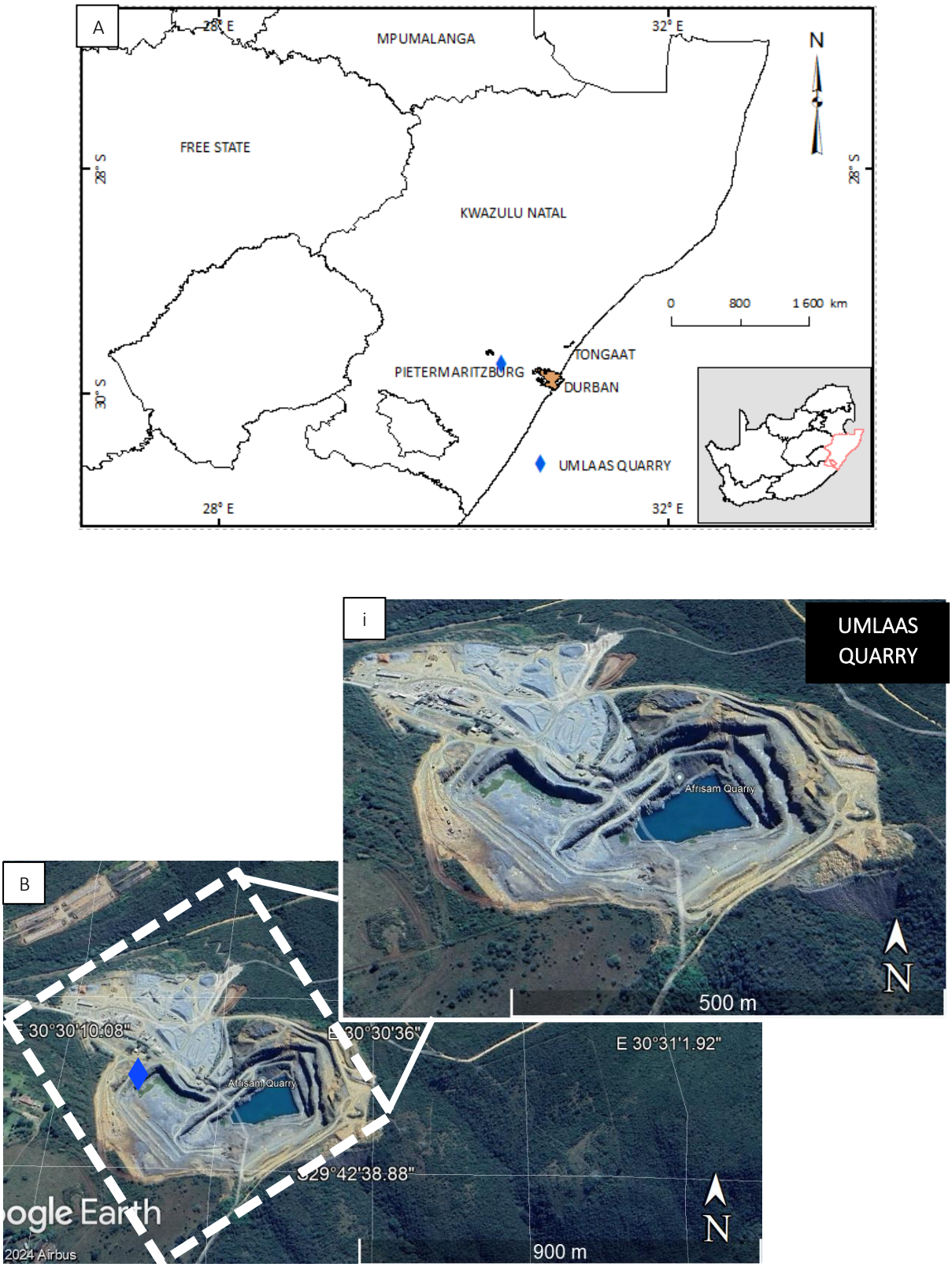

Figure 5.1: *Image showing the area of interest. A) Map showing the location of the study area, the Umlaas Quarry, and surrounding cities, in the KwaZulu Natal province. B) A Google Earth image showing the bird's eye view of the Umlaas Quarry. i) A magnified image of the open pit mining quarry.*

5.3. Results

5.3.1. Macroscopic (hand specimen) observations

Tillite is a greenish grey to bluish-grey rock with inclusions of white, brown, and minor red lithic fragments (Figure 5.2A). The lithic fragment grains range from 0.4-1.4 mm and are semi-angular to angular (Figure 5.2A (i)). The fragments are poorly sorted and lack any distinct correlation to one another, apart from being cemented by glacial tuff. The minerals observed within the tillite include quartz, mica, plagioclase, and chlorite.

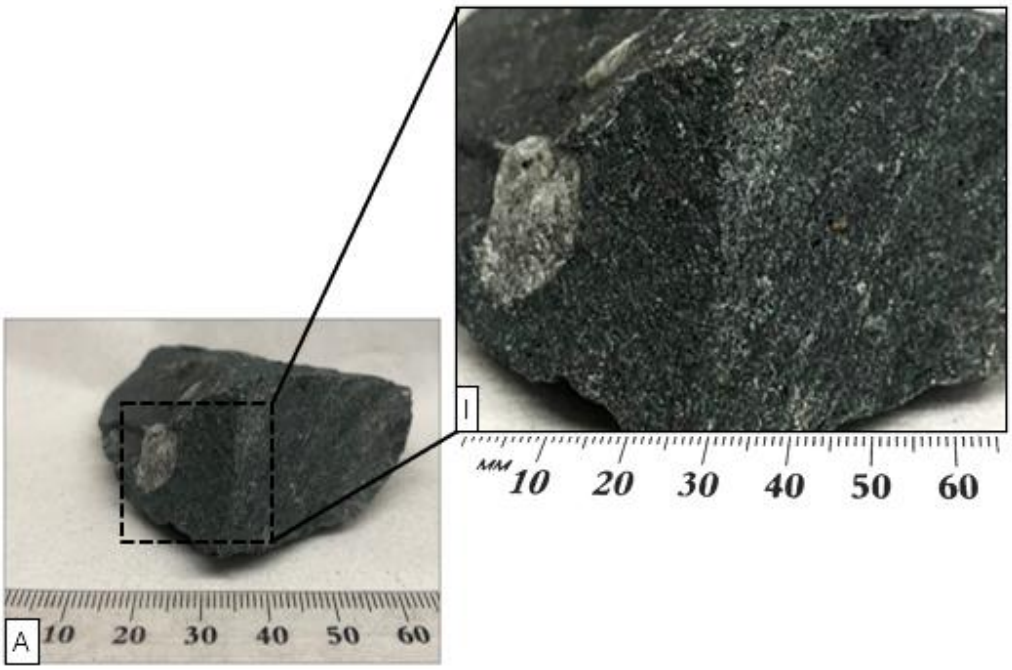

Figure 5.2: Hand specimen image of tillite. A) A greenish grey to bluish-grey rock with inclusions of white, brown, and minor red lithic fragments. i) The grain size of lithic fragments varies from 0.4-1.4 mm. The minerals observed include quartz, mica, and chlorite.

5.3.2. Petrographic analysis

Petrographic analysis (Figure 5.3A-E) shows that tillite is a fine-grained rock characterised by medium- to coarse-grained (0.2-6 mm) fragments varying in composition cemented by an extremely fine-grained matrix. The magnified microscopic images (Figure 5.3B-E and Appendix 8) reveal that tillite is composed of a clay-rich matrix cementing lithic fragments with diverse textures. The sample is characterised by zones of poikilitic and poikiloblastic textures along with lepidoblastic layers of muscovite in certain fragments; however, the overall sample shows no mineral alignment. The rock consists of kaolinite, plagioclase, quartz, albite, biotite, muscovite, actinolite, hornblende, chlorite, microcline, and cordierite. Quartz occurs as anhedral polycrystalline clasts and as microcrystalline grains exhibiting undulose extinction. Microcrystalline quartz is also observed as veins within the poikiloblastic lithic fragments. Plagioclase appears as euhedral to subhedral crystals showing no signs of alteration. Intragranular and intergranular microcracking in a few crystals is also observed.

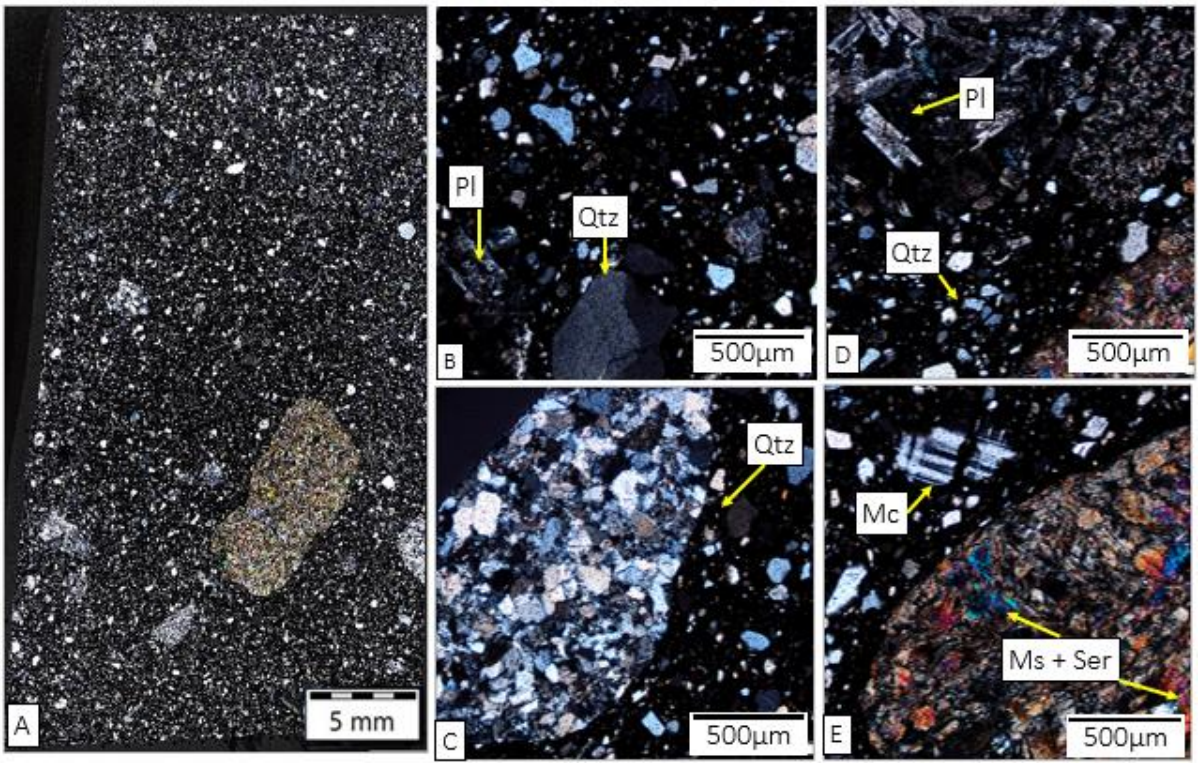

Figure 5.3: *Petrographic images of tillite. A) XPL image showing the fine-grained texture of tillite, an abundance of fine-grained quartz and plagioclase grains and a coarse fragment with a secondary plagioclase vein. B) Microscopic image in XPL with magnification 4x showing euhedral to subhedral plagioclase and undulatory extinction of a quartz grain. C) Microscopic image in XPL with magnification 4x, showing another area of the tillite rock with dominant quartz and orthoclase. D) Microscopic image in XPL with magnification 4x, showing poikilitic and poikiloblastic textures, lithic fragments varying in mineralogy, with euhedral plagioclase, muscovite, and sericite (Pl= plagioclase, Qtz= quartz, Ser= sericite, and Ms= muscovite). E) Microscopic image in XPL with magnification 4x, showing the presence of microcline and microscopic muscovite and sericite.*

5.3.3. TIMA analysis: phase maps and elemental maps

TIMA phase maps (Figure 5.4A) reveal that the tillite is defined by a variety of grain sizes and composed of plagioclase, quartz, albite, microcline, and orthoclase. The spatial relationship shows that plagioclase is homogeneously distributed throughout the sample, with dispersed albite and orthoclase. Additionally, quartz occurs as fine-grained clusters with a dispersed distribution. The enlarged phase maps (Figure 5.4B) show that tillite consists of medium-grained (more than 1 mm) orthoclase, albite, and actinolite clasts. It also highlights clusters of chlorite clasts, albite, disseminated pumpellyite, and ferro-actinolite crystals within the large actinolite clast, along with disseminated muscovite and secondary albite veins.

Elemental maps (Figure 5.4C-E) reveal that Si and Al occur in higher concentrations than K, associated with plagioclase and muscovite domains.

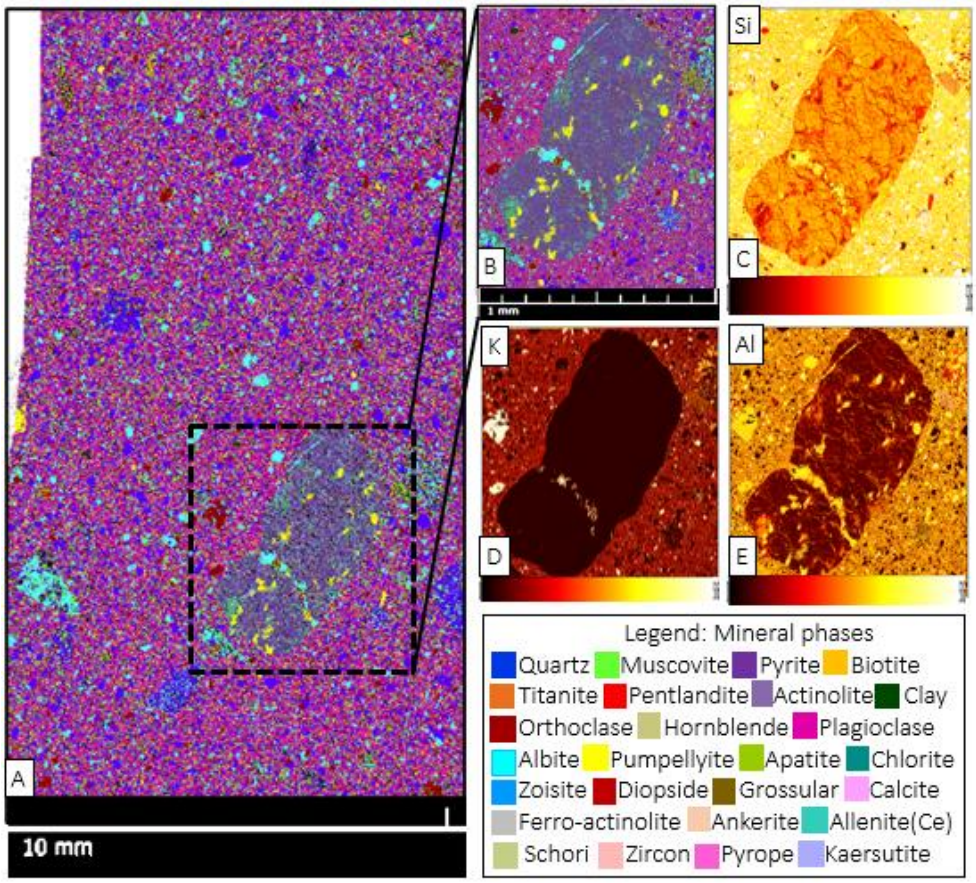

Figure 5.4: *TIMA Images for tillite. A) Phase maps show the dominance of plagioclase, dispersed quartz, albite, and disseminated orthoclase textures. B) Magnified phase maps reveal the coarse-grained (more than 5 mm) actinolite contains fine plagioclase, albite, pumpellyite, orthoclase, and chlorite as well as secondary albitic vein. C) Si elemental map showing high concentrations associated with plagioclase and quartz. D) K elemental map showing low concentrations (in red) with some high concentrations (in white) associated with albite. E) Al elemental map showing high concentrations associated with plagioclase.*

5.3.4. Modal abundance

The modal abundances for the tillite rock were obtained using TIMA and XRD analyses (Figure 5.5, Appendix 3 and 4). XRD results (Figure 5.5A) indicate that the rock contains 50 wt. % quartz and 20 wt. % plagioclase, whereas TIMA results (Figure 5.5B) suggest that the rock is plagioclase dominant, containing 45%, with quartz being of secondary abundance (containing 30%). Additionally, XRD analysis shows that chlorite is more abundant than biotite, while TIMA results indicate the opposite, with biotite being more abundant than chlorite.

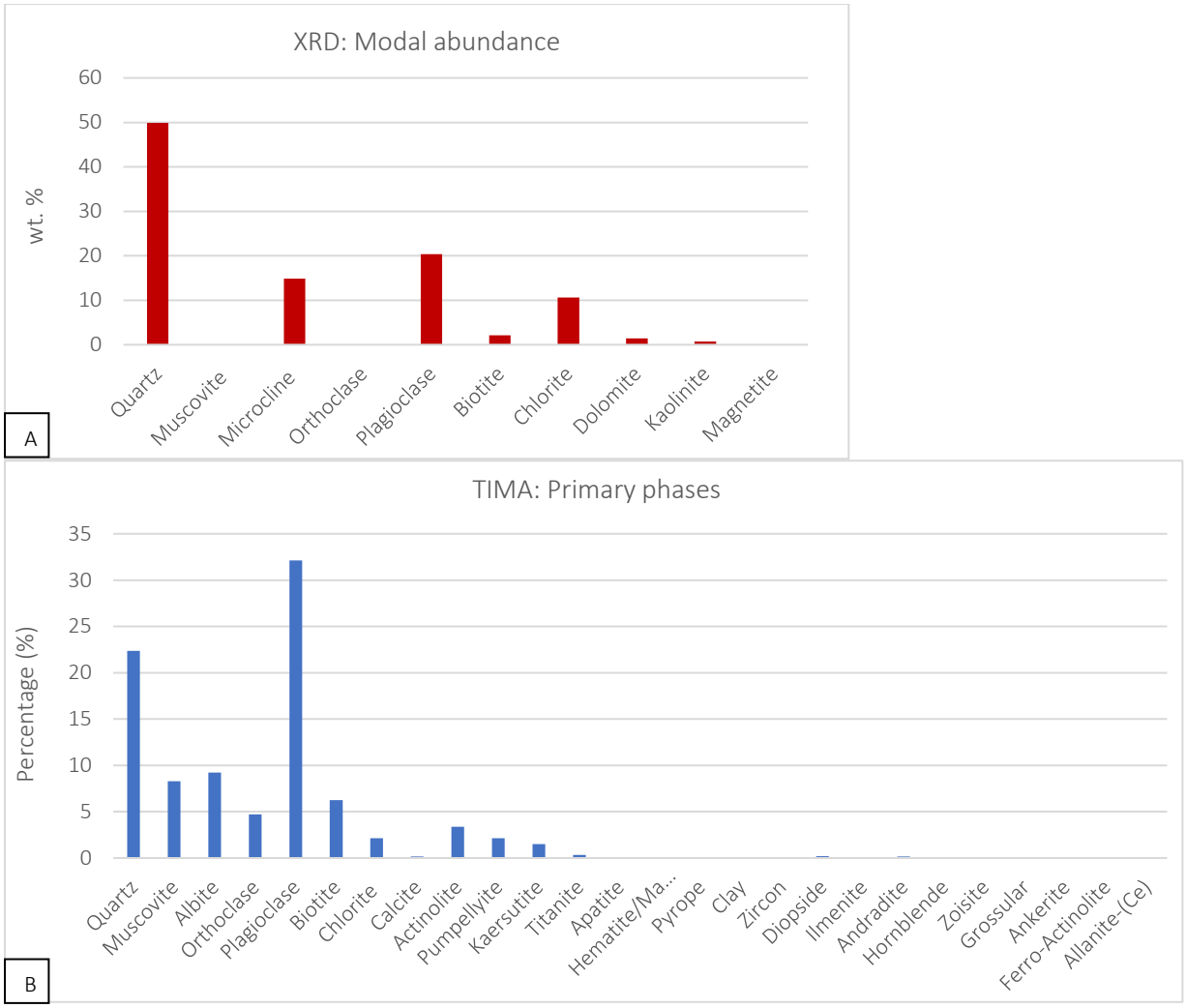

Figure 5.5*: Graphs showing the mineral abundance of the tillite sample. A) XRD results (in wt. %) show that quartz and plagioclase make the bulk composition of the rock, with less microcline and chlorite as well as accessory kaolinite. B) TIMA results (in %) show that plagioclase and quartz are the dominant primary phase, followed by albite, muscovite, and biotite. The rock also contains actinolite, pumpellyite, and kaersutite as well as accessory amounts of diopside, calcite, andradite, zoisite, pyrope, and clay.*

5.3.5. Accelerated Mortar Bar Test (SANS 6245)

SANS 6245 test results for the specimen were averaged and are as follows: after one day of curing, the average expansion was 0.01%. After seven days of curing, the average expansion increased to 0.04%, and by day fourteen of curing, the average expansion reached 0.09% (Table 5.2). The graph in Figure 5.6 illustrates a consistent increasing trend of expansion over the fourteen days.

Table 5.2: Mean expansion percentages with days for the tillite sample (UT)

Time	*Expansion %*
D1	0.01
D7	0.04
D14	0.09

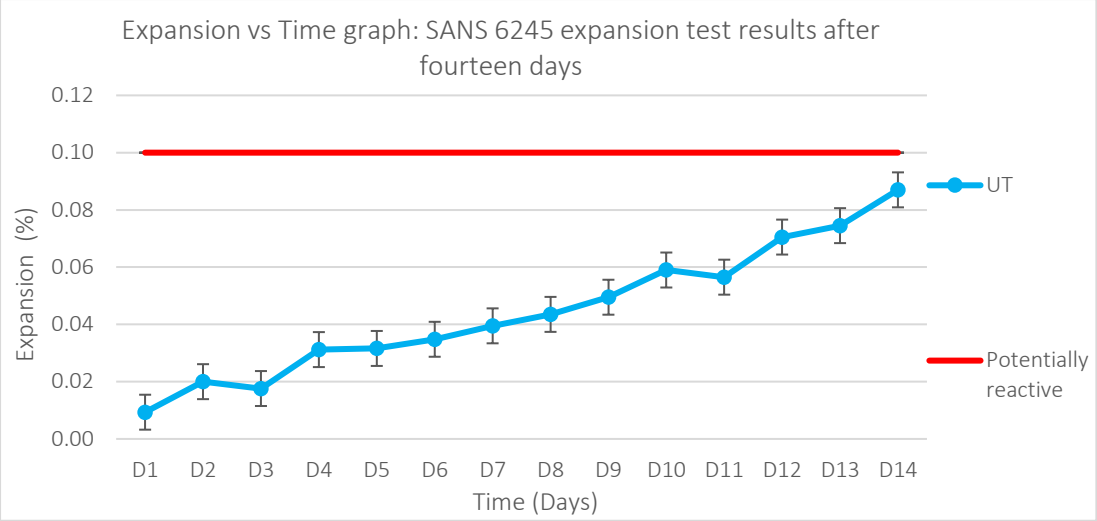

***Figure 5.6**: Image showing a graph for the expansion test results using tillite (UT) aggregate for SANS 6245 after fourteen days of immersion in NaOH solution.*

5.4. Discussions

5.4.1. Geological characteristics and classification for the Dwyka tillite

The Dwyka tillite is a greenish-black rock, primarily composed of a matrix of kaolinite, chlorite, plagioclase, albite, orthoclase, and microcrystalline quartz that cements medium to coarse-grained lithic fragments. This sedimentary rock also exhibits poikilitic and poikiloblastic textures along with lepidoblastic layers. However, these textures are not uniformly distributed throughout the rock, and the coarse-grained clasts show no correlation to each other or the cementing agent (Appendix 8). Additionally, relic deposition sedimentary textures are still preserved. This suggests that metamorphism and deformation affected certain lithic fragments prior to cementation (Nichols, 2009; MacKenzie *et al.*, 2017; Frost and Frost, 2019). Given that the rock is abundant in quartz and feldspar, it is thus, rich in aluminium and silica (Appendix 9).

5.4.2. Expansion results for the Dwyka tillite

The Accelerated Mortar Bar Test, SANS 6245, was carried out for fourteen days using three specimens containing a single composition of the Dwkya tillite. These specimens were immersed in NaOH solution, and strain changes were recorded daily. Minor changes were observed on the first two days, but a noticeable increase was seen on the fourth day. As the number of immersion days increased, so did the expansion (Appendix 5 and 6). Although all specimens showed a general incremental increase in expansion, two specimens reached 0.1% while one specimen remained below 0.1% on day fourteen. According to Oberholster and Davis (1986) (Table 2.8), specimens with less than 0.1% expansion are classified as non-reactive aggregate, whereas those with 0.1-0.2% expansion are classified as potentially deleterious. The variation in expansion experienced indicates that some fell into the non-reactive

category, while others fell into the potentially reactive category. However, due to the mechanism of ASR, the Dwyka tillite aggregate can be identified as a potentially reactive aggregate.

5.5. Closure

This chapter examined the Dwyka tillite sampled from the Umlaas Road Quarry. This sedimentary rock is a finely textured rock with a variety of medium- to coarse-grained lithic fragments. It is characterised by both metamorphic and sedimentary textures, suggesting that metamorphic occurred prior cementation. The rock is quartz- and feldspar -rich, consists of microcrystalline quartz exhibiting strong undulatory extinction as well as intergranular and intragranular microcracking. The tillite used in the AMBT (SANS 6245), showed expansive behaviour (with an expansion of 0.1%). The expansion results classify the Dwyka tillite as a potentially alkali-reactive aggregate.

CHAPTER SIX

6. The Natal Group quartzite

6.1. Geological setting

The Natal Group is a Palaeozoic siliclastic sedimentary sequence overlying the Namaqua-Natal Metamorphic basement rocks (Bell and Lindsay, 1999; Vorster *et al*., 2016). It extends along the southeastern coastal margin in KwaZulu Natal and in the northeastern region of the Eastern Cape Province of South Africa (Vorster *et al*., 2016). The Natal Group is overlain by the Msikaba Formation however the stratigraphic relationship between these two sedimentary successions remains a source of debate (Hicks, 2010). Previously, the Msikaba Formation was considered to belong to the Ordovician Natal Group however several scholars have recently opposed this theory, proposing that the Msikaba is Devonian in age, probably correlating to the Witterberg Group of the Cape Supergroup and not to Natal's red-bed succession (Liu and Cooper, 1998; Hicks, 2010).

The Natal Group is an approximately 600 m thick succession that unconformably overlies Archean Kaapvaal rock and intermittently outcrops from Hlabisa to Hibberdene and extends inland up to Pietermaritzburg (Figure 6.1) (Marshall and von Brunn, 1999; Hicks, 2010). The formation of the Natal Group is quite debatable however it is believed that during a tectonically induced move of a Pan-African orogenic terrane, there was deposition of sediments into a foreland graben which formed it (Marshall and von Brunn, 1999; Vorster *et al*., 2016). This sedimentary succession is composed of reddish-brown arkosic sandstone, siltstone, micaceous mudrock, and reddish-grey conglomerate (Vorster *et al*., 2016). The Natal Group is divided into two tectonically induced formations: the basal Durban Formation, which is further subdivided into six members, and the upper Marianahill Formation, which is subdivided into three members, as summarized in Table 6.1 (Marshall and von Brunn, 1999; Vorster *et al*., 2016). This upper Marianahill is made up of arkosic sandstones and silty-mudstone lenses that were deposited in a fluvial terrestrial environment. (Johnson *et al.,* 2011).

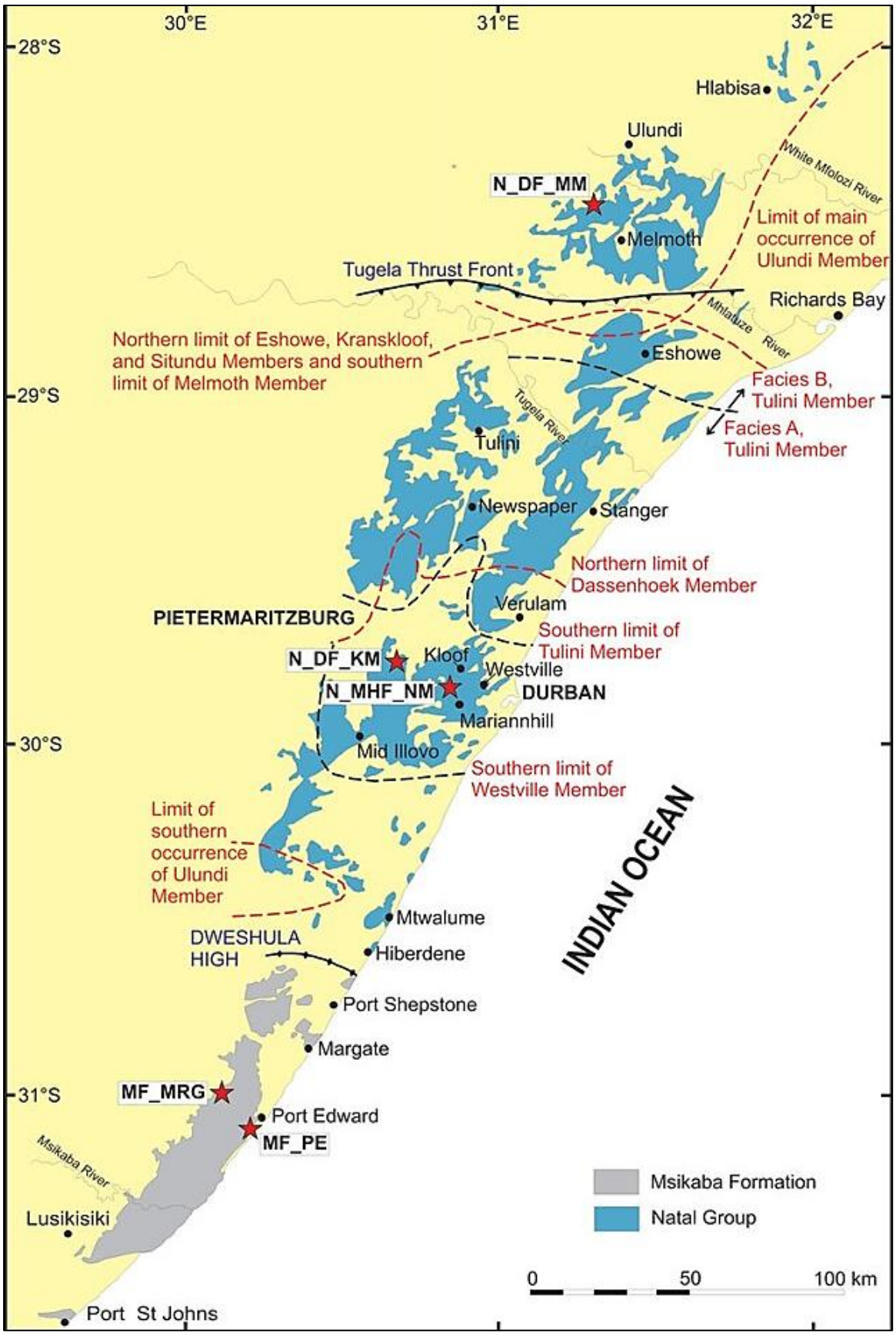

Figure 6.1: Map showing the Natal Group and Msikaba Formation, located along South Africa's eastern margin, and the distribution of the main units (Vorster et al., 2016).

Table 6.1: Summary of the lithostratigraphy of Natal Group (modified Marshall and von Brunn, 1999; Vorster et al., 2016).

Group	Formation	Member	Rock type
Msikaba Formation			
Natal Group	Marianahill	Westville	Matrix-supported conglomerate
		Newspaper	Arkosic sandstone and shale
		Tulini	Small pebble conglomerate
	Durban	Melmoth	Arkosic sandstone and interbedded shale
		Dassenhock	Silicified quartz arenite
		Situndu	Coarse-grained arkosic sandstone
		Kranskloof	Silicified-rich quartz arenite
		Eshowe	Arkosic sandstone and shale
		Ulindi	Coarse monomict, clast-supported conglomerate
Namibia-Natal Metamorphic basement rocks			

6.2. Area of interest

The Coedmore Quarry, with coordinates 29˚ 54’ 04.50” S 30˚ 56’ 56.00” E (Figure 6.2A), is an opencast mine extracting aggregate for concrete production (Jones *et al*., 2011; AfriSam, 2021) (Figure 6.2B (i)). The AfriSam (PTY) Ltd-owned quarry is found adjacent to the N2 and is situated in Bellair (Figure 6.2B) (Jones *et al.*, 2011; AfriSam, 2021). Bellair is a suburb in the southern parts of Durban within the KwaZulu Natal province of South Africa (Figure 6.2B). The Coedmore Quarry holds mining rights to the Natal Group aggregates, used in this study (Jones *et al*., 2011; AfriSam, 2021).

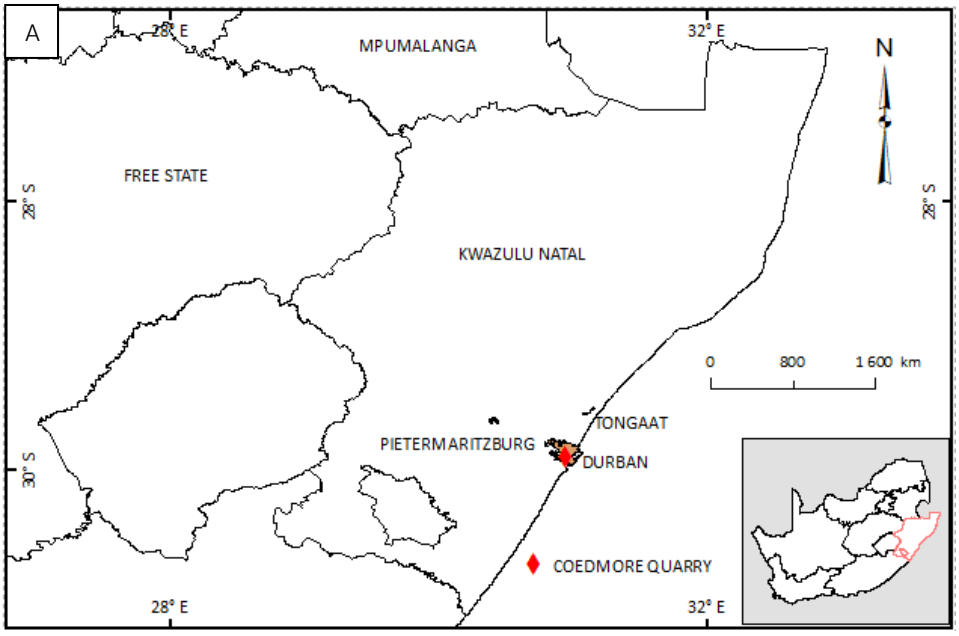

***Figure 6.2**: Image showing the area of interest. A) Map showing the study area, the Coedmore Quarry, and surrounding cities, in the KwaZulu Natal Province. B) A Google Earth image showing the bird's eye view of the Coedmore Quarry. i) A magnified image of the open pit mining quarry next to the N2 (yellow road).*

6.3. Results

6.3.1. Macroscopic (hand specimen) observations

The sample (Figure 6.3A) is a reddish-brown rock with pinkish and cream-white grains. It is finely grained with some visible quartz grains exhibiting a sugar-like texture. The rock is dominated by approximately 65% quartz, along with lesser amounts of plagioclase, feldspars, mica, and calcite (Figure 6.3(i)). No sulphides are observed.

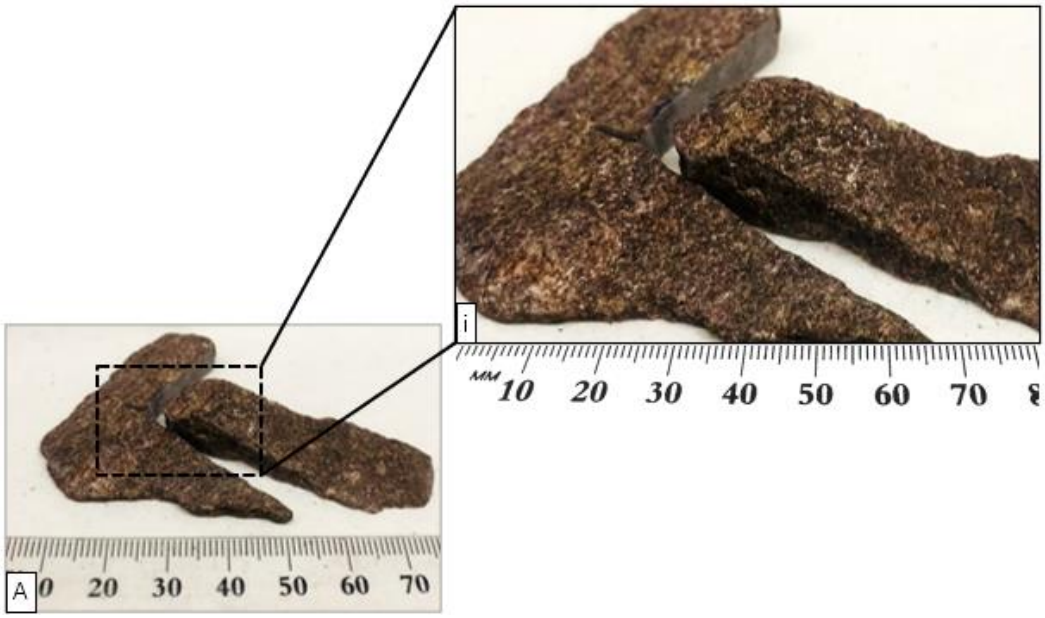

Figure 6.3: Hand specimen image for Natal rock. A) A reddish-brown rock with pinkish and cream-white grains. Grainy quartz is observed. i) Minerals observed quartz, along with less amounts of plagioclase, feldspars, mica, and calcite. No sulphides are observed.

6.3.2. Petrographic analysis

Petrographic examination (Figure 6.4A-D) show that the rock is characterised by fine- to medium-grained (0.5-2 mm) crystals composed of approximately 66% quartz, 15% orthoclase, 7% plagioclase, 5% microcline, 5% muscovite + sericite, 1% biotite, and 1% opaque mineral. The minerals show no preferred orientation. The magnified microscopic images (Figure 6.4B-D) reveal that the rock consists of medium-grained quartz, orthoclase, and plagioclase crystals, with a microscopic feldspar- and mica-rich matrix filling the interstitial spaces. The minerals are angular to semi-rounded with tangential to concavo-concave grain boundaries. Although quartz occurs as clear, monocrystalline particles with relatively smooth boundaries and exhibits straight extinction, minimal undulatory extinction is also observed in specific grains.

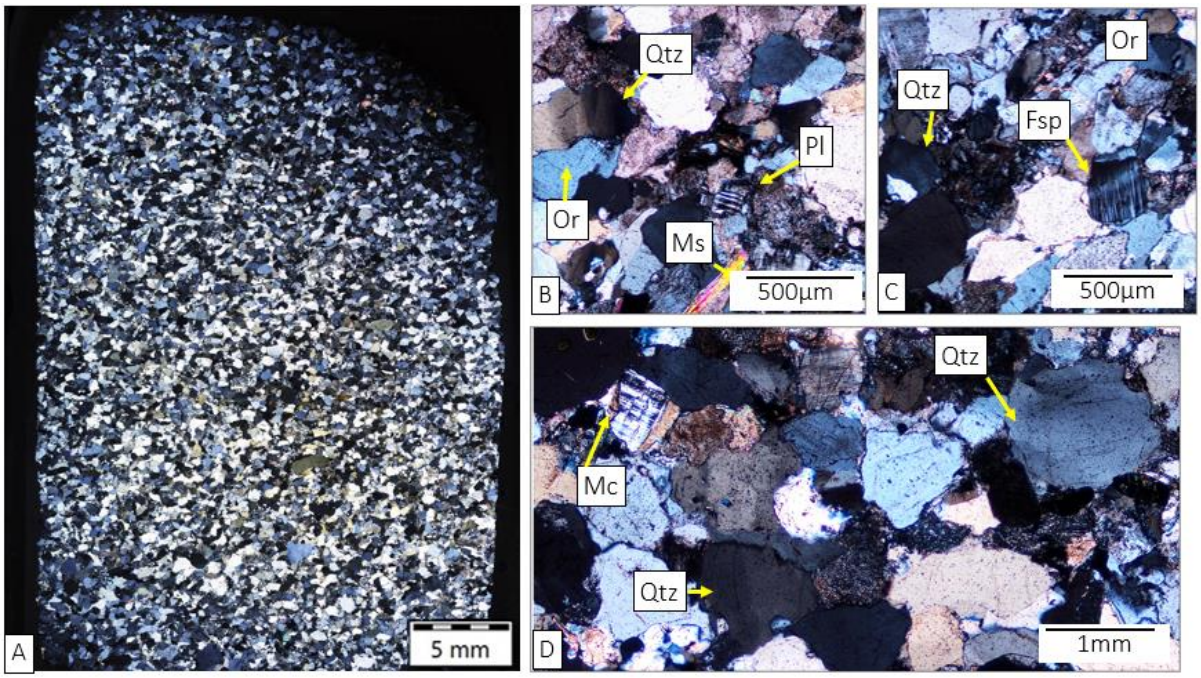

Figure 6.4: *Petrographic images of Natal rock. A) XPL image showing the fine- to medium-grained texture of the rock and minerals show no preferred alignment. There is an abundance of quartz and plagioclase grains. B) A microscopic image in XPL with magnification 4x, showing quartz crystal with undulatory extinction and elongated muscovite (Qtz= quartz, Pl= plagioclase, Ms= muscovite, and Or= orthoclase). C) A microscopic image in XPL with magnification 4x, showing quartz crystal with straight extinction (Fsp= feldspar). D) A microscopic image in XPL with magnification 4x, showing quartz crystals with weak undulose extinction and smooth boundaries as well as the presence of microcline (Mc=microcline).*

6.3.3. TIMA analysis: phase maps and elemental maps

Phase maps (Figure 6.5A-B) reveal that the rock has high quartz content and contains lesser amounts of orthoclase and albite, as well as minor biotite. The spatial relationship observed shows that quartz is homogeneously distributed along with equally dispersed fine-grained orthoclase and albite. The enlarged image (Figure 6.5B) indicates that quartz varies from fine-grained, less than 1 mm, to medium-grained, more than 1 mm, while the other minerals are less than 1 mm. The image also shows an association between orthoclase and muscovite.

Element maps (Figure 6.5C-E) reveal that Si occurs in higher concentrations than K and Al, with the highest Si concentrations associated with quartz. Low Si and high Al is associated with orthoclase and albite, whereas high K concentrations are associated with orthoclase and muscovite (Figure 6.5E).

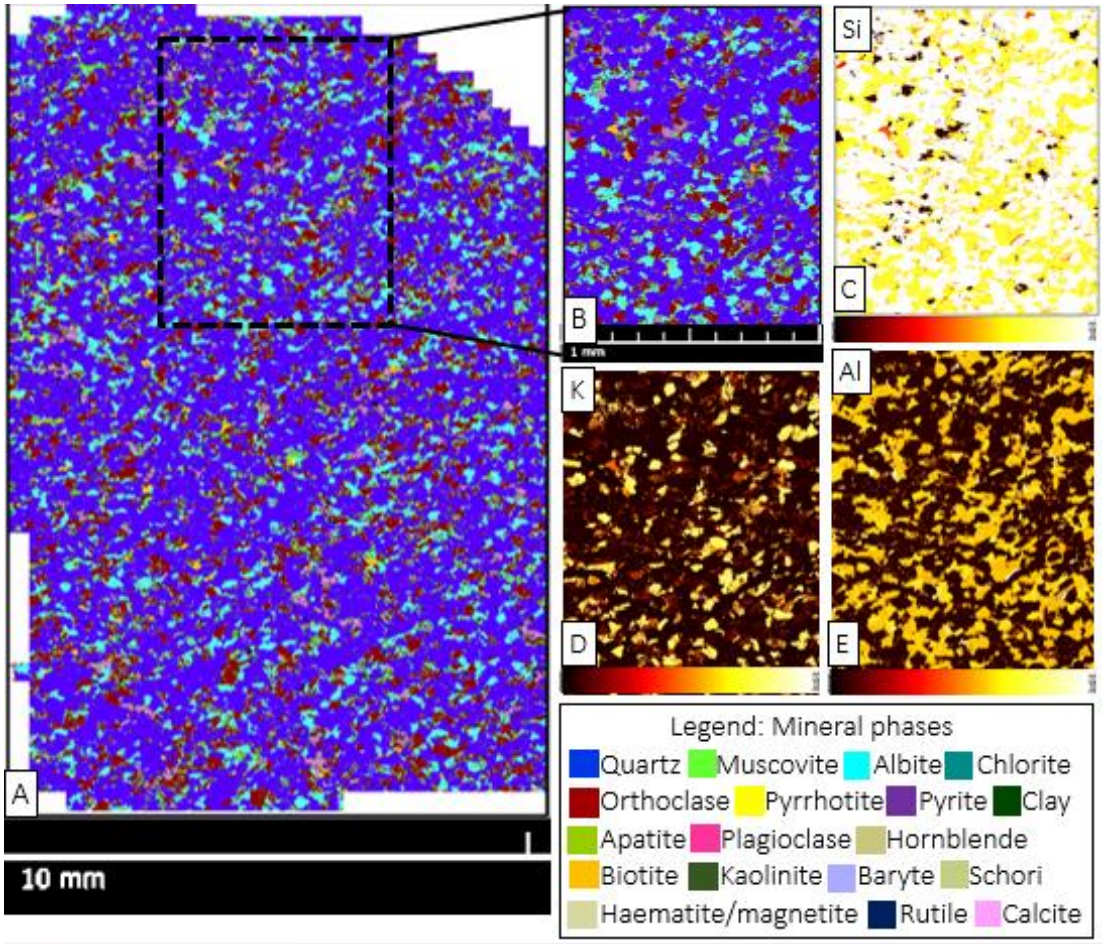

Figure 6.5: TIMA images of Natal rock. A) Phase maps showing the dominance of quartz with less albite and orthoclase. The spatial relationship reveals that albite and orthoclase are homogeneously dispersed, along with disseminated biotite and muscovite. B) Magnified image of phase maps showing coarse quartz with finer orthoclase, albite, dispersed calcite, plagioclase, biotite, and muscovite. C) Si elemental map showing variations in Si concentrations, with the highest concentrations associated to quartz. D) K elemental map showing moderate concentrations associated with orthoclase and albite. E) Al elemental map showing high to moderate concentrations associated to orthoclase, muscovite, biotite, and albite.

6.3.4. Modal abundance

Modal abundances for the rock sample were obtained using TIMA and XRD analyses (Figure 6.6, Appendix 3 and 4). Both analyses reveal that the rock is quartz-rich and contains more than 20% feldspar. XRD detected 9.4 wt. % microcline and 11.6 wt. % plagioclase, whereas TIMA found 12.96% albite and 13.16% orthoclase. Additionally, TIMA shows that the rock contains accessory amounts of plagioclase, chlorite, and haematite, which were not detected by XRD.

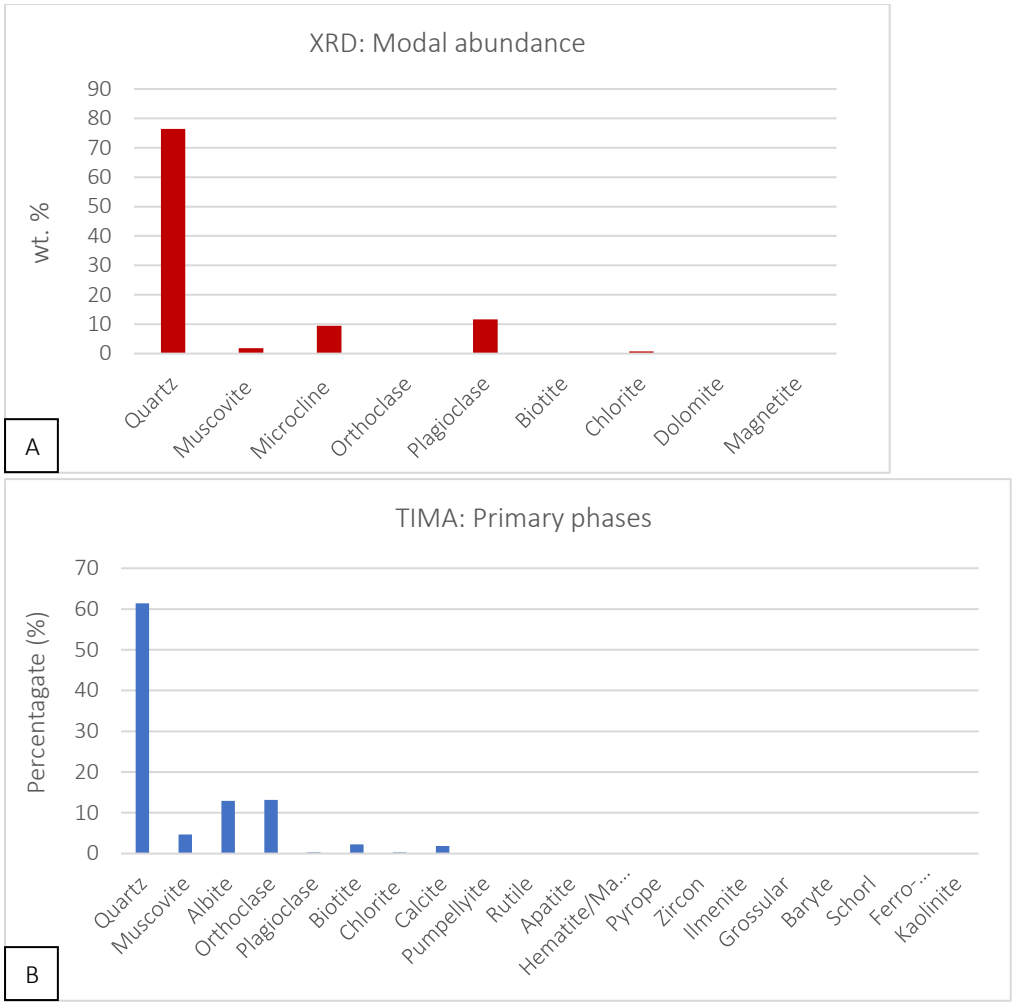

Figure 6.6: *Graphs showing the mineral abundance of the Natal rock. A) XRD results (in wt. %) show that quartz makes the bulk composition with a secondary abundance of plagioclase and microcline as well as accessory chlorite. B) TIMA results (in %) show that quartz is the dominant primary phase, followed by orthoclase and albite and accessory plagioclase, chlorite, and haematite.*

6.3.5. Accelerated Mortar Bar (SANS 6245)

SANS 6245 test results for the specimens were averaged and are as follows: after day one of curing, the average expansion was 0.02%. After seven days of curing, the average expansion was 0.03%, and on day fourteen of curing, the specimen had an average expansion of 0.06% (Table 6.2). The graph in Figure 6.7 shows an increasing trend of expansion over fourteen days. Although there is a general increase in expansion, fluctuations are observed between day five and day eleven.

Table 6.2: *Mean expansion percentages with days for Natal rock (CQ)*

Time	*Expansion %*
D1	0.02
D7	0.03
D14	0.06

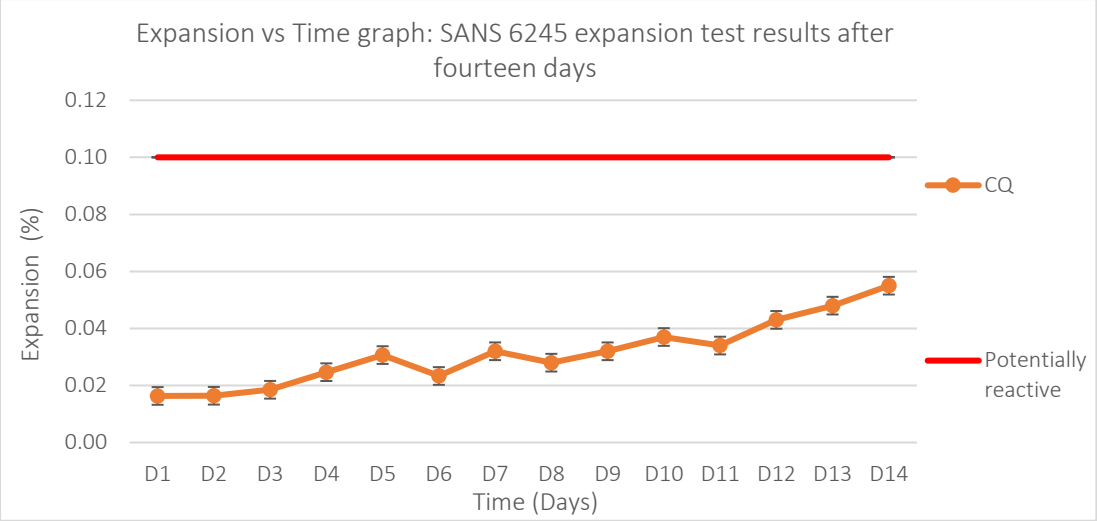

Figure 6.7: *Image showing a graph for the expansion test results using Natal CQ aggregate for* SANS 6245 *after fourteen days of immersion in NaOH solution.*

6.4. Discussions

6.4.1. Geological characteristics and classification for the Natal aggregate

The rock from the Natal Group is a quartz-rich rock defined by medium-grained crystals and contains more than 25% feldspar. It is interstitially filled by a microscopic feldspar- and mica-rich matrix, thus identifying the rock as arkosic sandstone. Although in South African concrete production the rock is nominally identified as quartzite, it showed no metamorphic textures or deformation features. The Natal arkosic sandstone comprises quartz with smooth boundaries and exhibits straight extinction, with a few crystals showing weak undulose extinction. This suggests that the rock was not subjected to significant strain, suggesting minimal distortion of the quartz crystalline structure (Blight and Alexander, 2011; Fernandes *et al.*, 2016; Leeman *et al.*, 2016; Tiecher *et al.*, 2018). Being dominated by quartz and feldspars, the rock is rich in silica and aluminium.

6.4.2. Expansion results for the Natal arkosic sandstone

The Accelerated Mortar Bar Test, SANS 6245, was carried out over fourteen days, with three specimens, containing a single composition of the Natal arkosic sandstone immersed in NaOH solution. The changes in strain were recorded daily. For the first five days, there was an incremental increase in expansion, and from days six to twelve, fluctuations were observed (Appendix 5 and 6). On day fourteen, all specimens showed less than 0.1% expansion, which is classified as non-reactive by Oberholster and Davis (1986) (Table 2.8). Thus, the Natal Group arkosic sandstone aggregate is non-reactive.

6.5. Closure

This chapter focused on the Natal arkosic sandstone sampled from the Coedmore Quarry. This sedimentary rock is a medium-grained, quartz-dominant and feldspar-rich rock, characterised by quartz crystals with smooth boundaries and straight extinction. The arkosic sandstone used in the AMBT (SANS

6245), showed non-expansive behaviour (with an expansion of 0.06%). The expansion results, deem the Natal arkosic sandstone as a non-alkali reactive aggregate.

CHAPTER SEVEN

7. The Cape Granite Suite granite

7.1. Geological setting

The igneous activity associated with the late Precambrian Saldania orogen in South Africa's Western Cape Province resulted in the intrusion of a suite of granitoid rocks with varying compositions (Jordan *et al*., 1995; Scheepers, 1995; Harris *et al*., 1997). These gabbroic to granitic batholiths form the Cape Granite Suite (CGS) which extends 500 km along the western and southern Cape coast (Harris *et al*., 1997). The CGS is geospatially separated into three groups of batholiths: the southwestern group neighbouring Cape Town, the northern group near Orange River, and the eastern group near George (Harris *et al*., 1997; Scheepers and Schoch, 2006; Buggisch *et al*., 2010). The eastern batholith is made up of George and Woodville plutons which are the most notable, however only appear as small, exposed outcrop on the Sardina Bay (Scheepers and Schoch, 2006). The northern pluton, consisting of the Kuboos, Swartbank, and Tatasberg plutons, is presumably associated with the final phase of CGS magmatism and forms part of Northern Cape and Namibia (Scheepers, 1995; Scheepers and Schoch, 2006). The southwestern batholith is described by distinctive regions attributed to the northwest-southeast-trending Colenso Fault and multiple phases of magmatism (Scheepers and Schoch, 2006; Buggisch *et al*., 2010).

The spatial distribution of the southwestern granites reflects regional tectonic limits and are structurally segmented into three terranes, Boland terrane, Swartland terrane, and Tygerberg terrane, separated by significant NW trending shear zones (Harris *et al*., 1997; Scheepers and Schoch, 2006). These terranes are further partitioned into major batholiths: Malmesbury and Paarl-Wellington of the Swartland terrane; Darling, Stellenbosch-Kuils River, and Peninsula of the Tygerberg terrane and Saldanha-Vredenburg batholith on the boundary between Swartland and Tygerberg (Figure 7.1) (Harris *et al*., 1997; Scheepers and Schoch, 2006; Buggisch *et al*., 2010; Villaros, 2010). These six plutons have been individually classed into three types of granites- A-type, I-type, and S-type- based on mineralogy, accessory mineral content, and geochemical characteristics (Figure 7.1 and Table 7.1) (Scheepers, 1995; Harris *et al*., 1997; Scheepers and Schoch, 2006). Each granite type is further classified into subcategories (Table 7.1) (Scheepers, 1995; Scheepers and Schoch, 2006). The older intrusives from the first phase of magmatism are predominantly S-type (peraluminous) granites found near the coast and west of the northwest-southeast trending Colenso Fault and in the Tygerberg terrane (Figure 7.1) (Harris *et al*., 1997; Scheepers and Schoch, 2006; Buggisch *et al*., 2010; Villaros, 2010). These older granites are characterised by pervasive deformation features, caused by tectonic changes which

resulted in the subsequent, second phase, magmatism (Scheepers, 1995; Harris *et al*., 1997; Mhlanga, 2021). The second phase intrusives are mainly I-type (metaluminous) and are represented by felsic plutons found in the Swartland terrane (Harris *et al*., 1997; Scheepers and Schoch, 2006; Buggisch *et al*., 2010). These granites do not possess any deformation features because they occurred post-tectonic (Harris *et al*., 1997; Scheepers and Schoch, 2006; Buggisch *et al*., 2010). The third phase granites are A-type granites that form small plutons in the Tygerberg and Swartland terranes (Figure 7.1) (Scheepers, 1995; Harris *et al*., 1997). Unlike the I-type and S-type, defining A-type granites has been a source of contention however the general consent states that A-type refers to anorogenic, anhydrous, and alkaline granites (Scheepers and Schoch, 2006; Frost and Frost, 2019). Additionally, a fourth phase magmatism occurred resulting in the youngest CGS igneous rocks (Scheepers, 1995; Harris *et al.,* 1997; Scheepers and Schoch, 2006; Villaros, 2010). The fourth phase is composed of extrusives and intrusives consisting of ignimbrite, tiff site, and quartz porphyry found in the Tygerberg terrane (Scheepers, 1995; Harris *et al*., 1997; Scheepers and Schoch, 2006; Villaros, 2010).

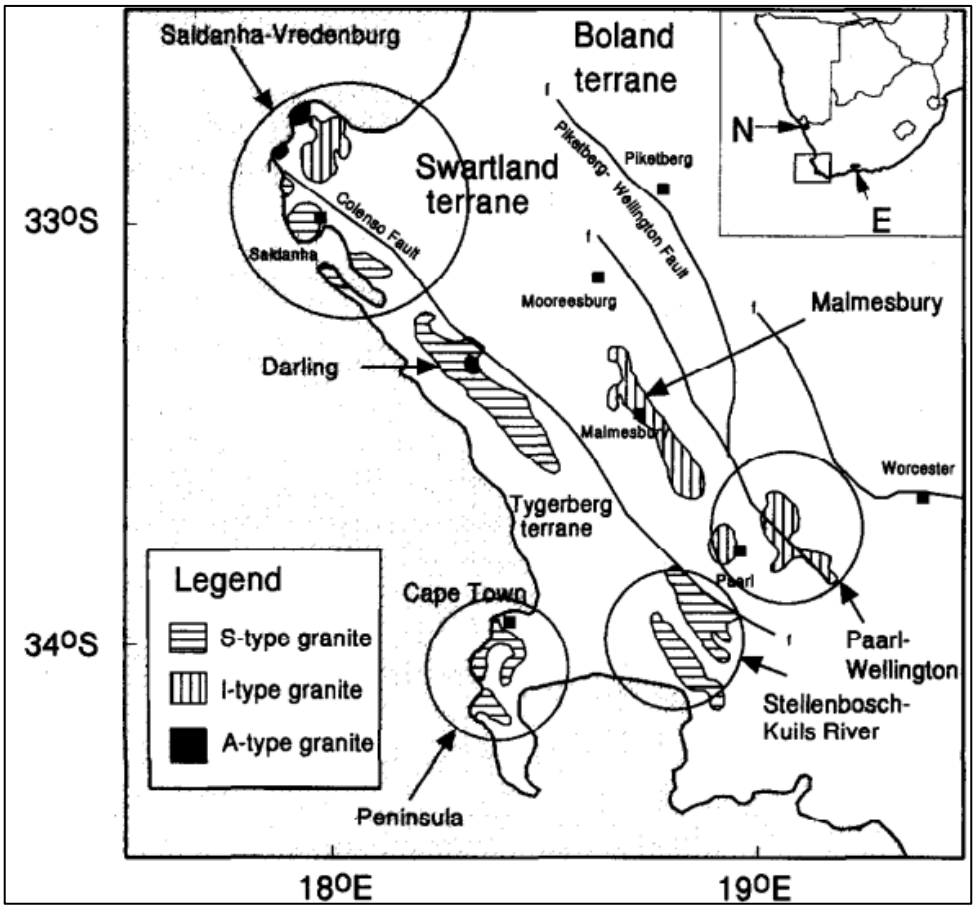

Figure 7.1: The distribution of granite plutons in the Western Cape Province. The S-type granite is located in the Peninsula, Stellenbosch-Kulis River, Darling, and Saldanha-Vredenburg batholiths. The I-type is in the Malmesbury, Paarl-Wellington batholith (Harris et al., 1997).

Table 7.1: *Table showing the different magmatic phases of the CGS with the associated granite-type, rocks, and mineralogy (adapted from Scheepers, 1995; Harris et al., 1997; Scheepers and Schoch, 2006; Villaros, 2010).*

Phase	*Granite-type*	*Associated rocks, mineralogy,*
Phase IV	-	*Volcanic type rocks- Ignimbrite, tuffisite, quartz porphyry*
Phase III	A-type	*Quartz syenites, biotite-synites, alkali feldspar granites*
		Ab — Subsolvus granites with partially chloritized Fe-rich biotite, microcline microperthite, and less albitic plagioclase. Accessory zircon, allanite, titanite, and monzanite.
		Aa — Varies amphibole -quartz synites to alkali feldspar granites. Albitisation of microcline microperthite along with partially chloritized Fe-rich biotite. Accessory magnetite, zircon, monzanite, and thorite.
Phase II	I-type	*Alkali feldspar granites, monzogranite, granites*
		Ib — Equigranular rock with microperthite, albitic plagioclase, and biotite. Occurrence of chloritised biotite and saussuritised plagioclase cores. Accessory apatite, allanite, titanite, monzanite, thorite, and zircon.
		Ia — Varies from porphyritic to equigranular monzogranite to granite rock. Presence of microcline microperthites along with partially chloritised biotite and hornblende. Accessory apatite, allanite, titanite, zircon, magnetite, fluorite, and epidote
Phase I	S-type	*Granodiorites, biotite granites, granites*
		Sb — Coarse-grained granitic rock. Biotite and hornblende present, and accessory apatite, tourmaline, monzanite, and zircon
		Sa2 — Muscovite and biotite rich, with albite and accessory apatite, tourmaline, monzanite, zircon, and garnet
		Sa1 — Feldspar to microcline dominant with less muscovite. Accessory apatite, tourmaline, monzanite, zircon, and garnet

7.2. Area of interest

The Rheebok Quarry, with coordinates 33˚24’11.18” S 18˚42’43.36” E, is located in the Abbotsdale rural settlement in the West Coast District Swartland Municipality, of the Western Cape Province. It is situated near the town of Malmesbury, which is approximately 65 km north of Cape Town, South Africa

(Figure 7.2A). The opencast mining quarry (Figure 7.2B-(i)), found near the N7, is known for mining and processing granite of the Cape Granite Suite to produce concrete aggregates.

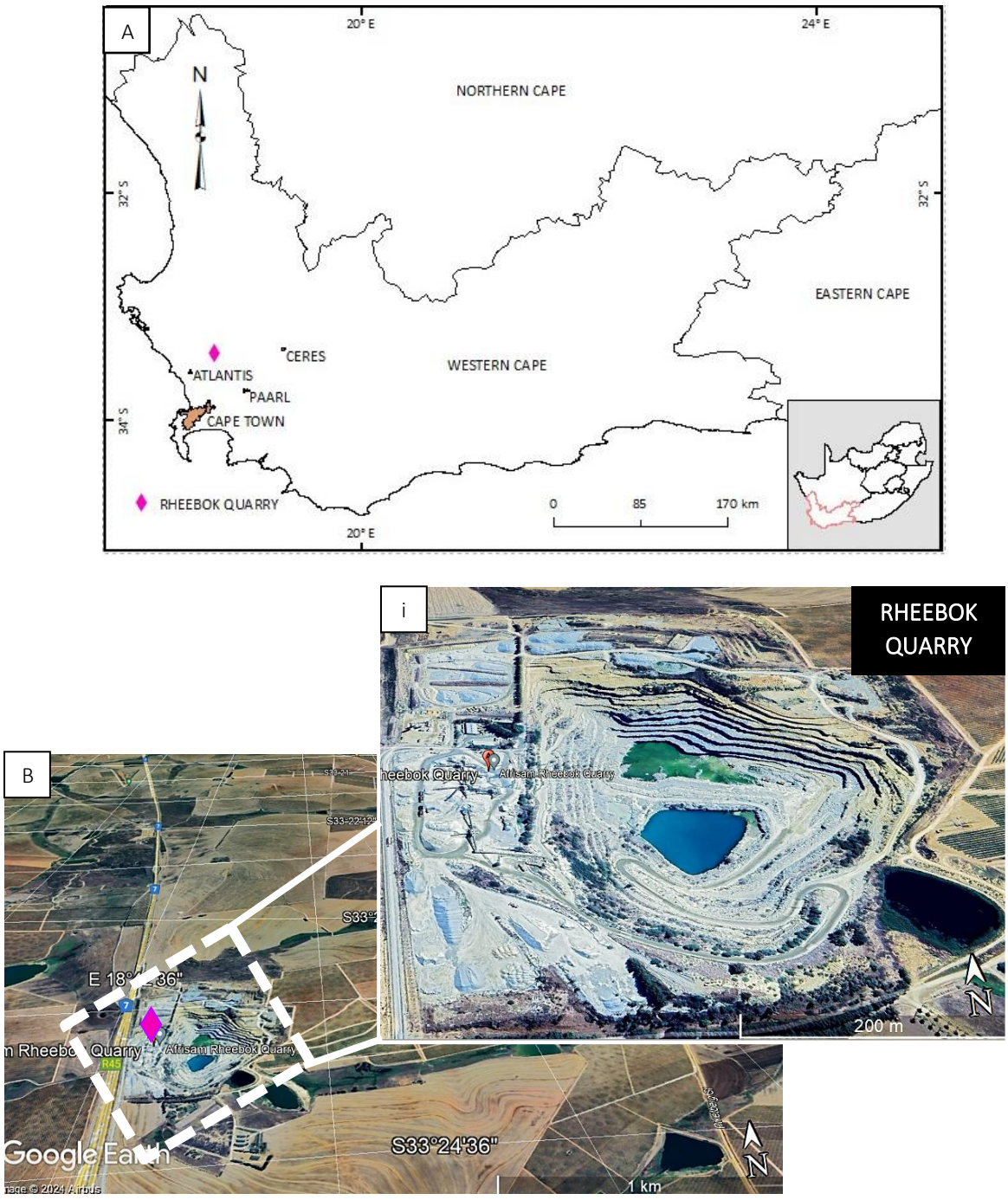

Figure 7.2: Image showing the area of interest. A) Map showing the study area for the Rheebok Quarry and surrounding cities, in the Western Cape Province. B) A Google Earth image showing the bird's eye view of the Rheebok Quarry next to the N7 (yellow road). i) A magnified view of the opencast mining quarry.

7.3. Results

7.3.1. Macroscopic (hand specimen) observation

In the hand sample, the granite is an equigranular, intrusive felsic rock, characterized by a balanced mix of dark and light minerals, with minor pink and black grains visible (Figure 7.3A). The rock also exhibits

a subtle green hue. The minerals identified include plagioclase, quartz, K-spar, hornblende, biotite, muscovite, and chlorite (Figure 7.3(i)). Notably, some plagioclase and quartz grains are slightly coarser compared to the other minerals.

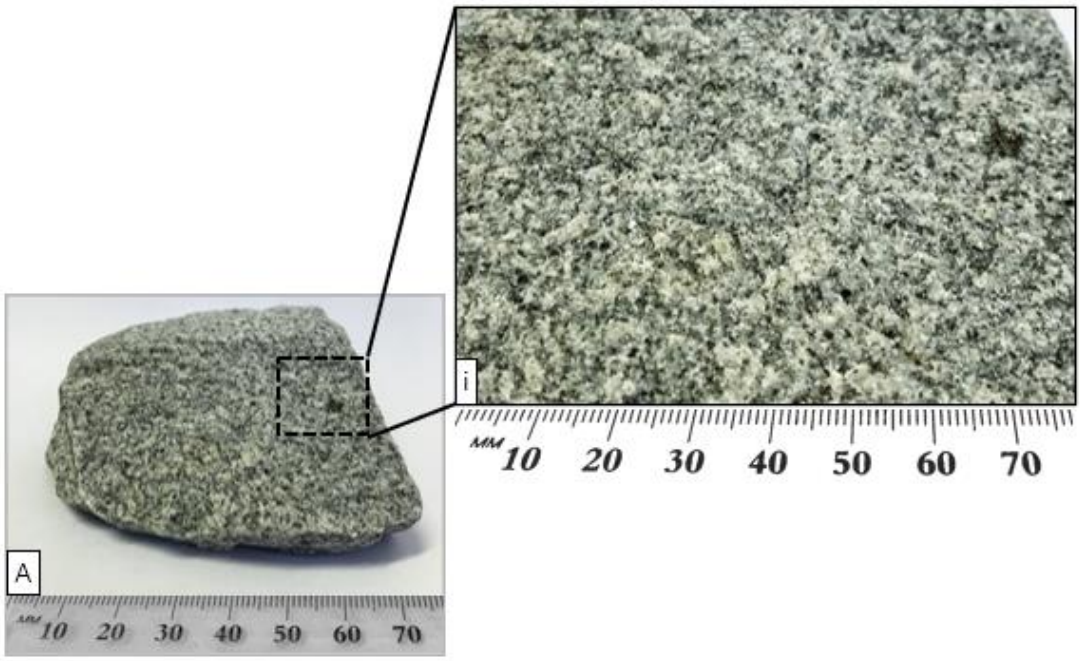

Figure 7.3: An image of the granite hand specimen. A) Shows the intrusive and felsic attributes of the rock. i) An enlarged area of rock showing a combination of dark and light minerals with a slightly green hue. Minerals observed include plagioclase, quartz, K-spar, hornblende, biotite, muscovite, and chlorite. Some of the plagioclase and quartz grains appear to be slightly coarser than other minerals.

7.3.2. Petrographic analysis

Petrographic analysis (Figure 7.4A-E) shows that the sample is fine- to medium-grained and contains approximately 45% plagioclase, 45% quartz, and 5% biotite. Microscopic examination (Figure 7.4B-E) further reveals trace amounts of muscovite, chlorite, hornblende, pyroxenes, and apatite. In the PPL and XPL images (Figure 7.4B-C), biotite appears as euhedral to subhedral grains, varying from elongated to semi-orthorhombic crystals, with chlorite present at the rims and core of biotite grains. Plagioclase occurs as subhedral to anhedral crystals, exhibiting alteration of microscopic mica grains at their cores (Figure 7.4D-E). Quartz appears as colourless crystals with no recrystallisation or subgraining, with most grains showing straight extinction. The images also indicate the presence of well-developed quartz and feldspar crystals with straight to slightly curved boundaries. Micrographic textures (Figure 7.4E) and microcrystalline material (Appendix 11) are observed in the interstitial spaces.

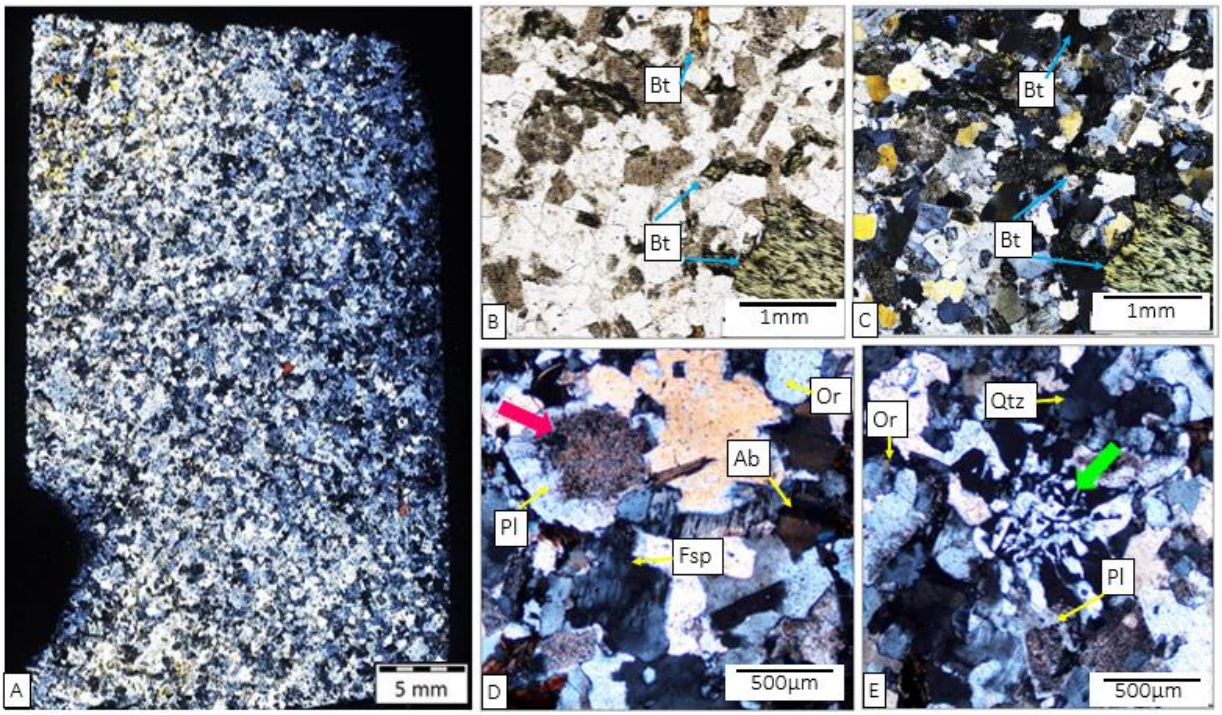

Figure 7.4: *Petrographic images of granite. A) XPL image showing equigranular textured granite and abundance of quartz and plagioclase grains. B) A microscopic image in PPL with magnification 4x, showing greenish brown pleochroism of biotite (chloritisation of biotite (Bt)). C) The XPL version of image B shows chloritised biotite. D) A microscopic image in XPL with magnification 4x, showing medium- to coarse-grained plagioclase, quartz, orthoclase, and albite. The pink arrow highlights saussuritisation of plagioclase cores (Qtz= quartz, Pl= plagioclase, Bt= biotite, Or= orthoclase, Ab= albite, and Fsp= feldspar). E) A microscopic image in XPL with magnification 4x, showing micrographic texture in green and saussuritisation of plagioclase cores.*

7.3.3. TIMA analysis: mineral phase and element maps

Phase maps (Figure 7.5A-B) demonstrate that the granite is enriched in orthoclase, quartz, and albite, with all minerals homogeneously distributed throughout the rock. The enlarged phase maps (Figure 7.5B) reveal fine-grained muscovite, calcite, and hornblende crystals at the core of plagioclase. Additionally, biotite is strongly associated with chlorite, with some biotite crystals found along chlorite boundaries and others located within biotite cores.

Elemental maps (Figure 7.5C-E) indicate high concentrations of Si, K, and Al. The highest Si concentrations are associated with quartz, K is associated with orthoclase, and Al with orthoclase, albite, and plagioclase.

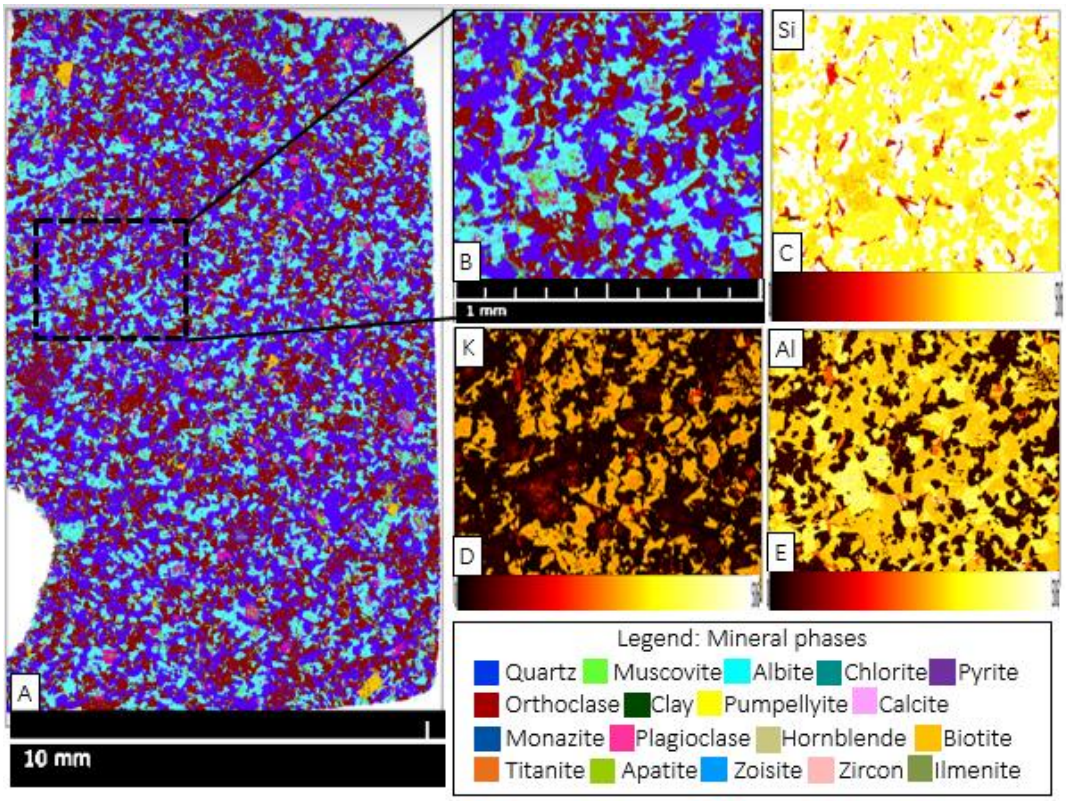

Figure 7.5: TIMA images of granite. A) A mineral phases map, showing equal distribution of quartz, orthoclase, and albite. B) An enlarged mineral phases map image focusing on the demarcated area showing coarse quartz, orthoclase, and albite, along with dispersed calcite, plagioclase, biotite, and muscovite. C) An element map showing variations in Si concentrations, with the highest concentrations (in white) associated with quartz and the lower concentrations with orthoclase, albite, biotite, and plagioclase. D) An element map showing moderate concentrations of K, associated with orthoclase. E) An element map showing high (in yellow) Al concentrations, associated with orthoclase, albite, and plagioclase. Low Al concentrations are associated with quartz.

7.3.4. Modal abundance

The modal abundance for the granite sample was determined using XRD and TIMA analyses (Figure 7.6, Appendix 3 and 4). Both analyses reveal the granite comprises of less than 40% quarts though compositional variations are noted in the feldspars. TIMA analysis (Figure 7.6B) detected 29% orthoclase, 22% albite, and 3.42% plagioclase, whereas XRD (Figure 7.6A) found 0 wt. % orthoclase, 22 wt. % microcline, and 29 wt. % plagioclase. Additionally, TIMA detected minor amounts of biotite and chlorite, along with accessory minerals such as titanite, hornblende, zircon, and allanite. In contrast, XRD found minor amounts of chlorite however did not detect biotite (Figure 7.6B).

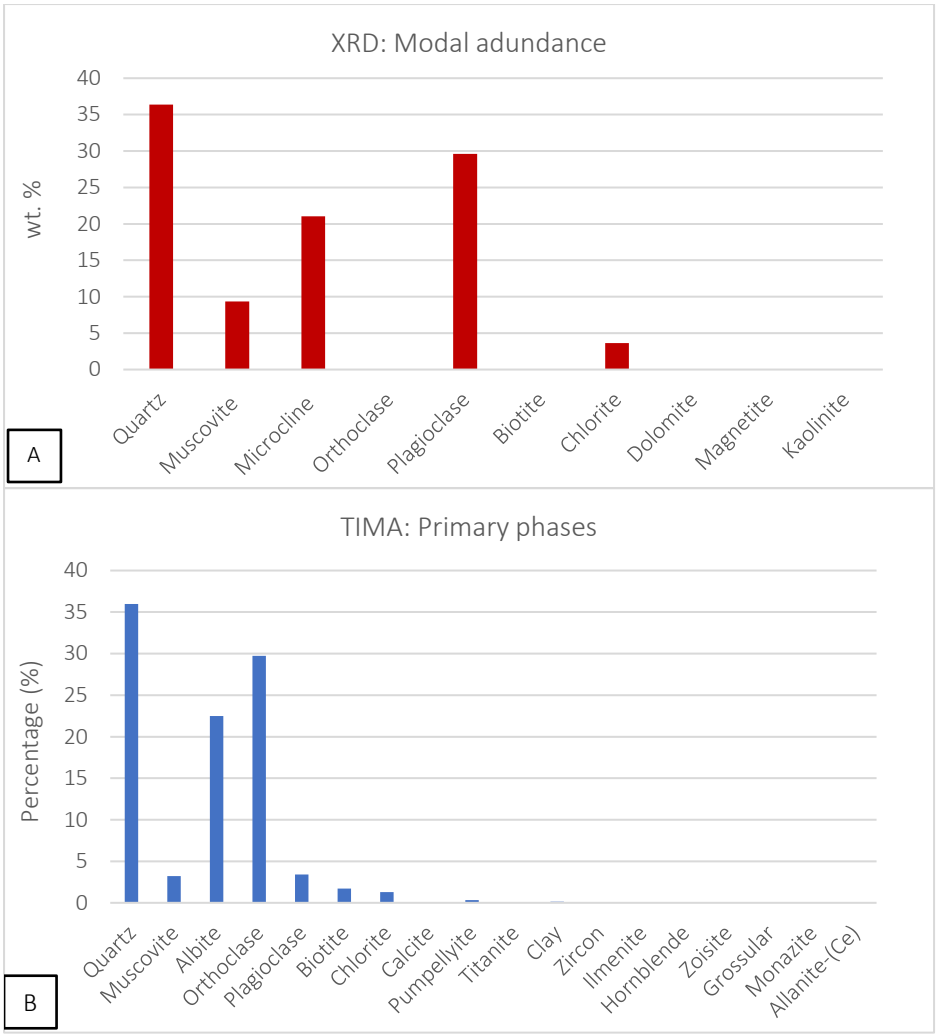

***Figure 7.6**: Graphs showing the mineral abundance of granite sample. A) XRD results (in wt. %) show that quartz, microcline, and plagioclase make up the bulk composition. B) TIMA results (in %) show that quartz, albite, and orthoclase are the dominant primary phases. Rock also contains accessory titanite, hornblende, zircon, and allanite.*

7.3.5. Accelerated Mortar Bar Test (SANS 6245)

The SANS 6245 test results for the specimen are summarized in Table 7.2 and Figure 7.7. After one day of curing, the average expansion was 0.02%. This expansion remained constant at 0.02% after seven days of curing. By day fourteen, the average expansion had increased to 0.04%. The graph in Figure 7.7 illustrates the variation in expansion over the fourteen days, showing a notable decrease on days ten and eleven indicating a slight fluctuation in the expansion rate during the curing process.

***Table 7.2:** Mean expansion percentages with days for granite (RG) sample*

Time	*Expansion %*
D1	0.02
D7	0.02
D14	0.04

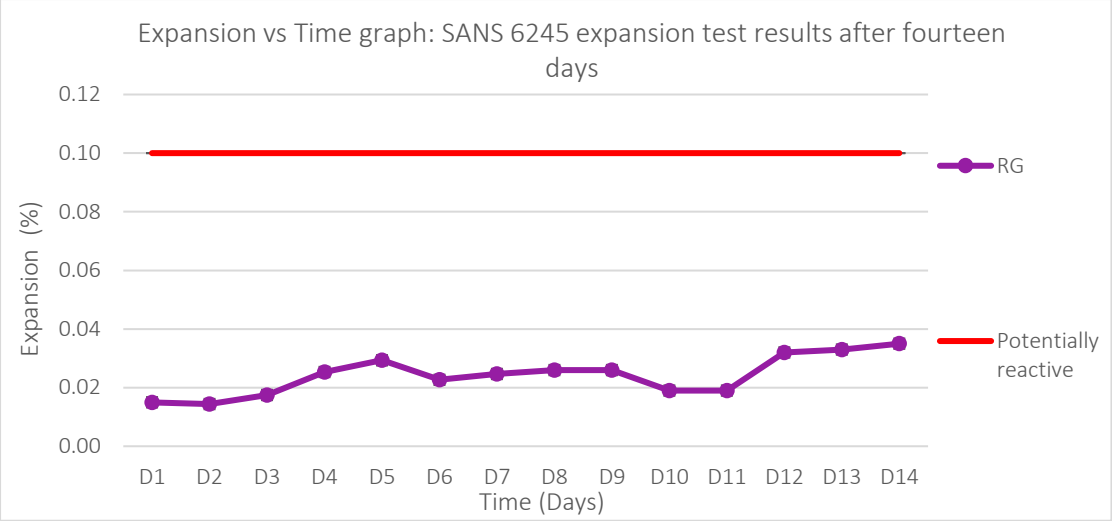

***Figure 7.7**: Image showing a graph for the expansion test results using granite (RG) aggregate for SANS 6245 after fourteen days of immersion in NaOH solution.*

7.4. Discussions

7.4.1. Geological characteristics and classification of the CGS granite

The CGS granite rock used in this research is an equigranular textured rock, characterized by higher concentrations of quartz and plagioclase, and a lower concentration of potassium feldspar (K-spar). This rock exhibits both intrusive textures, such as medium-grained crystals, and extrusive textures, in the form of microscopic material in the interstitial spaces, as well as micrographic textures. These features suggest that the rock formed as a result of sub-solid recrystallisation (Frost and Frost, 2019). CGS rocks are part of a suite of granitoids differentiated by their composition, which helps in understanding the geological processes that the rock has undergone. Modal abundance results identify this rock as a monzogranite (Figure 7.8). The presence of biotite, alteration of the more anorthitic plagioclase cores, partial replacement of biotite by chlorite, and accessory minerals such as hornblende, allanite, titanite, and zircon (Figure 7.4-7.6), categorises this monzogranite as an Ib, I-type granite (Scheepers, 1995; Harris *et al*., 1997; Scheepers and Schoch, 2006; Villaros, 2010*).* I-type granites are younger than the heavily deformed S-type granites, as they formed during phase II, post-tectonic events, and thus are not deformed (Scheepers, 1995; Harris *et al*., 1997; Mhlanga, 2021). Given that monzogranite is dominant by quartz, orthoclase, and albite feldspar, these minerals are enriched in silica, aluminium, and sodium (Appendix 12). Although undulose extinction is typically associated with deformation, the weak undulose extinction observed in certain quartz grains (Appendix 11) within the monzogranite may be attributed to the stresses induced by the cooling and uplifting of the igneous body rather than deformation (MacKenzie *et al*., 2017).

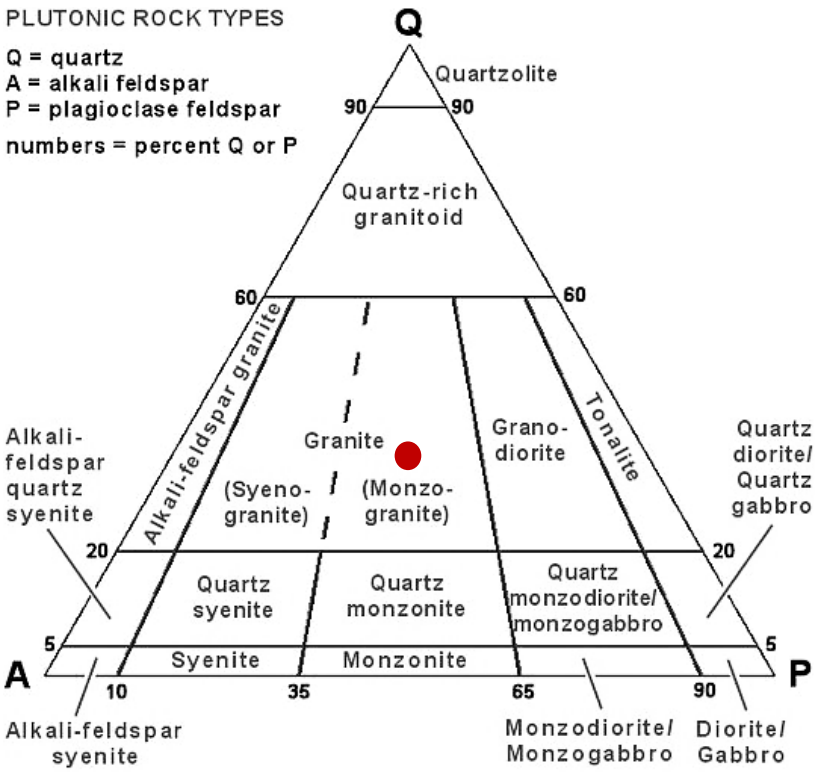

Figure 7.8: Image showing the Q-K-P-FOID Plutonic Streckeisen Diagram and the classification of CGS granite rock used in this study (shown by the circle) (modified Le Bas and Streckeisen, 1991).

7.4.2. Expansion test results for the CGS monzogranite

Accelerated Mortar Bar Test, SANS 6245, was conducted over fourteen days, with three specimens made from only the CGS monzogranite immersed in a NaOH solution and closely monitored for changes in strain. Although temperature affected the strain readings, fluctuations were observed over the fourteen days, and the specimens exhibited less than 0.1% expansion on day fourteen (Appendix 5 and 6). According to Oberholster and Davis (1986), an expansion of less than 0.1% on day fourteen classifies the aggregate as non-reactive (Table 2.8). Therefore, the monzogranite from the Swartland terrane near the Malmsebury pluton, part of the CGS, is a non-alkali reactive aggregate.

7.5. Closure

This chapter presented on the CGS monzogranite sampled from the Rheebok Quarry. This rock igneous rock is a medium-grained rock, composed of quartz, plagioclase, and K-feldspar. It is characterised by both intrusive and extrusive textures, chloritisation of biotite and saussuritisation of plagioclase cores. The quartz grains in this rock are pure, medium-grained crystals exhibiting straight extinction (with a few grains showing weak undulatory extinction). The monzogranite used in the AMBT (SANS 6245), showed non-expansive behaviour. The expansion results, classify the CGS monzogranite as a non-alkali reactive aggregate.

CHAPTER EIGHT

8. The Malmesbury Group wacke

8.1. Geological setting

The Malmesbury Group is a collection of supacrustal rocks that underlie the western Saldania Belt (Mhlanga, 2021). The Saldania Belt is a low-grade metamorphic fold belt trending in the NW-SE direction and extensively outcrops approximately 80 km x 100 km (Scheepers, 1995; Rozendaal *et al.,* 1999; Kisters *et al*., 2002; Mhlanga, 2021). The belt's metamorphism is correlated to deformation and folding during the Saldania orogeny however the subdivision of its lithostratigraphy has been a source of contention (Bailie and Weber, 2024). Several scholars proposed that the Saldania Belt is underlain by three allochthonus separated by three terranes whereas others opposed this theory by proposing two terranes instead of three (Kisters *et al*., 2002; Mhlanga, 2021). However, a more recent theory proposed by Kisters and Belcher (2018) has seemed to be more viable. Kisters and Belcher proposed that the western Saldania Belt is divided into two domains-the Malmesbury Group and Swartland Complex- with distinctive structural and strain histories (Kisters and Belcher, 2018; Mhlanga, 2021).

The Swartland Complex is the lower domain which consists of structural complexities and lithological heterogeneity whereas the upper Malmesbury Group is less complex and covers an extensive region (Belcher and Kisters, 2003; Kisters and Belcher, 2018). These domains are divided by a significant tectonostratigraphic break, which occurred because of the closure of the Adamastor Ocean during the late Neoprotezoic to Cambrian age (Jordan *et al*., 1995; Rozendaal *et al.,* 1999; Bailie and Weber, 2024). The Swartland Complex consists of a metamorphosed marine to metaturbiditic sedimentary succession and is characterised by pervasive bedding (Kisters and Belcher, 2018; Mhlanga, 2021). This lower domain is unconformably overlain by the Malmesbury Group (Belcher and Kisters, 2003).

The Malmesbury Group is a clastic marine sedimentary sequence composed of successive layers of metagreywacke, metapelite, metasandstone, metalimestone, metaconglomerate, and minor metavolcanic rocks (Cilliers, 2019; Mhlanga, 2021). It is defined by the absence of pervasive bedding-parallel schistosity and the schistose/phyllitic textures, like those of the Swartland Complex (Kisters and Belcher, 2018). Additionally, it has well-developed bedding, and the primary sedimentary features are generally well-preserved throughout the succession (Belcher and Kisters, 2003; Kisters and Belcher, 2018; Mhlanga, 2021). This upper domain is defined by the formations as summarised in Table 8.1 (Cilliers, 2019; Mhlanga, 2021; Bailie and Weber, 2024). The rocks of the Malmesbury Group are locally

metamorphosed to the lower amphibolite facies due to the intrusion of the Cape Granite Suite granites (Harris *et al*., 1997; Rozendaal *et al.,* 1999).

Table 8.1*: Malmesbury's formations and associated lithologies (modified: Cilliers, 2019; Mhlanga, 2021; Bailie and Weber, 2024).*

	Formation	*Lithology*
South-west area	Tygerberg	The succession is characterized by greywacke consisting of layered shales and siltstones, minor quantities of quartzite, impure carbonate, and conglomerate layers.
Colenso Fault		
Central area	Berg River	Contains mica schists, greywackes and quartz
	Klipplaat	Quartz-schist
	Morreesburg	Interlayered greywacke and shale units (similar to those of the Tygerberg).
	Bridgetown	Comprised of mafic metavolcanic units, chert, dolomite, and shales
	Franschhoekape	This formation is made up of feldspathic greywackes, quartzites, and conglomerates, with minor layered shales, tuffs, amygdaloidal lavas, and quarzitic porphyry dykes.
Piketberg-Wellington fault		
North-east area	Piketberg, Porterville and Norree	Interlayering of quartzite and feldspathic quartzite with siltstone and shale, greywacke, gritty sandstone, conglomerate units, and limestones.
	Brandwacht	contains andesitic metavolcanic intercalated with conglomerates, greywackes, and metapelites layers.

8.2. Area of interest

The Peninsula Quarry, with coordinates 33˚49'08.08" S 18˚32'28.43" E, is found in Killarney of the Cape Farms, located approximately 25 km north of Cape Town, Western Cape, South Africa (Figure 8.1A) (Creamer, 2018). The AfriSam owned 60-year-old quarry (Figure 8.1B), mines wacke rock and processes

it to produce a variety of concrete aggregates for the Western Cape area (Figure 8.1(i)) (Creamer, 2018; AfriSam 2021). Although the southwestern region of the Western Cape is characterised by many lithologies, the Peninsula Quarry wacke rock originates from the Malmesbury Group (AfriSam. 2021).

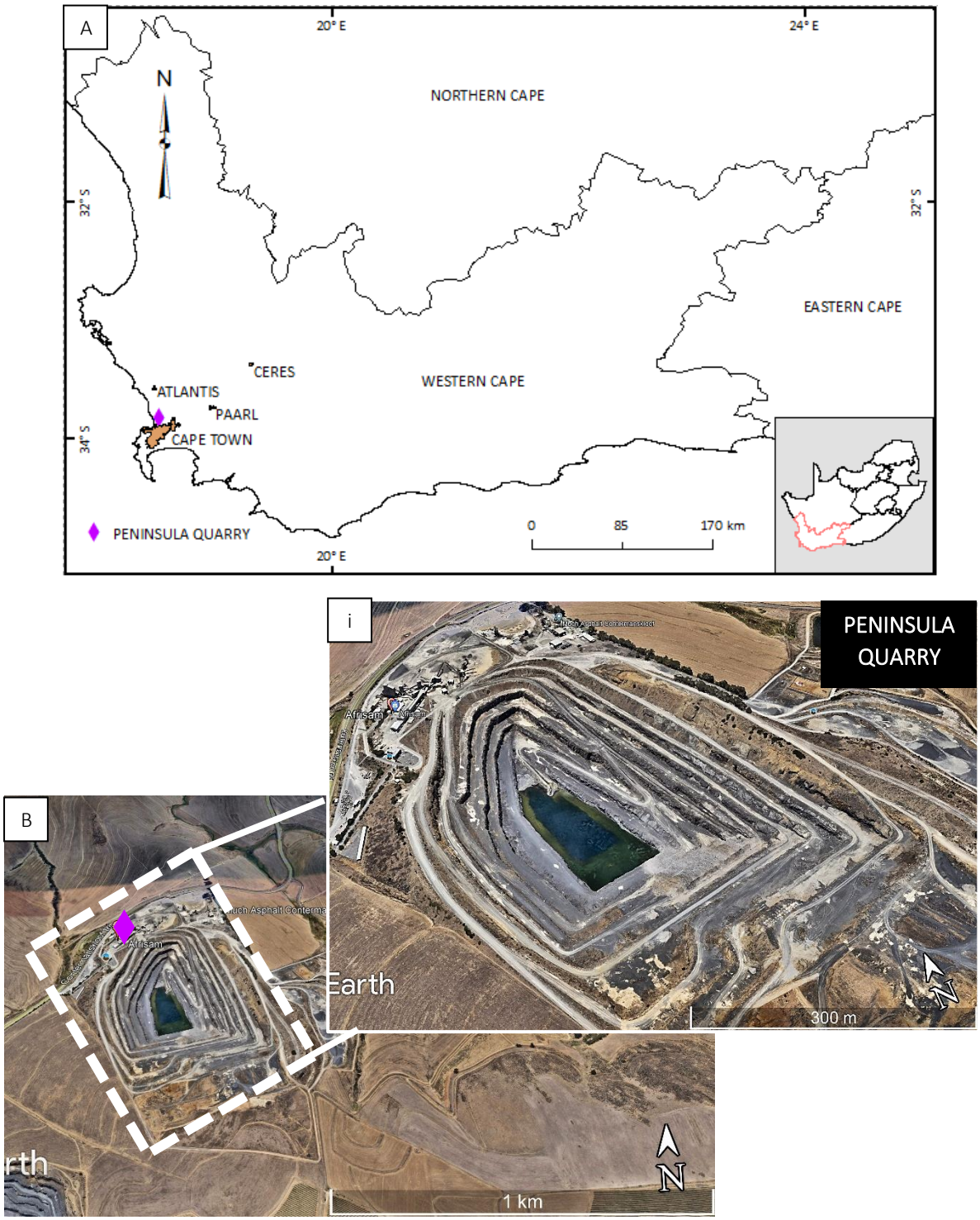

Figure 8.1: *Image showing the area of interest. A) Map showing the study area for the Peninsula Quarry located in the northern region of Cape Town and surrounding cities, in the Western Cape Province. B) A Google Earth image showing the bird's eye view of the Peninsula Quarry. i) A magnified view of the opencast mining quarry.*

8.3. Results

8.3.1. Macroscopic (hand specimen) observations

The hand specimen of the wacke (Figure 8 2A) is a finely grained, bluish-grey rock with specks of whitish fragments. The rock lacks any visible fracture orientation or metamorphic attributes (Figure 8.2(i)). Despite its dark colour, it does not exhibit any igneous textures. The primary minerals observed include quartz and mica.

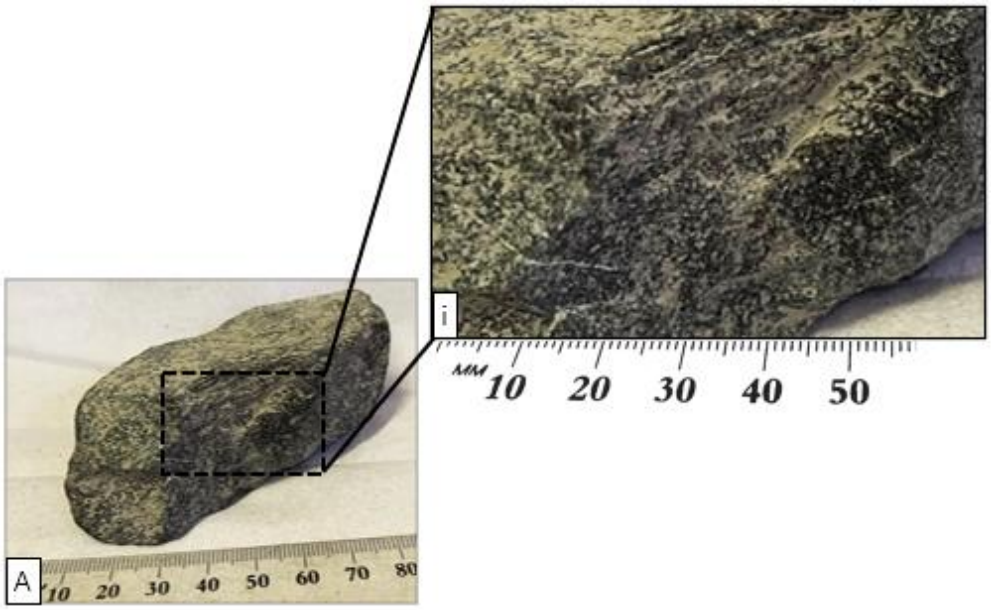

Figure 8.2: Hand specimen image of wacke. A) The rock is a finely grained bluish-grey rock with specks of whitish fragments. i) An enlarged area showing the finely grained texture of the greyish rock with no fracture orientation, nor metamorphic attributes observed.

8.3.2. Petrographic analysis

Petrographic observations (Figure 8.3A-D) reveal that wacke is fine-grained (0.1-1 mm) with minor medium-grained (more than 1 mm) lithic fragments. The minerals display no preferential alignment and occur as poorly sorted, sub-angular clasts cemented by an extremely fine-grained matrix. The petrographic images (Figure 8.3B-D) indicate that the rock is composed of quartz, orthoclase, and plagioclase, cemented by a matrix abundant in extremely fine-grained biotite and sericite, cryptocrystalline, and microcrystalline quartz, as well as trace amounts of chlorite. Plagioclase occurs as anhedral crystals, breaking down to sericite along the grain boundaries. Quartz appears as subhedral to anhedral crystals existing as polycrystalline particles with intense undulatory extinction (Figure 8.3C-D). Sutured boundaries are observed between the polycrystalline quartz particles, and the mineral boundaries are concavo-convex. Additionally, intragranular and intergranular microcracking is evident in the coarser-grained quartz crystals.

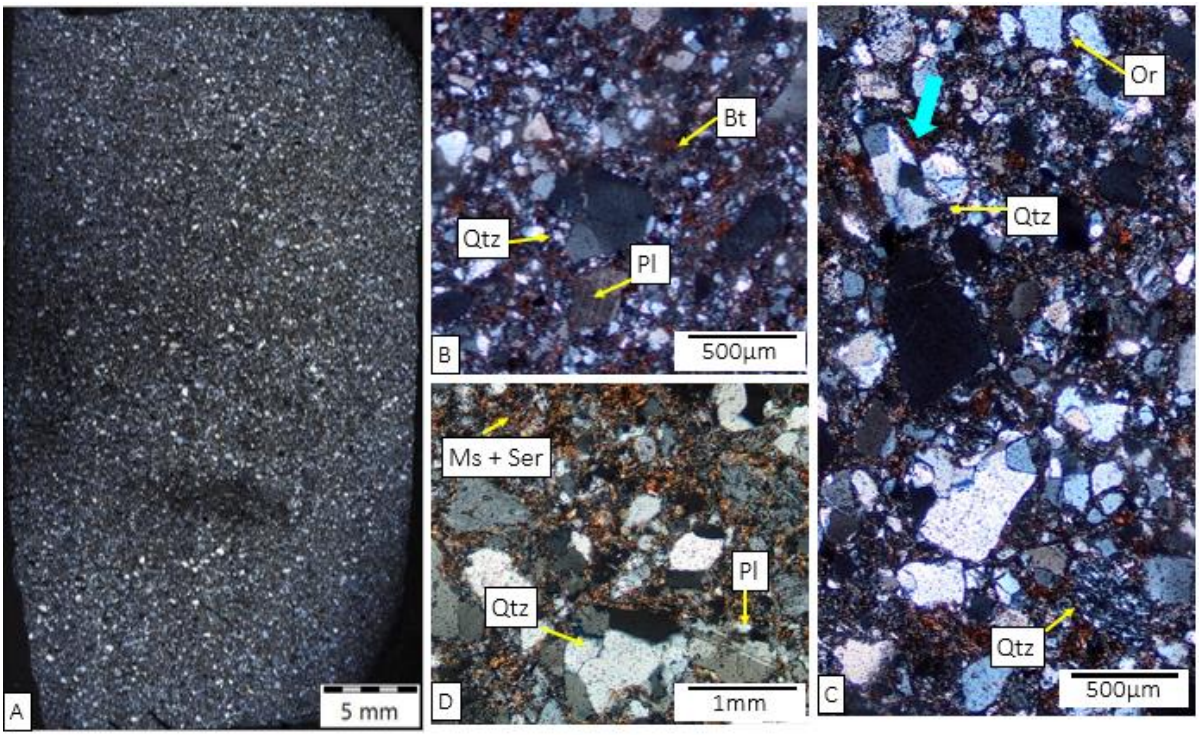

Figure 8.3: Petrographic mages of wacke. A) XPL image showing the fine-grained texture of the rock and the abundance of quartz grains with an extremely fine matrix. B) Microscopic image in XPL with magnification 4x showing fine grain quartz (Qtz), plagioclase (Pl), and biotite (Bt). C) Microscopic image in XPL with magnification 4x showing an abundance of quartz and polycrystalline quartz (in green), and biotite in the interstitial space. D) Microscopic image in XPL with magnification 10x, showing polycrystalline quartz (green arrow) and its extinction behaviour. It also shows clasts of quartz and plagioclase cemented by micaceous matrix (Ms= muscovite, and Ser= sericite).

8.3.3. TIMA analysis: mineral phases and element maps

TIMA phase maps (Figure 8.4A) results show that the rock comprises of a high quartz content with lower concentrations of albite, orthoclase, biotite, and plagioclase. The spatial relationships observed in the image indicate that fine-grained quartz and plagioclase are homogenously distributed, with equally dispersed albite and disseminated orthoclase. The close-view image (Figure 8.4B) reveals that quartz occurs as coarser grains compared to albite and plagioclase, which are still less than 1 mm in size. Albite appears as semi-rounded and semi-elongated crystals.

The elemental maps (Figure 8.4C-E) show enrichment in Si than K and Al. The highest Si concentrations are associated with quartz, while moderate concentrations are linked to orthoclase and albite, and lower concentrations are related to muscovite and biotite. High K concentrations show the presence of muscovite (Figure 8.4D). Al high concentrations are associated with orthoclase, albite, muscovite, and plagioclase (Figure 8.4E and Appendix 13).

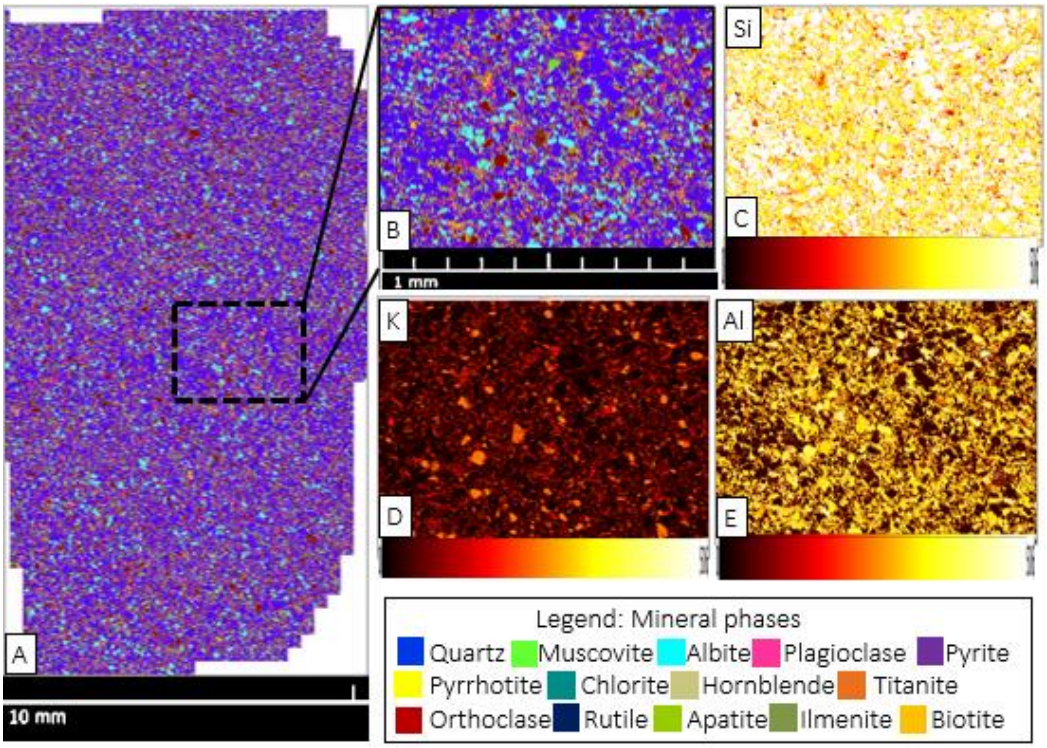

Figure 8.4: *TIMA images of wacke. A) Phase map showing equal dominance of plagioclase and quartz, dispersed albite, and disseminated orthoclase textures. B) Phase maps focusing on the demarcated area, showing coarse quartz with finer orthoclase, albite, and dispersed calcite, plagioclase, and biotite. C) An element map showing variations in Si concentrations, with the highest concentrations (in white) associated with quartz and the lowest concentrations with orthoclase, albite, biotite, and plagioclase. D) An element map showing low concentrations of K. E) An element map showing high (in yellow) Al concentrations, associated with orthoclase, albite, biotite, and plagioclase.*

8.3.4. Modal abundance

The modal abundances for the wacke sample were determined using TIMA and XRD analyses (Figure 8.5, Appendix 3 and 4). Both analyses show that the wacke has high quartz content with lower concentrations of plagioclase, orthoclase, and biotite. However, XRD (Figure 8.5A) detected twice the amount of plagioclase compared to TIMA. It is important to note that, TIMA (Figure 8.5B) detects 5% muscovite and accessory amounts of pumpellyite, ilmenite, chlorite, and hornblende, which is not detected by XRD. XRD, on the other hand, found no muscovite but detected accessory amounts of dolomite (Figure 8.5A).

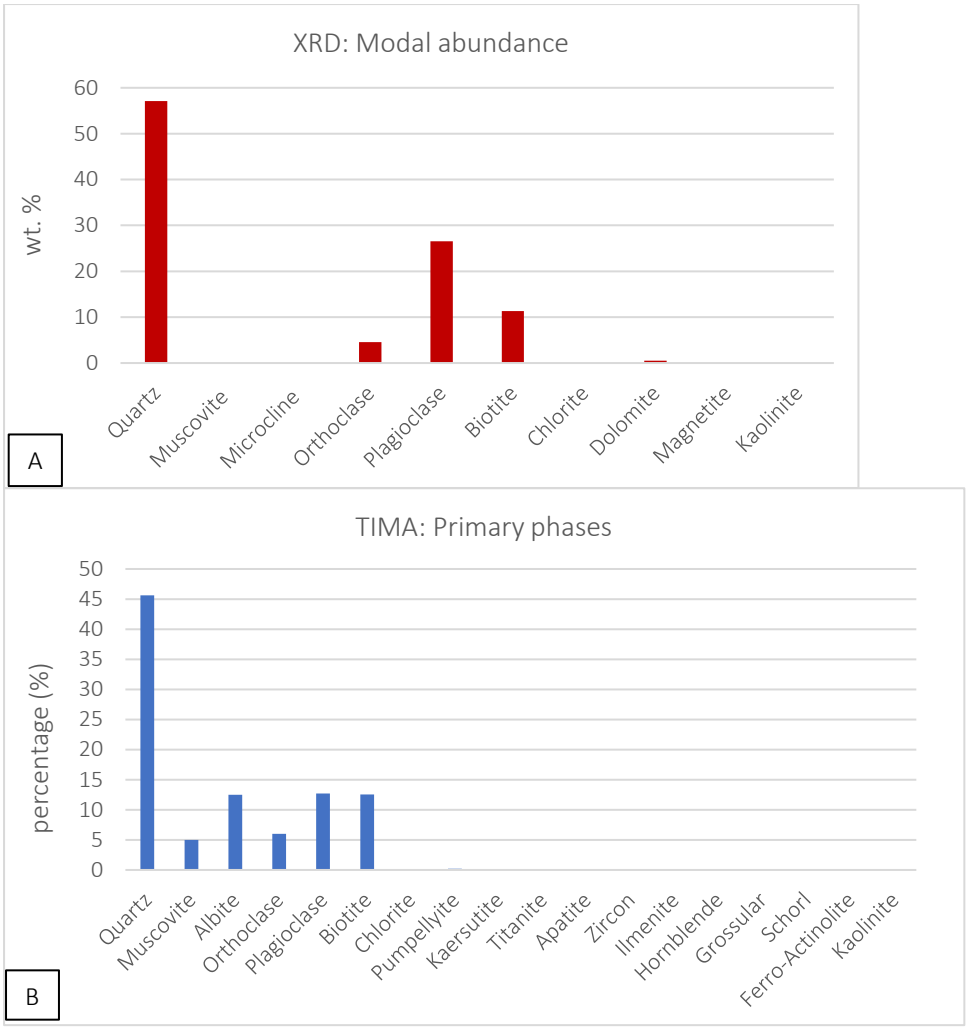

Figure 8.5: *Graphs showing the mineral abundance of the wacke sample. A) XRD results (in wt. %) show that quartz and plagioclase make up the bulk composition with less biotite. B) TIMA results (in %) show that quartz is the dominant primary phase, followed by plagioclase, biotite, and albite. The rock also contains accessory amounts of pumpellyite, ilmenite, chlorite, and hornblende.*

8.3.5. Accelerated Mortar Bar Test (SANS 6245)

The test results for the specimen were averaged as follows: after day one of curing, the average expansion was 0.01%. After seven days of curing, the average expansion increased to 0.04 %. By day fourteen of curing, the specimen showed an average expansion of 0.1% (Table 8.2). The graph in Figure 8.6 illustrates an increasing trend of expansion over fourteen days.

Table 8.2: Mean expansion percentages with days for wacke (PG)

Time	*Expansion %*
D1	0.01
D7	0.04
D14	0.10

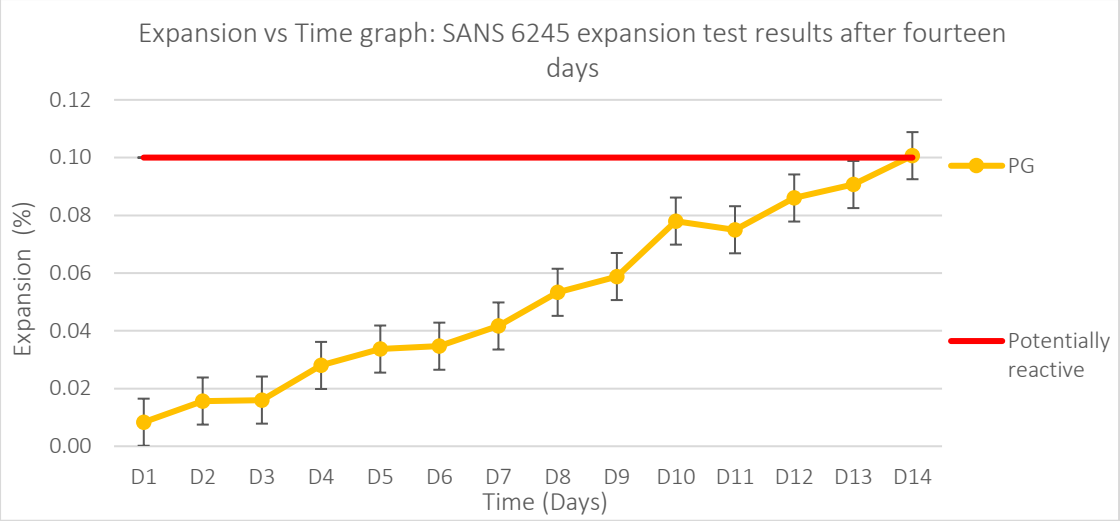

***Figure 8.6**: Image showing a graph for the expansion test results using wacke (PG) aggregate for SANS 6245 after fourteen days of immersion in NaOH solution.*

8.4. Discussions

8.4.1. Geological characteristics and classification of Malmesbury wacke

The Malmesbury Group wacke used in this research is characterised by angular to sub-angular grains of quartz, feldspar, and minor lithic fragments, cemented by a matrix abundant in microscopic biotite, sericite, cryptocrystalline, and microcrystalline quartz, as well as trace amounts of chlorite. The rock contains more than 25% feldspars (Figure 8.4 and Appendix 13) and is thus classified as a feldspathic wacke (Nicholas, 2009; Earle, 2015). Although wackes are typically sedimentary rocks (Nichols, 2009), this feldspathic wacke has an abundance of accessory ilmenite, pumpellyite, and chlorite, suggesting it was subjected to very low-grade metamorphism (Frost and Frost, 2019). Furthermore, the presence of concavo-convex to semi-sutured boundaries observed in the quartz crystals indicates that the rock experienced grain contact dissolution due to a minor increase in pressure upon burial (Frost and Frost, 2019). Therefore, the rock is classified as a feldspathic metawacke. The metawacke is dominated by polycrystalline quartz exhibiting intense undulose extinction, indicating significant distortion of the quartz crystalline structure (Blight and Alexander, 2011; Fernandes *et al.*, 2016; Leeman *et al.,* 2016; Tiecher *et al*, 2018). Additionally, the abundance of quartz and feldspar, indicates high silica and aluminium concentrations.

8.4.2. Expansion result of the Mamlmesbury feldspathic metawacke

The Accelerated Mortar Bar Test, SANS 6245, was carried out over fourteen days, during which three specimens of the Malmesbury feldspathic metawacke (of single composition) were immersed in a NaOH solution and closely monitored by recording the changes in strain daily. As the number of days of immersion increased, so did expansion, following an almost linear trend (Figure 8.6). Although average results were presented (Table 8.2 and Figure 8.6), all specimens behaved similarly, reaching a 0.1% expansion by day fourteen (Appendix 5). According to Oberholster and Davis (1986) (Table 2.8),

specimens with an expansion of more than 0.1% are classified as potentially deleterious. Therefore, the Malmesbury feldspathic metawacke aggregate is classified as potentially alkali reactive.

8.5. Closure

This chapter concentrated on the Malmesbury feldspathic metawacke sample from the Peninsula Quarry. This metasedimentary rock is a fine-grained, quartz, and feldspar-rich rock dominated by polycrystalline and microcrystalline quartz exhibiting intense undulose extinction. The feldspathic metawacke used for the AMBT (SANS 6245), showed expansive behaviour (with an expansion of 0.1%). The expansion results classify the Malmesbury feldspathic metawacke as a potentially alkali-reactive aggregate.

CHAPTER NINE

9. The Witwatersrand quartzite (Krugersdorp Formation)

9.1. Geological setting

The Witwatersrand (Wits) Supergroup is an Archaean intracratonic sedimentary sequence found at the center of South Africa's Kaapvaal Craton (Robb and Meyer, 1995; McCarthy, 2006; Tucker *et al*., 2016). This 2.9 Ga world-class gold repository basin was formed by a series of crustal plate motions from the north and west in a foreland basin environment (Robb and Meyer, 1995; McCarthy, 2006; Tucker *et al*., 2016). The sedimentary sequence was deposited gradually and is associated with inland coastlines (Robb and Meyer, 1995; McCarthy, 2006; Tucker *et al*., 2016). The Wits basin was metamorphosed and reshaped by three major events, 1) lateral crustal movement, 2) the Vredefort meteorite impact, and 3) the emplacement of the Bushveld Complex (Robb and Meyer, 1995; McCarthy, 2006; Tucker *et al.,* 2016). The sedimentary sequence is divided into the lower West Rand Group and upper Central Rand Group (McCarthy, 2006; Frimmel, 2019).

The Central Rand Group is an arenaceous sequence that includes quartz-pebble conglomerates, quartzites, quartzwackes, and minor shales (McCarthy, 2006; Frimmel, 2019). Deposition occurs mostly under alluvial-braid-plain and modest alluvial fan conditions (McCarthy, 2006; Frimmel, 2019). This group is suggested to be divided into two subdivisions: the lower Johannesburg Subgroup and the upper Turffontein Subgroup (McCarthy, 2006; Frimmel, 2019). The Turffontein Subgroup is the penultimate stage of sedimentation in the Wits Basin, with widespread upward coarsening produced by tectonics (McCarthy, 2006). The Subgroup is divided into the Mondeor Formation, Elsburg Formation, and Kimberly Formation (McCarthy, 2006; Frimmel, 2019). The Turffontein Subgroup overlies the Johannesburg Subgroup (McCarthy, 2006; Frimmel, 2019).

The lower Johannesburg Subgroup is quartzite-dominated and was deposited in a fluvial braid-plain environment. This Subgroup is distinguished by multiple cycles of degradation caused by the transgression or progradation of braid plains (McCarthy, 2006; Frimmel, 2019). It contains five formations, which are the result of multiple cycles, and these include the Main Formation, Randfontein Formation, Luipaardsvlei Formation, Blyvooruitzicht Formation, and Krugersdorp Formation (McCarthy, 2006). While the Krugersdorp Formation was being deposited, the eruption of lava from the Bird Member occurred (McCarthy, 2006). The volcanics of the Bird Member unit only developed over a portion of the basin from the West Rand to Evander (Table 9.1) (McCarthy, 2006; Frimmel, 2019). Toward the end of the Krugersdorp Formation period, a basin-wide transgression occurred, resulting in the deposition of Booysens Formation shales near the top of the Johannesburg Subgroup. Depositional

conditions varied throughout the basin, resulting in lithological differences (Table 9.1) (McCarthy, 2006; Frimmel, 2019). These variations gave rise to the eight areas of the Wits Supergroup: Welkom, South Rand, Carletonville, West Rand, Central Rand, East Rand, Evander, and Klerksdorp area (Table 9.1) (McCarthy, 2006; Frimmel, 2019).

***Table 9.1**: The stratigraphy of the Central Rand Subgroup and different areas with associated Formation (Fm) (the black areas indicate an absence of the Fm). The far right shows a simplified lithostratigraphy of the Klerksdorp area in the Johannesburg Subgroup of the Central Rand Group and shows the origin of the aggregate sample used in the study (adapted from McCarthy, 2006; Frimmel, 2019).*

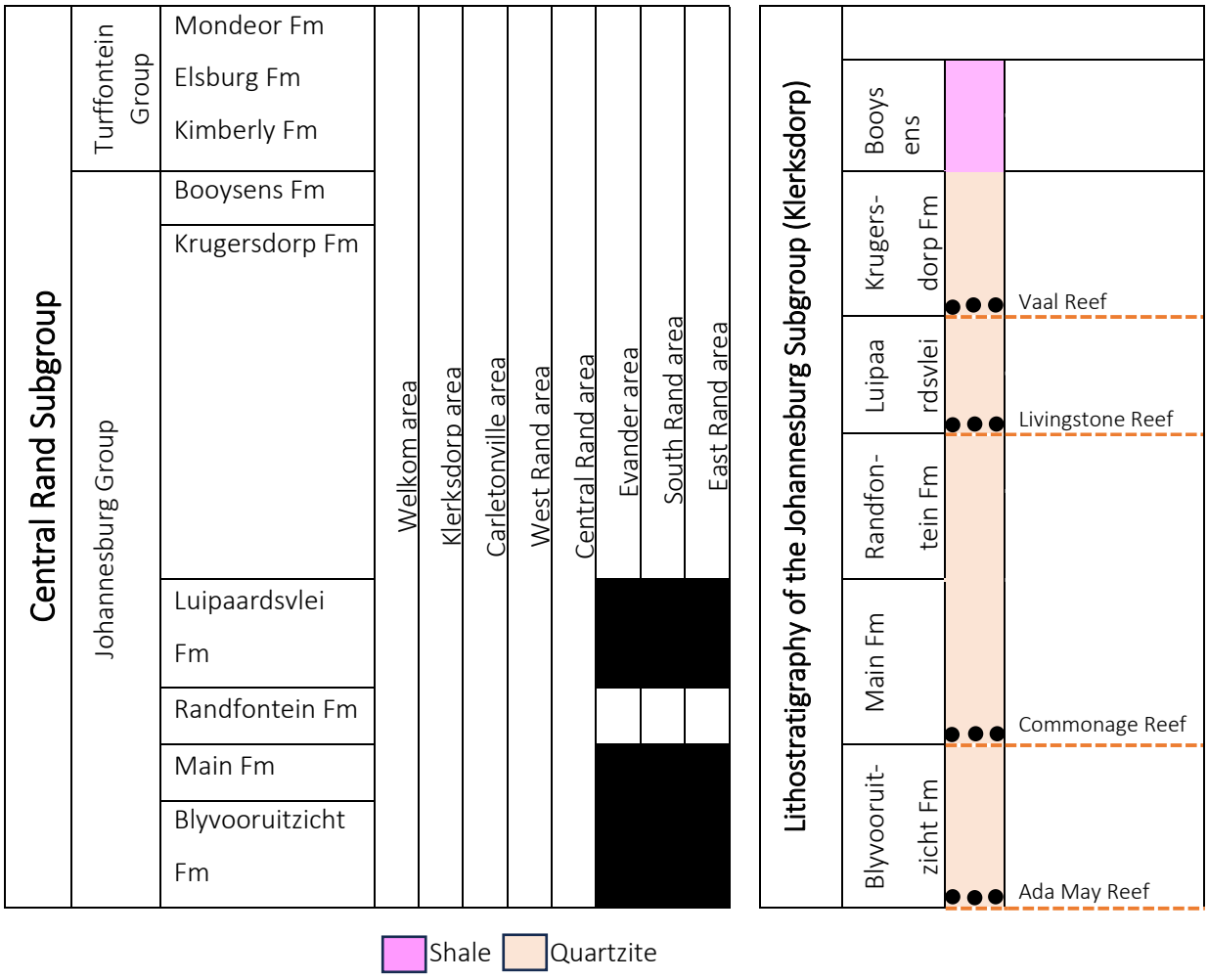

The Klerksdorp area, located southwest of Carletonville and separated by the Potchefstroom gap, is a highly fractured sub-basin characterised by erosional truncation of lower formations (McCarthy, 2006). It is made up of quartzites, conglomerates, shaly quartzites, siliceous quartzites, and argillaceous quartzites (McCarthy, 2006; Frimmel, 2019). The volcanic absent area is comprised of the basal Blyvooruitzicht Formation, upper Booysens Formation, Main Formation, Randfontein Formation Luipaardsvlei Formation, and Krugersdorp Formation (Table 9.1) (McCarthy, 2006; Frimmel, 2019). The Krugersdorp Formation is where the quartzite sample used in this research originates from.

9.2. Area of interest

The OMV Stilfontein Crushers, with coordinates 26˚46’46.72” S 26˚48’00.67” E (Figure 9.1A), is a surface crushing and screening operation (screening and crushing: rock dump, ballast, and crusher sand, stone, dust and run) situated outside of Stilfontein, along the N12 (OMV, 2023) (Figure 9.1B (i)). Stilfontein is a small town in the North West province of South Africa, known as a mining area, and it is approximately 23 km southwest of Potchefstroom and approximately 14 km east of Klerksdorp (Figure 9.1A).

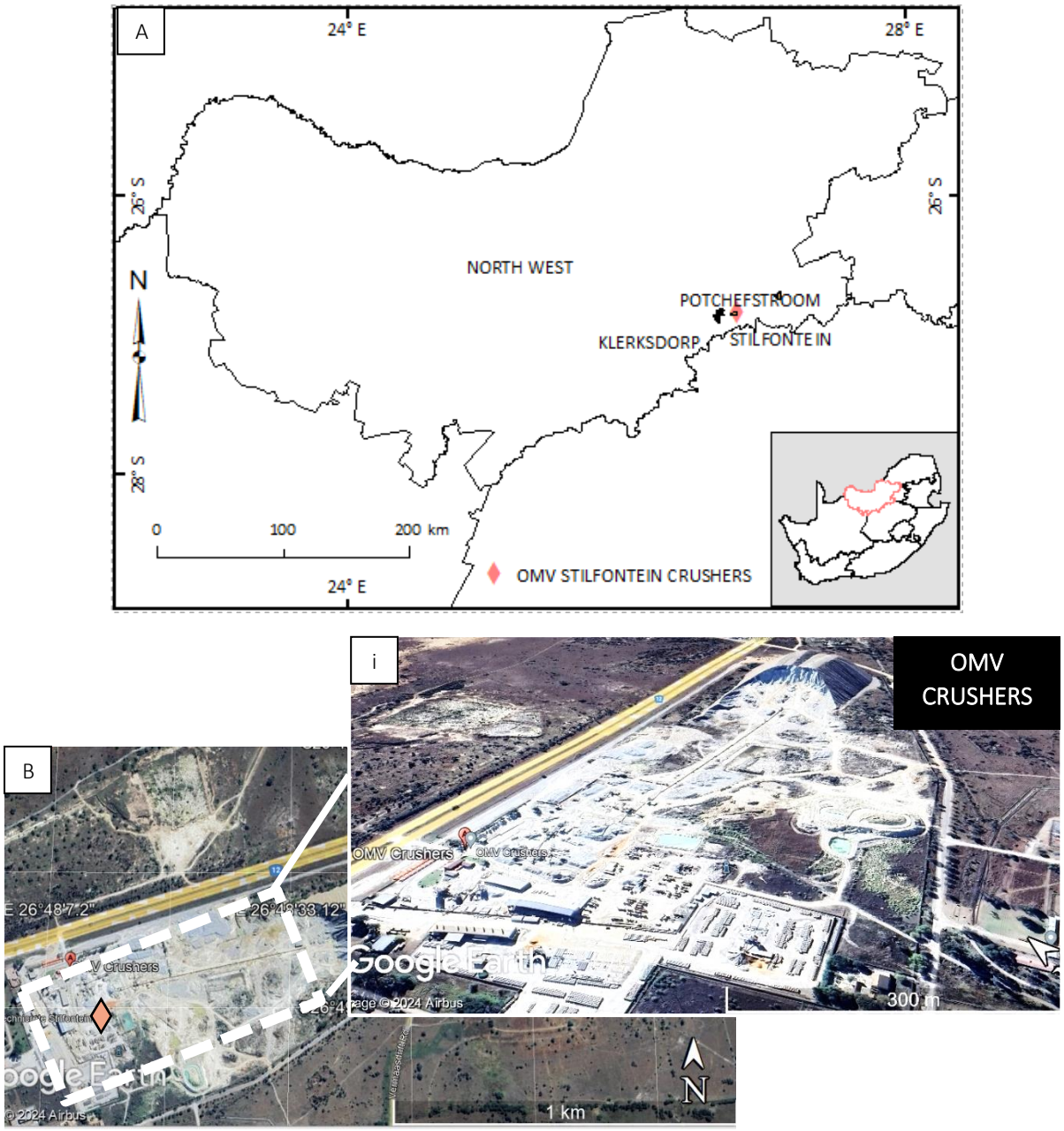

Figure 9.1*: Image showing area of interest. A) Map showing the study area for the OMV Stilfontein Crushers located in Stilfontein, and the surrounding cities with the North West Province. B) A Google Earth image showing the bird's eye view of the OMV Stilfontein Crushers. i) An enlarged image of the surface crushing and screening operation.*

9.3. Results

9.3.1. Macroscopic (hand specimen) observations

In hand specimen, the quartzite is a greenish-grey, non-foliated rock with interlocked, grainy glassy quartz grains (Figure 9.2A). There are no distinctive grain sizes, but annealing of quartz is observed (Figure 9.2A (i)). The rock is dominated by approximately 90% quartz and contains minor amounts of mica.

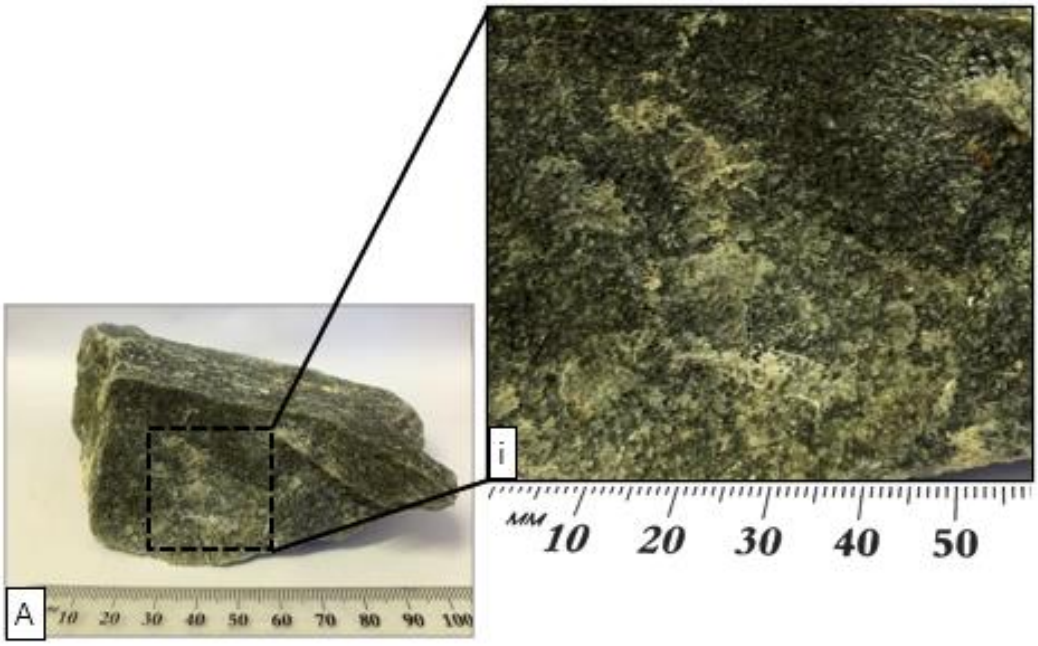

Figure 9.2: An image of the hand specimen of the quartzite. A) A greenish grey rock, dominantly composed of quartz. i) An enlarged area within the sample showing annealing of quartz.

9.3.2. Petrographic analysis

Petrographic analysis shows that the quartzite sample is fine- to medium-grained (0.5-2 mm) with no mineral alignment, containing approximately 85% quartz, minor muscovite, and accessory apatite (Figure 9.3A-D). The magnified petrographic images (Figure 9.3B-D) reveal that the rock is composed of quartz, and minor orthoclase, with apatite occurring as accessory crystals cemented by a fine-grained matrix consisting of extremely fine-grained mica and microcrystalline quartz. Granoblastic textures and sutured grain boundaries between quartz clasts are also observed. Coarser quartz crystals are angular to subangular, occurring as both monocrystalline and polycrystalline clasts. These exhibits intense undulatory extinction, subgraining, and recrystallisation along the grain boundaries (Figure 9.3D). There is also an abundance of large microcrystalline quartz clasts (Figure 9.3B-D) and strained polycrystalline quartz. Additionally, intragranular and intergranular microcracking is observed in the coarse quartz crystals, with some microcracks filled by minerals observed in the matrix.

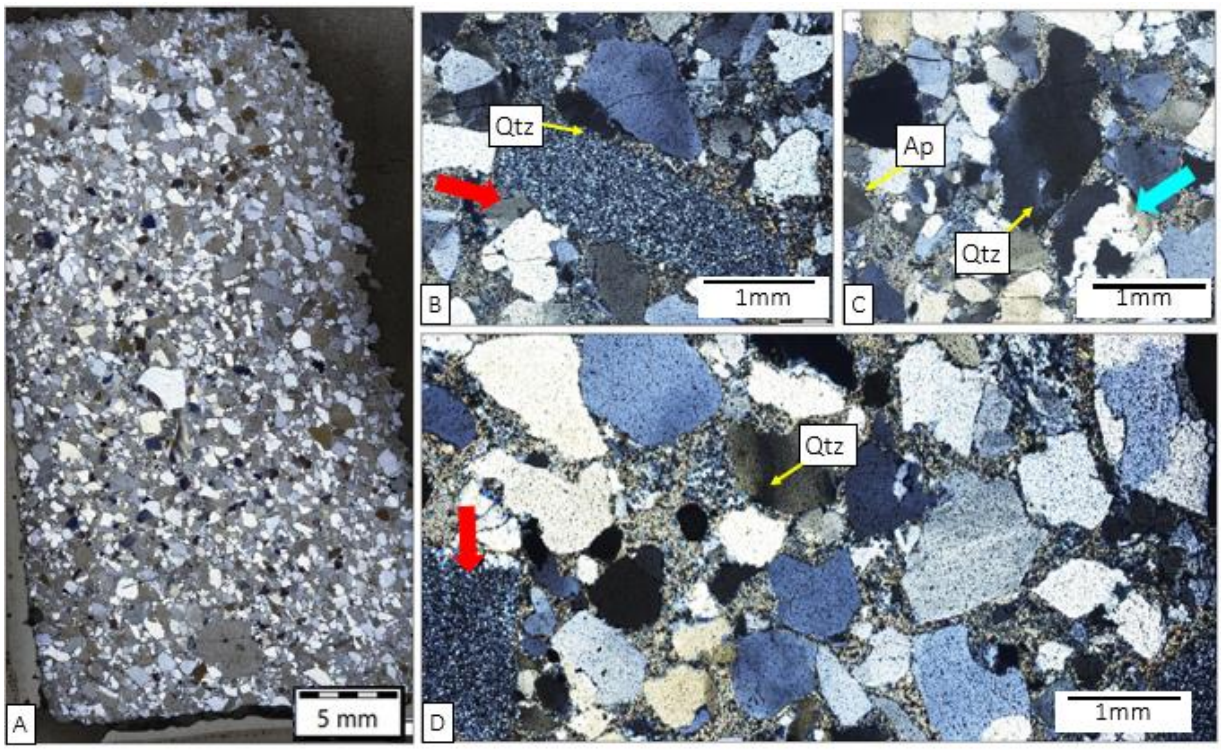

Figure 9.3: *Petrographic Images of quartzite. A) A microscopic XPL image showing fine- to medium-grained (0.5-2 mm) texture with no mineral alignment and an abundance of quartz. B) A microscopic image in XPL with magnification 4x, showing undulose extinction of quartz crystals and a medium-grained microcrystalline quartz crystal (red arrow). C) A microscopic image in XPL with magnification 4x, showing undulose extinction, strained polycrystalline quartz (blue arrow), microcrystalline quartz, and subgraining and recrystallisation along quartz boundary, and isotropic apatite (Qtz= quartz, and Ap= apatite). D) A microscopic image in XPL with magnification 4x, showing undulose extinction, strained polycrystalline quartz, and microcrystalline quartz (red arrow).*

9.3.3. TIMA analysis: phase maps and elemental maps

Phase maps (Figure 9.4A-B) show that the rock consists of quartz, with lesser amounts of muscovite, and minor pyrite and pyrrhotite. Quartz is homogeneously distributed, and muscovite is dispersed. Figure 9.4B further reveals that medium- to coarse-grained (more than 1 mm), subhedral quartz is interstitially filled by anhedral muscovite. Additionally, extremely fine quartz crystals are observed around the coarser quartz crystals.

The elemental maps (Figure 9.4C-E) reveal that Si occurs in higher concentrations than K and Al. The highest Si concentration is associated with quartz. K occurs in moderate concentrations associated with muscovite (Figure 9.4D). Al occurs in high concentrations and its concentration overlaps with the K concentration, suggesting domains of muscovite.

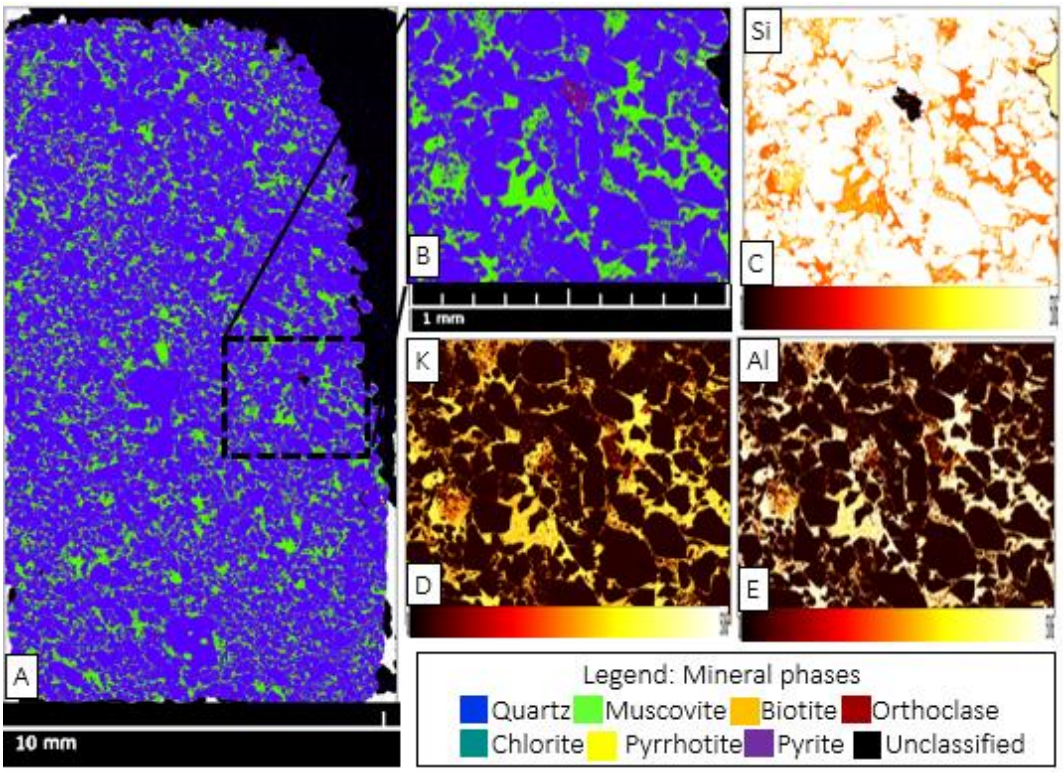

Figure 9.4: *TIMA Images of quartzite. A) A mineral phase map showing the dominance of quartz with dispersed muscovite. B) A mineral phase map focusing on the demarcated area showing medium- to coarse-grained (more than 1 mm), subhedral quartz interstitially filled by anhedral muscovite, and extremely fine quartz crystals surrounding coarser quartz. C) An element image showing variations in Si concentrations, with the highest concentrations associated with quartz and the lowest, with pyrite. D) An element image showing variations in K concentrations, with moderate concentrations associated with muscovite and the lowest with quartz. E) An element image showing variations in Al concentrations, with high concentrations associated with muscovite and the lowest with quartz.*

9.3.4. Modal abundance

The modal abundance for the quartzite was determined using TIMA and XRD analyses. Both analyses (Figure 9.5A-B, Appendix 3 and 4) reveal that the rock contains more than 66% quartz and less than 18% muscovite. TIMA (Figure 9.5B) also detected accessory amounts of biotite and chlorite, whereas XRD detected accessory magnetite.

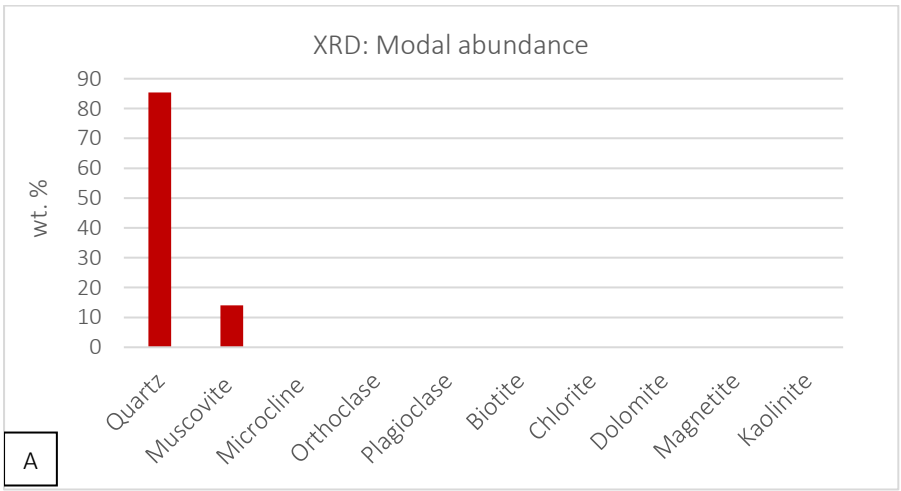

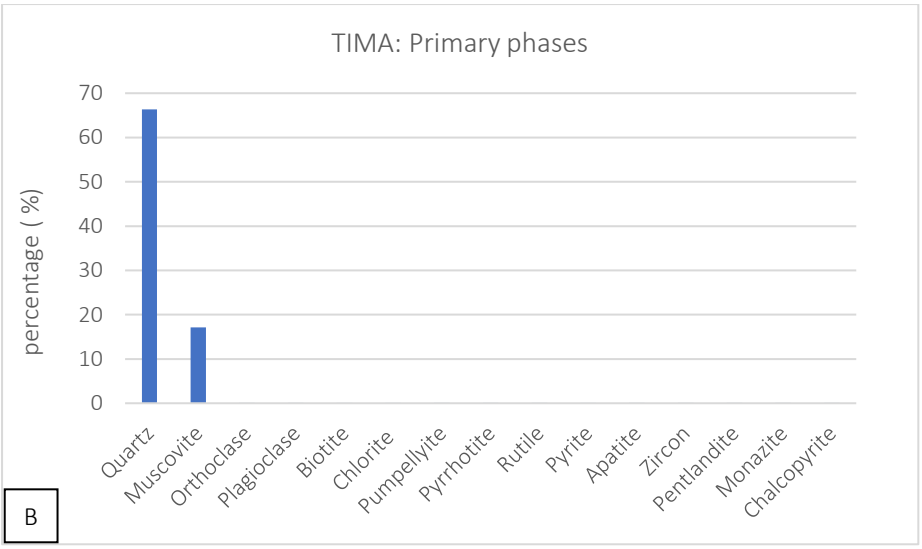

Figure 9.5: *Graphs showing the mineral abundance of quartzite. A) XRD results (in wt. %) show that rock is dominated by quartz and contains low muscovite concentrations. B) TIMA results (in %) show that quartz is the dominant primary phase followed by muscovite. The rock also contains accessory amounts of biotite, chlorite, and pyrite.*

9.3.5. Accelerated Mortar Bar Test (SANS 6245)

The test results for the specimen were averaged as follows: after day one of curing, the average expansion was 0.01%. After seven days of curing, the average expansion increased to 0.05%. By day fourteen of curing, the average expansion reached 0.1% (Table 9.2). The graph in Figure 9.6 shows an increasing trend of expansion over the fourteen days.

Table 9.2: *Mean expansion percentages with days for Krugersdorp quartzite (SQ).*

Time	*Expansion %*
D1	0.01
D7	0.05
D14	0.10

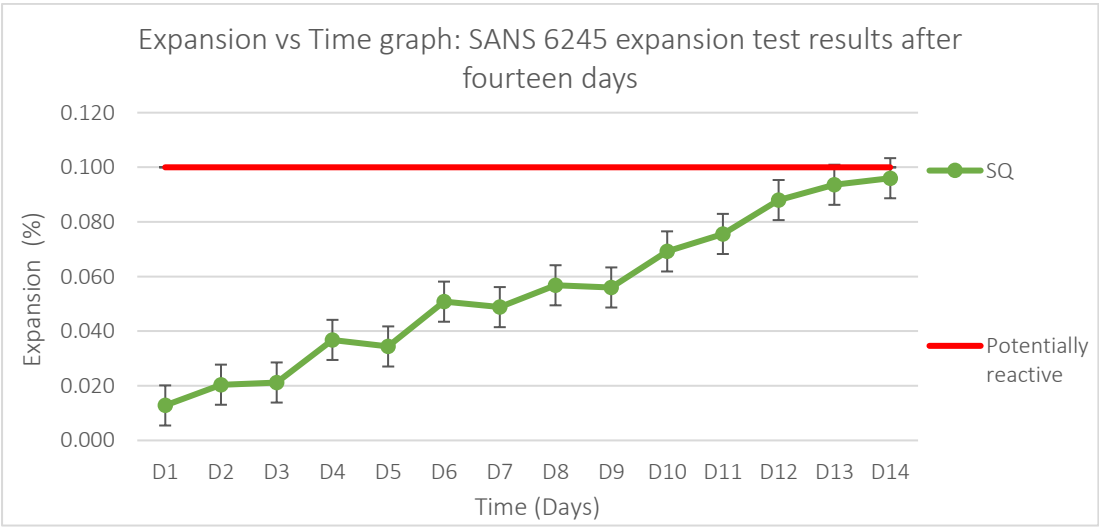

Figure 9.6*: Image showing a graph for the expansion test results using quartzite (SQ) aggregate for SANS 6245 after fourteen days of immersion in NaOH solution.*

9.4. Discussions

9.4.1. Geological characterisation and classification of the Witwatersrand quartzite (Krugersdorp Formation)

The Krugersdorp Formation quartzite rock utilised in this study is a monomineralic, medium-grained rock cemented by a micaceous matrix. It exhibits distinctive granoblastic textures, subgraining, and recrystallisation along quartz boundaries. Despite undergoing low-grade metamorphism (Heinrich, 1956; Best, 2003; Frost and Frost, 2019), the presence of sutured boundaries between quartz grains, intense undulatory extinction of polycrystalline quartz, and abundant microcracking suggests metamorphism was accompanied by deformation (MacKenzie *et al*., 2017; Frost and Frost, 2019). Furthermore, the quartzite is characterised by monocrystalline quartz with pronounced undulose extinction and an abundance of coarse-grained microcrystalline quartz, indicating significant distortion of the quartz crystalline structure (Blight and Alexander, 2011; Fernandes *et al*., 2016; Leeman *et al.,* 2016; Tiecher *et al*, 2018). Given that the rock is quartz-rich (Appendix 14) it has high silica content.

9.4.2. Expansion results for the Witwatersrand quartzite (Krugersdorp Formation)

An Accelerated Mortar Bar Test, SANS 6245, was conducted over fourteen days, during which three specimens, containing a single composition of the Krugersdorp Formation quartzite were immersed in a NaOH solution and closely monitored for changes in strain each day. Minor changes were observed initially, but an increase in strain occurred on day four. With increasing days of immersion, the expansion also increased (Figure 9.6). Despite presenting average results (Table 9.2 and Figure 9.6), all specimens exhibited similar behaviour, experiencing 0.1% expansion by day fourteen (Appendix 5). According to Oberholster and Davis (1986) (Table 2.8), specimens that experiencing expansion between 0.1-0.2% are classified under the innocuous and deleterious aggregates group. Therefore, the quartzite aggregate of the Krugersdorp Formation, in the Klerksdorp area, is identified as potentially alkali reactive.

9.5. Closure

This chapter looked at the Witwatersrand quartzite sampled from the OMV Crusher. The metamorphic rock is a medium-grained, quartz-rich rock, cemented by a micaceous matrix. It is characterised by monocrystalline and microcrystalline quartz with intense undulose extinction, as well as subgraining and recrystallisation along quartz boundary. In the medium- to coarse-grained quartz intragranular and intergranular microcracking is observed. The quartzite used for the AMBT (SANS 6245), showed expansive behaviour (with an expansion of 0.1%). The expansion results classify the Witwatersrand quartzite as a potentially alkali-reactive aggregate.

CHAPTER TEN

10. Discussion

10.1. Expansion test results versus geological characteristics

The primary aim of this study is to leverage the geological characteristics of each aggregate taken from different parts of South Africa to understand their expansion and ASR susceptibility. Geological analyses and expansion tests were conducted, and the results were compared. Each aggregate exhibited distinct expansion behaviours, as illustrated in Figure 10.1, which can be correlated with the microscopic attributes of each aggregate. The microscopic attributes for each aggregate are discussed below.

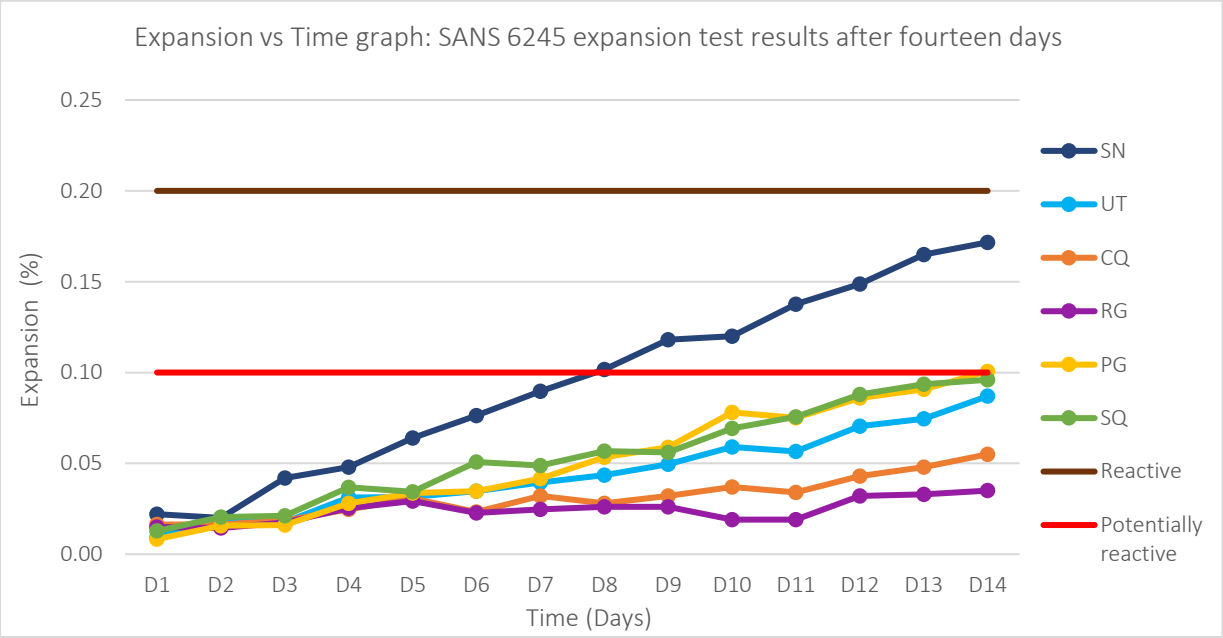

Figure 10.1*: A graph showing the expansion behaviour for all aggregates over fourteen days with an indicator value of innocuous and deleterious aggregate. SN = Witwatersrand micaceous metashale (Booysens Formation) and quartzite (Randfontein Formation); UT = Dwyka tillite; CQ = Natal arkosic sandstone; RG = CGS monzogranite; PG = Malmesbury feldspathic metawacke; SQ = Krugersdorp Formation quartzite.*

<u>The Witwatersrand micaceous metashale (Booysens Formation) and quartzite (Randfontein Formation) (SN)</u>

The Accelerated Mortar Bar Test results (Figure 10.1) reveals that the Booysens micaceous metashale and Randfontein quartzite are potentially alkali-silica reactive, exhibiting an expansion of 0.17% after fourteen days. This expansion can be correlated with the geological characteristics detailed below.

The Booysens micaceous metashale is a finely grained rock composed of more than 50% microcrystalline quartz, a known reactive mineral (Oberholster *et al*., 1978; Hobbs, 2002, Fernandes *et al*., 2016). The fine-grain nature increases the surface area of quartz, promoting collision between hydroxides, silica, and water, thus encouraging ASR (Key and Ball, 2014). Although dominated by muscovite, the significant silica concentrations facilitate the reaction, and muscovite's less resistant

nature, does not impede ASR and gel expansion (Neville and Brooks, 1987; Blight and Alexander, 2011; Kawai *et al*., 2015; Leeman *et al.,* 2016).

The Randfontein Formation quartzite is characterized by intense undulatory extinction, subgraining, and recrystallisation along its crystal boundaries, features that favour ASR (Fernandes *et al.,* 2016; Fanijo *et al*., 2021; Venyite *et al*., 2022). The rock's high silica content, along with microcrystalline and cryptocrystalline quartz, increases the surface area of quartz grains, promoting reactivity (Key and Ball, 2014). Additionally, intergranular and intragranular microcracking in medium-grained quartz crystals not only increases the surface area of quartz but also creates zones of weakness where ASR gel can migrate, thus encouraging expansion (Ghasemi *et al*., 2020).

The Dwyka tillite (UT)

The Dwyka tillite is classified as potentially reactive (Figure 10.1 and Appendix 5). This is because the rock contains microcrystalline and polycrystalline quartz with strong undulating extinction, attributes known to favour ASR (Fernandes *et al.,* 2016; Fanijo *et al*., 2021; Venyite *et al*., 2022). The fine-grained nature of quartz increases its surface area, and the high silica content facilitates reactivity (Key and Ball, 2014). Additionally, Intergranular and intragranular microcracking in non-reactive crystals, such as orthoclase and actinolite, provide potential pore spaces for ASR gel migration (Ghasemi *et al*., 2020).

The Natal arkosic sandstone (CQ)

The Natal arkosic sandstone aggregate is non-reactive, with less than 0.1% expansion after fourteen days (Figure 10.1). Due to the dominance of monocrystalline quartz with straight extinction, minimal microcracking, and medium-grained quartz with smooth boundaries, the sandstone has a reduced surface area, thus lowering the potential for ASR (Glinnemann *et al*., 1992; Klein, 2003; Blight and Alexander, 2011; Key and Ball, 2014; MacKenzie *et al*., 2017). Although high silica defines this rock, the type of silica is not disordered and thus does not dissolve in the presence of hydroxides and water (Blight and Alexander, 2011; Fernandes *et al*., 2016; Leeman *et al.,* 2016).

The CGS monzogranite (RG)

The CGS monzogranite is also classified as non-reactive because it contains pure, monocrystalline quartz with straight extinction and minor undulatory extinction. The medium-grained quartz, low silica concentration, and interlocking crystals without microcracking reduce the surface area and collision rate, preventing ASR (Neville and Brooks, 1987; Glinnemann *et al*., 1992; Klein, 2003; Blight and Alexander, 2011; Key and Ball, 2014; MacKenzie *et al*., 2017).

The Malmesbury feldspathic metawacke (PG)

The Malmesbury feldspathic metawacke is potentially reactive, with more than 0.1% expansion on day fourteen (Figure 10.1). It is characterised by microcrystalline quartz and strained monocrystalline and polycrystalline quart, minerals known to be alkali reactive (Fernandes *et al.,* 2016; Fanijo *et al*., 2021; Venyite *et al*., 2022). The fine-grained nature and high silica concentration promote ASR (Fernandes *et al.,* 2016; Fanijo *et al.,* 2021; Venyite *et al.,* 2022). Furthermore, the intergranular and intragranular microcracking in many reactive and non-reactive crystals, become zones of weakness which the alkali-silica gel uses as potential pore space for gel migration, consequently, promoting expansion (Ghasemi *et al*., 2020).

The Krugersdorp Formation quartzite (SQ) of the Witwatersrand

The Krugersdorp Formation quartzite is potentially alkali reactive with an expansion of more than 0.1% on day fourteen. This quartzite, like the Randfontein quartzite, contains quartz crystals with intense undulatory extinction, subgraining, and recrystallisation along crystal boundaries, indicating a highly distorted quartz crystalline structure (Glinnemann *et al*., 1992; Klein, 2003; MacKenzie *et al.*, 2017). The quartzite contains microcrystalline quartz and high silica concentration, promoting ASR (Glinnemann *et al*., 1992; Klein, 2003; Fernandes *et al*., 2016; Fanijo *et al*., 2021; Venyite *et al*., 2022). Additionally, intergranular and intragranular microcracking in medium-grained quartz crystals not only increases its surface area but also creates zones of weakness that the alkali-silica gel uses as potential pore space for gel migration, thus encouraging expansion (Ghasemi *et al*., 2020).

While undulatory extinction is a common and important indicator, it cannot be solely used as the main factor favouring ASR occurrence. Instead, the intensity of undulatory extinction, increased surface area of quartz, high concentration of reactive silica, and the presence of microcracking must be considered together as the diagnostic characteristics. Due to the fact that these attributes were present in all the potentially reactive aggregates (however they were more prevalent in some than others) (Table 10.1). For example, medium-grained Witwatersrand quartzite with microcracking exhibited more expansion than finer-grained tillite and metawacke, highlighting the significance of microcracking. Similarly, a higher concentration of reactive silica correlates with greater expansion, as seen in the Krugersdorp versus Randfontein quartzite. Microcracking is crucial for expansion, as illustrated by the extensive microcracking in Randfontein quartzite, which experienced the most expansion. This research reveals that petrographic studies of aggregates can provide insight into aggregate susceptibility to ASR.

Table 10.1: A tabulated summary of the aggregates' characteristics and diagnostic features

Aggregate		Rock type	SiO_2 content	Dominant texture of quartz	Undulatory extinction	Microscopic features	Expansion (%)	Potential ASR reactivity
Witwatersrand	quartzite[1]	Metamorphic	> 80%	Medium-grained	Intense	Subgraining, and recrystallisation along quartz boundaries intergranular and intragranular microcracking	0.17	yes
	metashale	Metamorphic	20-50 %	Extremely fine-grained	Too small to be observed	-		
Dwyka tillite		Sedimentary	20-50 %	Fine-grained	intense	Microcrystalline and polycrystalline quartz Minor intergranular and intragranular microcracking	> 0.1	Yes
Natal arkosic sandstone		Sedimentary	60-75 %	Medium-grained	None-weak	Monocrystalline quartz with smooth boundaries	0.06	No
CGS monzogranite		Igneous	30-35 %	Medium-grained	None-weak	Pure, monocrystalline quartz	0.04	No
Malmesbury metawacke		Meta-sedimentary	45-55 %	Fine-grained	Intense	Strained monocrystalline and polycrystalline quartz Minor intergranular and intragranular microcracking	> 0.1	Yes
Witwatersrand quartzite[2]		Metamorphic	60-80 %	Medium-grained	Intense	Subgraining, and recrystallisation along quartz boundaries intergranular and intragranular microcracking	0.1	Yes

1 = Randfontein Formation

2 = Krugersdorp Formation

10.2. Use of aggregates for construction projects

Extreme caution is necessary when selecting concrete aggregates to avoid using potentially deleterious rock. Understanding rock properties encourages the use of appropriate aggregates for concrete production (Oberholster *et al*., 1978; Neville and Brooks, 1987; Grieve, 2006). This research highlights the behaviour of aggregates in concrete, revealing that the Natal arkosic sandstone and Phase II CGS monzogranite, that show minimal alkali-silica reactivity, are suitable for construction. Conversely, the Booysens metashale, Randfontein and Krugersdorp quartzite, Malmesbury feldspathic metawacke, and Dwyka tillite that show potential alkali-silica reactivity, should be avoided. However, if the use of potentially alkali-reactive aggregates is unavoidable, mitigation strategies such as using supplementary cementitious material, less alkali-rich cement (due to the fact that the modal abundance in a potentially reactive aggregate cannot be chemically altered, however cement can) or a low water/cement ratio can be implemented (Neville and Brooks. 1987; Oberholster, 2009; Blight and Alexander, 2011; Rajabipour *et al*., 2015; Ley, 2019).

11. Conclusion

This research aimed to employ geological techniques to understand the alkali-silica-reaction (ASR) susceptibility of reported concrete aggregates used in South Africa from various quarries. Geological analyses and the Accelerated Mortar Bar Test (SANS 6245) were conducted. The expansion results were compared to the microscopic properties observed in the aggregates to explain the expansion behaviour. Seven aggregates were assessed, each exhibiting distinctive microscopic attributes based on their rock type and origin. However, similar ASR favouring properties were observed. The Booysens metashale and Randfontein quartzite aggregates were potentially alkali reactive with expansion of over 0.1% on day fourteen due to their high content of microcrystalline and cryptocrystalline quartz and significant microcracking. The Dwyka tillite also showed potential reactivity due to its microcrystalline quartz and microcracking. The Natal arkosic sandstone and CGS monzogranite were non-reactive, with expansions less than 0.1%, attributed to their unstrained silica, medium-grained quartz, and minimal microcracking. The Malmesbury feldspathic metawacke and Krugersdorp Formation quartzite were potentially reactive, showing significant expansions due to their high reactive silica concentration and microcracking.

Undulatory extinction alone cannot be the sole indicator of ASR occurrence; the intensity of undulatory extinction, increased quartz surface area, high reactive silica concentration, and presence of microcracking must all be considered. The integration of these attributes is essential for understanding the ASR susceptibility of aggregates. Selecting appropriate aggregates for construction projects is

crucial to avoid ASR. However, if potentially reactive rocks must be used, mitigation strategies can be incorporated to reduce the risk. Petrographic studies of aggregates can provide insight into aggregate susceptibility to ASR; however, the integration of geological techniques is essential for a comprehensive understanding of aggregate properties and their susceptibility to ASR. Therefore, future studies should consider, combining the different methods for an accurate prognosis.

12. Recommendations

This dissertation identified some recommendations that may be conducted for future research, and these are:

- Although this study added to the knowledge of the susceptibility of South African concrete aggregates to ASR, literature regarding a geological approach of South African concrete aggregates' susceptibility to ASR is quite limited. Therefore, more studies of this kind, with different South African aggregates and semi-quantifying the findings, should be considered.
- Although literature regarding the chemical analysis of cement types is accessible, studies of this kind should consider doing a chemical analysis for the cement type used.
- Given that aggregates can be sourced from open pit quarrying or mine waste dumps, a study could be conducted to compare the similarities and differences of the aggregates' characteristics and expansion behaviours.
- XRD and TIMA are both used to determine modal abundance however, there were large discrepancies between the two results, in this research. Therefore, an investigation of the comparison of these two analytical methods is recommended

13. References

AfriSam., 2021. AfriSam Aggregate. Available: https://www.afrisam.co.za/product/aggregate/concrete-aggregate/

Akinyemi, S.A., Gitari, W.M., Akinlua, A. and Petrik, L.F., 2012. Mineralogy and geochemistry of sub-bituminous coal and its combustion products from Mpumalanga Province, South Africa. *Analytical chemistry*, pp.47-70.

Alexander, M. and Blight, G., 2017. Southern and Central Africa. In *Alkali-Aggregate Reaction in Concrete: A World Review*, CRC Press, pp.509-538.

Alexander, M.G., 2019. *Alkali-aggregate reaction*. Mindess, S. (eds). Developments in the Formulation and Reinforcement of Concrete, Woodhead Publishing, pp.87.

Arito, P.A., Johannes, P.T. and Mulundu, M.T., 2023. The susceptibility of selected Namibian aggregates to ASR. *Concrete Beton*, 172, pp.10-14.

Bailie, R. and Weber, B., 2024. Petrogenesis and tectonic implications of the Bloubergstrand basaltic andesites, Tygerberg Formation, Malmesbury Group, Pan-African Saldania Belt, southwestern Africa. *South African Journal of Geology*, *127*(1), pp.95-116.

Belcher, R.W. and Kisters, A.F., 2003. Lithostratigraphic correlations in the western branch of the Pan-African Saldania belt, South Africa: the Malmesbury Group revisited. *South African Journal of Geology*, 106(4), pp.327-342.

Bell, F.G. and Lindsay, P., 1999. The petrographic and geomechanical properties of some sandstones from the Newspaper Member of the Natal Group near Durban, South Africa. *Engineering Geology*, *53*(1), pp.57-81.

Ben Haha, M., 2006. *Mechanical effects of alkali silica reaction in concrete studied by SEM-image analysis*. Doctoral dissertation, University of Science and Engineering Techniques, Switzerland.

Best, M.G., 2003. *Igneous and metamorphic petrology*. Blackwell, United Kingdom.

Beushausen, H. and Alexander, M., 2009. Concrete Repair. In: Owen, G. (eds). *Fulton's concrete technology,* 9th edition, Cement & Concrete Institute, South Africa, pp.393-409.

Blight, G.E. and Alexander, M.G., 2011. *Alkali-aggregate reaction and structural damage to concrete: engineering assessment, repair, and management*. CRC Press.

Britannica, T. Editors of Encyclopaedia, 2023. *Pietermaritzburg*. Available: https://www.britannica.com/place/Pietermaritzburg

Brouwer, P., 2006. Theory of XRF. *Almelo, Netherlands: PANalytical BV*.

Buggisch, W., Kleinschmidt, G. and Krumm, S., 2010. Sedimentology, geochemistry, and tectonic setting of the Neoproterozoic Malmesbury Group (Tygerberg Terrane) and its relation to neighbouring terranes, Saldania Fold Belt, South Africa. *Neues Jahrbuch für Geologie und Paläontologie-Abhandlungen*, pp.85-114.

Bunt, J.R., Waanders, F.B. and Schobert, H., 2012. Behaviour of selected major elements during fixed-bed gasification of South African bituminous coal. *Journal of Analytical and Applied Pyrolysis*, 93, pp.85-94.

Bussio, J.P., 2012. *Effect of dolerite intrusions on coal quality in the Secunda coal fields of South Africa*. Doctoral dissertation, University of Pretoria. Available: https://repository.up.ac.za/handle/2263/29300za

Cheng, Y.H., Zhu, B.L., Yang, S.H. and Tong, B.Q., 2021. Design of concrete mix proportion based on particle packing voidage and test research on compressive strength and elastic modulus of concrete. *Materials*, 14(3), pp.623.

Cole, W.F. and Lancucki, C., 1983. Products formed in an aged concrete the occurrence of okenite. *Cement and Concrete Research*, 13(5), pp.611-618.

Creamer, M., 2018. *Western Cape Quarry.* Mining Weekly. Available: https://www.miningweekly.com/article/western-cape-quarry-2018-05-04

Crow, J.M., 2008. The concrete conundrum. *Chemistry World*, 5(3), pp.62-66.

De Ceukelaire, L., 1991. The determination of the most common crystalline alkali-silica reaction product. *Materials and Structures*, 24, pp.169-171.

De Grazia, M.T., Goshayeshi, N., Gorga, R., Sanchez, L.F.M., Santos, A.C. and Souza, D.J., 2021. Comprehensive semi-empirical approach to describe alkali aggregate reaction (AAR) induced expansion in the laboratory. *Journal of Building Engineering*, 40, pp.1-13.

Dietrich, P. and Hofmann, A., 2019. Ice-margin fluctuation sequences and grounding zone wedges: The record of the Late Palaeozoic Ice Age in the eastern Karoo Basin (Dwyka Group, South Africa). *The Depositional Record*, *5*(2), pp.247-271.

Earle, S., 2015. *Physical geology*. BCcampus. Available: https://opentextbc.ca/geology/part/chapter-3-intrusive-igneous-rocks/.

Fanijo, E.O., Kolawole, J.T. and Almakrab, A., 2021. Alkali-silica reaction (ASR) in concrete structures: Mechanisms, effects and evaluation test methods adopted in the United States. *Case Studies in Construction Materials*, 15, pp.1-17.

Fernandes, I., Andiç-Çakır, Ö. and Hooton, D., 2016. Assessing aggregates for alkali–aggregate reaction potential. *Construction Materials*, 169, pp.172-178.

Fernandes, I., dos Anjos Ribeiro, M., Broekmans, M.A. and Sims, I. (eds) 2016. *Petrographic atlas: characterisation of aggregates regarding potential reactivity to alkalis: RILEM TC 219-ACS recommended guidance AAR-1.2, for use with the RILEM AAR-1.1 petrographic examination method* (Vol. 20). Springer.

Frimmel, H.E., 2019. The Witwatersrand Basin and its gold deposits. In: Kröner A, Hofmann A (eds) *The archaean geology of the Kaapvaal Craton. Southern Africa*. Springer. pp.255-279.

Frost, B.R. and Frost, C.D., 2019. Essentials *of igneous and metamorphic petrology*. Cambridge University Press.

Gagg, C.R., 2014. Cement and concrete as an engineering material: An historic appraisal and case study analysis. *Engineering Failure Analysis*, 40, pp.114-140.

Geng, G., Shi, Z., Lothenbach, B., Leeman, A., Wieland, E. and Dähn, R., 2021. A micro-XAS and XRD study of the crystalline alkali-silica reaction products. In: Batista, A.L., Silva, A.B., Fernandes, I.,

Santos, L.O., Custódio, J. and Serra, C. (eds). *Proceedings of the 16th International Conference on Alkali-Aggregate Reaction in Concrete.* Volume I, LNEC, Brasil, pp.15-22.

Ghasemi, S., Khamehchiyan, M., Taheri, A., Nikudel, M.R. and Zalooli, A., 2020. Crack evolution in damage stress thresholds in different minerals of granite rock. *Rock Mechanics and Rock Engineering*, 53, pp.1163-1178.

Gholizadeh-Vayghan, A. and Rajabipour, F., 2021. Physicochemical properties of synthetic alkali-silica reaction (ASR) gels. In: Batista, A.L., Silva, A.B., Fernandes, I., Santos, L.O., Custódio, J. and Serra, C. (eds). *Proceedings of the 16th International Conference on Alkali-Aggregate Reaction in Concrete.* Volume I, LNEC, Brasil, pp.267-279.

Gillott, J.E., 1995. Review of expansive alkali-aggregate reactions in concrete. *Journal of materials in civil engineering*, 7(4), pp.278-282.

Grieve, G., 2009. Aggregate for concrete. In: Owen, G. (eds). *Fulton's concrete technology*, 9th edition, Cement & Concrete Institute, South Africa, pp.25-54.

Gu, X., Jin, X. and Zhou, Y., 2016. *Basic principles of concrete structures*. Springer Berlin Heidelberg.

Harris, C., Faure, K., Diamond, R.E. and Scheepers, R., 1997. Oxygen and hydrogen isotope geochemistry of S-and I-type granitoids: the Cape Granite suite, South Africa. *Chemical Geology*, 143(1-2), pp.95-114.

Heinrich, E.W., 1956. *Microscopic petrography.* The Maple Press Company, York. Pa.

Hicks, N., 2010. Extended distribution of Natal Group within southern KwaZulu-Natal, South Africa: implications for sediment sources and basin structure. *South African Journal of Geology*, *113*(3), pp.287-306.

Hobbs, D.W., 2002. Alkali-silica reaction in concrete. In: Bensted, J. and Barnes, P. (eds). *Structure and performance of cements*, 2nd edition, Spon Press, London, pp.265-281.

Hrstka, T., Gottlieb, P., Skala, R., Breiter, K. and Motl, D., 2018. Automated mineralogy and petrology-applications of TESCAN Integrated Mineral Analyzer (TIMA). *Journal of Geosciences*, 63(1), pp.47-63.

Hustrulid, W.A., 2023. *Quarry*. Available: https://www.britannica.com/technology/quarry-mining

Ideker, J.H., East, B.L., Folliard, K.J., Thomas, M.D. and Fournier, B., 2010. The current state of the accelerated concrete prism test. *Cement and concrete research*, 40(4), pp.550-555.

Johnsonn, M.R., van Vuuren, C.J., Visser, J.N., Cole, D.I., Wickens, H., Christie, A.D., Roberts, D.L and Brandl, G., 2006. Sedimentary rocks of the Karoo Supergroup. In: Johnson, M.R., Annhacusser, C.R. and Thomas, R.J. (eds). *The Geology of South Africa*. Geological Society of South Africa. Johannesburg/Council for Geoscience. Pretoria, pp.461-500.

Jones, B.R., Hingston, E.D.C. and Naidoo, K., 2011. Evaluation of the stability of a rehabilitated pit wall slope at Coedmore Quarry, Durban, South Africa. *Proceedings of Young Geotechnical Engineers Conference*, 31, pp.1-10

Jordaan, L.J., Scheepers, R. and Barton, E.S., 1995. The geochemistry and isotopic composition of the mafic and intermediate igneous components of the Cape Granite Suite, South Africa. *Journal of African Earth Sciences*, 21(1), pp.59-70.

Kao, P., 2016. A study of reactive silica dissolution for determining potential alkali silica reactivity in concrete. Masters dissertation, University of Washington. Available: https://digital.lib.washington.edu/researchworks/handle/1773/44986

Kawai, K., Sakuma, H., Katayama, I. and Tamura, K., 2015. Frictional characteristics of single and polycrystalline muscovite and influence of fluid chemistry. *Journal of Geophysical Research: Solid Earth*, 120(9), pp.6209-6218.

Kawamura, M. and Iwahori, K., 2004. ASR gel composition and expansive pressure in mortars under restraint. *Cement & Concrete Composition*, 26, pp.47-56.

Key, J.A. and Ball, D.W., 2014. *Introductory Chemistry I,* 1st edition*,* BC Campus.

Kisters, A. and Belcher, R., 2018. The Stratigraphy and structure of the western Saldania Belt, South Africa and geodynamic implications. *Geology of Southwest Gondwana*, pp.387-410.

Klein, C. (ed) 2003. *The 22nd Edition of the Manual of Mineral Science*. John Wiley & Sons, Inc., New York.

Kleinhans, M., 2016. Mining every last bit: commodity: gold & PGMs. *Inside Mining*, 9(7), pp.14-15.

Kurtis, K.E., Xi, Y., Glinicki, M.A., Provis, J., Giannini, E.R. and Fu, T., 2017. Can we design concrete to survive nuclear environments. *Concrete. International*, 39(11), pp.53-59.

Lanza, V. and Alaejos, P., 2012. Optimized Gel Pat Test for Detection of Alkali-Reactive Aggregates. *ACI Materials Journal*, 109(4). pp.1-13

Law, R.D., 1986. Relationships between strain and quartz crystallographic fabrics in the Roche Maurice quartzites of Plougastel, western Brittany. *Journal of Structural Geology*, 8(5), pp.493-515.

Le Bas, M.J. and Streckeisen, A.L., 1991. The IUGS systematics of igneous rocks. *Journal of the Geological Society*, 148(5), pp.825-833.

Leemann, A., Katayama, T., Fernandes, I. and Broekmans, M.A. (2016) Types of alkali–aggregate reactions and the products formed. *Proceedings of the Institution of Civil Engineers-Construction Materials*, 169(3), pp.128-135.

Ley T., 2018. *How to make cement*. Available: https://www.youtube.com/watch?v=MNK-z-35LG0

Ley, T., 2018. *Types of Cement*. Available: https://www.youtube.com/watch?v=cApoqFALh8s&t=56s

Ley, T., 2019. *How do you stop ASR? | A design guide for alkali silica reaction for concrete*. Available: https://www.youtube.com/watch?v=Qu2wM7_FPg8&t=14s

Ley, T., 2019. *The silent killer of concrete! | Intro to Alkali Aggregate Reaction*. Available: https://www.youtube.com/watch?v=qiF89HFLY2A&t=61s

Liaudat, J., 2018. *Experimental and numerical study of the effect of stress on ASR expansions in concrete.* Doctoral dissertation, University of Barcelona. Available: https://upcommons.upc.edu/handle/2117/121005

Liu, K.W. and Cooper, M.R., 1998. Tidalites in the Natal Group. *South African Journal of Geology*, *101*(4), pp.307-312.

MacKenzie, W.S., Adams, A.E. and Brodie, K.H., 2017. *Rocks and minerals in thin section: A colour atlas*. CRC Press.

Mahomed, Z.L., 2018. *Alkali-Aggregate reaction in Western Cape concrete*. MSc thesis, University of Cape Town.

Marshall, C.G.A. and von Brunn, V., 1999. The stratigraphy and origin of the Natal Group. *South African Journal of Geology*, 102(1), pp.15-25.

McCarthy, T.S., 2006. The Witwatersrand Supergroup. In: Johnson, M.R., Annhacusser, C.R. and Thomas, R.J. (eds). *The Geology of South Africa*. Geological Society of South Africa. Johannesburg/Council for Geoscience. Pretoria, pp.155-186.

Mhlanga, M., 2021. *Magmatic-petrogenetic & structural relationships of the peninsula granite of the Cape Granite Suite (CGS) with the Malmesbury group, sea point contact, Saldania belt, South Africa*. Masters dissertation, University of the Western Cape.

Milanesi, C.A., Locati, F. and Marfil, S., 2021. Questions and answers about alkali-carbonate reaction seen through the lens of osmotic mechanism. In: Batista, A.L., Silva, A.B., Fernandes, I., Santos, L.O., Custódio, J. ad Serra, C. (eds). *Proceedings of the 16th International Conference on Alkali-Aggregate Reaction in Concrete.* Volume I, LNEC, Brasil, pp.3-14.

Modie, B.N. and Le Hérissé, A., 2009. Late Palaeozoic palynomorph assemblages from the Karoo Supergroup and their potential for biostratigraphic correlation, Kalahari Karoo Basin, Botswana. *Bulletin of Geosciences*, 84(2), pp.337-358.

Mohammed, A. and Abdullah, A., 2018. Scanning electron microscopy (SEM): A review. In *Proceedings of the 2018 International Conference on Hydraulics and Pneumatics—HERVEX, Băile Govora, Romania*, pp.7-9.

Munir, M.J., Abbas, S., Qazi, A.U., Nehdi, M.L. and Kazmi, S.M.S., 2018. Role of test method in detection of alkali–silica reactivity of concrete aggregates. *Proceedings of the Institution of Civil Engineers-Construction Materials*, 171(5), pp.203-221.

Naidoo, D., 2008. Overview of South African Sand and Aggregate Industry. *Directorate: Mineral Economics*, R55, pp.1-10.

Neville, A.M. and Brooks, J.J., 1987. *Concrete technology*, 2nd edition. England: Longman Scientific & Technical.

Nichols, G., 2009. *Sedimentology and stratigraphy*. John Wiley & Sons, United Kingdom.

O'Brien, N.R., 1996. Shale lamination and sedimentary processes. *Geological Society, London, Special Publications*, 116(1), pp.23-36.

Oberholster, B., 2009. Alkali-silica reaction. In: Owen, G. (eds). *Fulton's concrete technology*, 9th edition, Cement & Concrete Institute, South Africa, pp.189-214.

Oberholster, R.E., 1996. Case studies of the practical and economical impact of alkali-silica reaction in South Africa. In *Proceedings of the 10th International Conference on Alkali-Aggregate Reaction (ICAAR), Melbourne, Australia*, pp.123-132.

Oberholster, R.E., Brandt, M.P. and Weston, A.C., 1978. Cement-aggregate reaction and the deterioration of concrete structures in the Cape Peninsula. *Civil Engineering= Siviele Ingenieurswese*, 7, pp.161-166.

Oberholster, R.E. and Davies, G., 1986. An accelerated method for testing the potential alkali reactivity of siliceous aggregates. *Cement and Concrete research*, 16(2), pp.181-189.

OMV., 2023. *Stilfontein*. Available: https://omv.co.za/sites/stilfontein/

Owens, G. (ed) 2013. *Fundamentals of concrete*. Cement and Concrete Institute, Midrand, South Africa.

Pandey, A., 2020. *Microscopy: Overview, Principles and its Types.* Available: https://microbiologynotes.org/microscopy-overview-principles-and-its-types/

Park, S., Lee, N. and Park, K.G., 2024. Early-age hydration behavior of calcium sulfoaluminate (CSA) cement/ordinary Portland cement-blended ultra-high performance concrete. *Journal of Building Engineering*, *87*, pp.109058.

Powell, C.M., 1979. A morphological classification of rock cleavage. *Tectonophysics*, 58(1-2), pp.21-34.

Prasad., 2023. *Deterioration of Concrete | Type and Causes*. Available: https://www.structuralguide.com/deterioration-of-concrete/

Rajabipour, F., Giannini, E., Dunant, C., Ideker, J.H. and Thomas, M.D., 2015. Alkali–silica reaction: Current understanding of the reaction mechanisms and the knowledge gaps. *Cement and Concrete Research*, 76, pp.130-146.

Robb, L.J. and Meyer, F.M., 1995. The Witwatersrand Basin, South Africa: geological framework and mineralization processes. *Ore Geology Reviews*, 10(2), pp.67-94.

Rozendaal, A., Gresse, P.G., Scheepers, R. and Le Roux, J.P., 1999. Neoproterozoic to early Cambrian crustal evolution of the Pan-African Saldania belt, South Africa. *Precambrian research*, 97(3-4), pp.303-323.

Rubidge, B. and Hancox, J., 2002. The Karoo supergroup: A geological and palaeontological superlative. *Rocks & Minerals*, *77*(1), pp.54-59.

Scheepers, R., 1995. Geology, geochemistry and petrogenesis of Late Precambrian S-, I-and A-type granitoids in the Saldania belt, Western Cape Province, South Africa. *Journal of African Earth Sciences*, 21(1), pp.35-58.

Scheepers, R. and Schoch, A.E., 2006. The Cape Granite Suite. In: Johnson, M.R., Annhacusser, C.R. and Thomas, R.J. (eds). *The Geology of South Africa*. Geological Society of South Africa. Johannesburg/Council for Geoscience, pp.421-432.

Science first., 2017. Available: https://shop.sciencefirst.com/chemistry/4088-quartz-molecule.html

Selden, P. and Nudds, J., 2012. *Evolution of fossil ecosystems*. Elsevier, London

Shi, C., Shi, Z., Hu, X., Zhao, R. and Chong, L., 2015. A review on alkali-aggregate reactions in alkali-activated mortars/concretes made with alkali-reactive aggregates. *Materials and Structures*, 48, pp.621-628.

Sims I., and Poole, A.B., 2017. *Alkali-Aggregate Reaction in Concrete: A World Review,* CRC Press, USA.

Thomas, A., 2021. Mapping of surface deformation associated with the 5.2 magnitude Stilfontein earthquake of 3 April 2017 using radar interferometry. *The Egyptian Journal of Remote Sensing and Space Science*, 24(1), pp.85-108.

Thomas, RJ, von Brunn, V. and Marshall, C.G.A., 1990. A tectono-sedimentary model for the Dwyka Group in southern Natal, South Africa. *South African Journal of Geology*, *93*(4), pp.809-817.

Tiecher, F., Florindo, R.N., Vieira, G.L., Gomes, M.E., Dal Molin, D.C. and Lermen, R.T., 2018. Influence of the quartz deformation structures for the occurrence of the alkali–silica reaction. *Materials*, 11(9), pp.1692.

Tucker, R. F., Viljoen, R. P., and Viljoen, M. J., 2016. A Review of the Witwatersrand Basin-The World's greatest goldfield. *Episodes Journal of International Geoscience*, 39(2), pp.104-133.

Twiss, R.J. and Moores, E.M., 1992. *Structural geology.* Macmillan. Available https://www.scribd.com/document/554314333/Twiss-and-Moores-structural-geology

Venyite, P., Nemaleu, J.G.D., Kaze, R.C., Tchamba, A.B., Kamseu, E., Melo, U.C. and Leonelli, C., 2022. Alkali-silica reactions in granite-based aggregates: The role of biotite and pyrite. *Construction and Building Materials*, 320, pp.126259.

Villaros, A., 2010. *Petrogenesis of S-type granites: the example of the Cape Granite Suite*. Doctoral dissertation, University of Stellenbosch.

Von Brunn, V., 1996. The Dwyka Group in the northern part of Kwazulu/Natal, South Africa: sedimentation during late Palaeozoic deglaciation. Palaeogeography, Palaeoclimatology, Palaeoecology, 125(1-4), pp.141-163.

Vorster, C., Kramers, J.A.N., Beukes, N.I.C. and Van Niekerk, H., 2016. Detrital zircon U–Pb ages of the Palaeozoic Natal Group and Msikaba Formation, Kwazulu-Natal, South Africa: provenance areas in context of Gondwana. *Geological Magazine*, 153(3), pp.460-486.

Werner, D., Gardei, A., Simon, S. and Meng, B., 2015. Microscopic investigations of building materials affected by alkali–silica reaction. *15th Euroseminar on microscopy applied to building materials*, pp.1-11.

Woodson, R.D., 2009. *Concrete structures: protection, repair, and rehabilitation*. Butterworth-Heinemann.

Wu, H., Pan, J. and Wang, J., 2020. Nano-scale structure and mechanical properties of ASR products under saturated and dry conditions. *Scientific reports*, 10(1), pp.9187.

Yegon, J.J., 2019. *What is Alkali-Silica Reaction in concrete*? HPD Construction. Available: https://www.hpdconsult.com/what-is-alkali-silica-reaction-in-concrete/#:~:text=Alkali-silica%20reaction%20%28ASR%29%20can%20damage%20the%20structural%20integrity,cracks%20to%20form%20or%20existing%20cracks%20to%20open

14. Appendices

Appendix 1: TIMA elemental maps showing concentrations of Ca, Fe, Mg and Na for the shale rock, Figure 4.5.

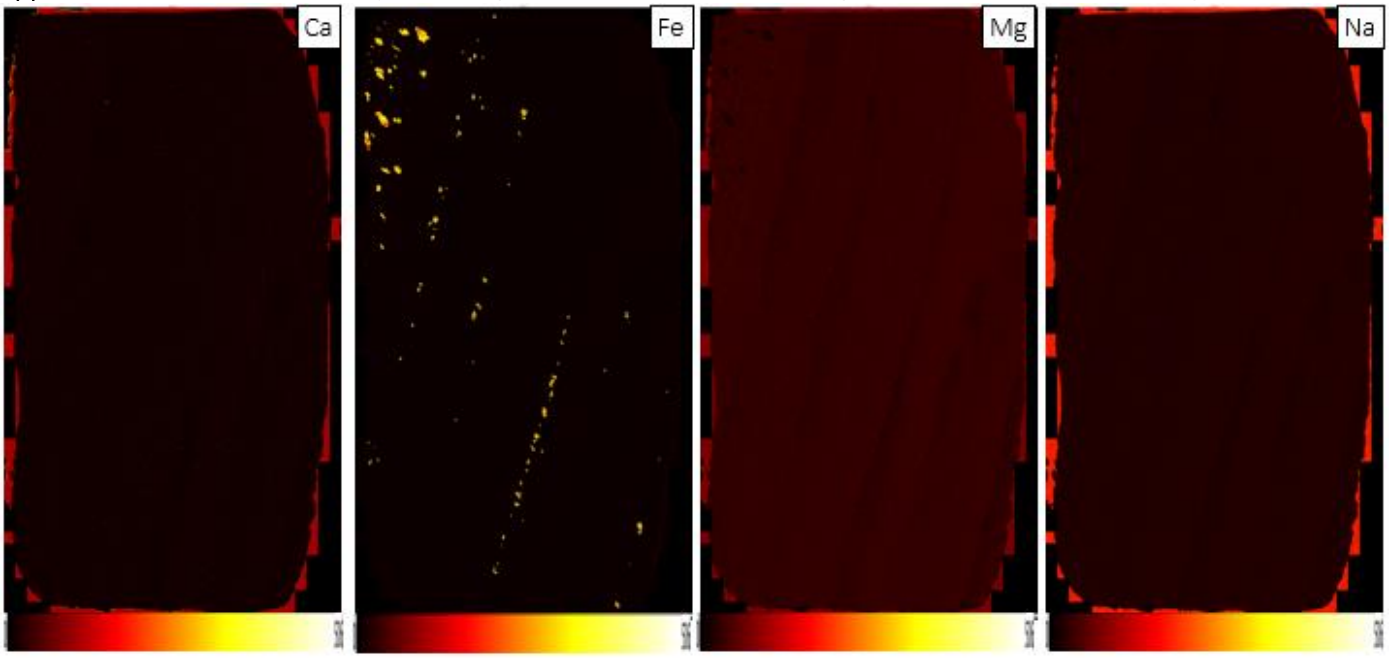

Figure 14.1*: Ca, Mg and Na occur in extremely low concentrations. Fe concentrations are observed to be in high concentrations associated with pyrrhotite domains as seen in Figure 4.5A*

Appendix 2: TIMA elemental maps showing concentrations of Ca, Fe, Mg and S for the quartzite rock, Figure 4.9

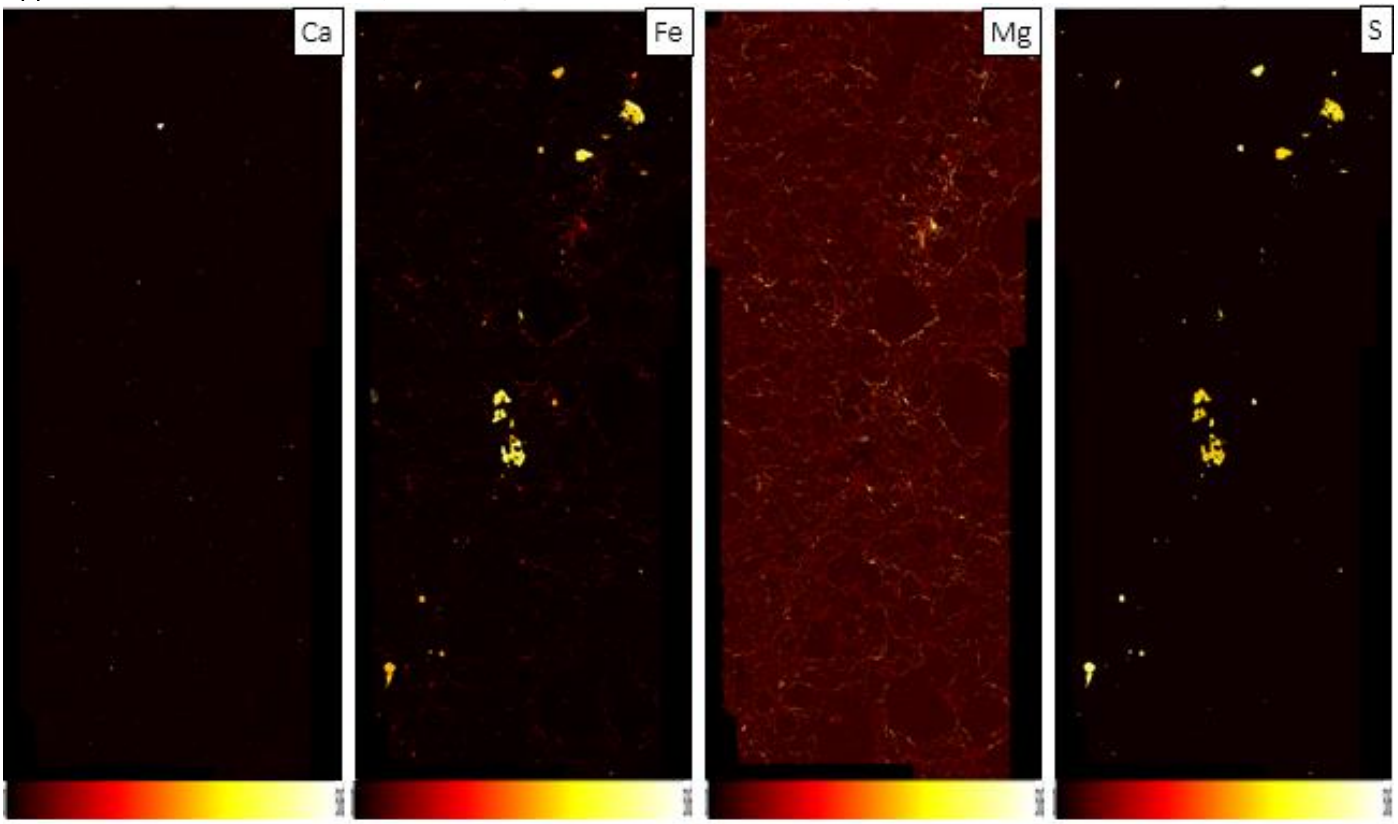

Figure 14.2: Elemental maps show that Ca, Fe, Mg, and S are extremely low concentrations. No Ca content is detected in the rock. High Fe and S concentration are associated with pyrrhotite.

Appendix 3: Mineral phases for rock samples (in wt %) detected by XRD analysis.

Mineral phases	Wits shale	Wits quarzite[1]	Dwyka tillite	Natal sandstone	GCS granite	Malmesbury wacke	Wits quartzite[2]
Quartz	48.5	91.1	49.9	76.4	36.4	57.1	85.4
Plagioclase	0	0	20.4	11.6	29.6	26.5	0
Microcline	.2	0	14.9	9.4	21.0	0	0
Chlorite	0	2.4	10.6	0.8	3.6	0	0
Muscovite	51.3	5.8	0	1.8	9.3	0	14.0
Biotite	0	0	2.1	0	0	11.4	0
Kaolinite	0	0.6	0.7	0	0	0	0
Orthoclase	0	0	0	0	0	4.5	0
Dolomite	0	0	1.4	0	0	0.5	0
Magnetite	0	0	0	0	0	0	0.5

Appendix 4: Primary phases for rock samples (in %) detected by TIMA analysis.

Primary phases	Wits shale	Wits quarzite[1]	Dwyka tillite	Natal sandstone	GCS granite	Malmesbury wacke	Wits quartzite[2]
Quartz	22.90	86.76	22.37	61.42	35.97	45.64	66.36
Muscovite	71.15	9.86	8.29	4.69	3.24	4.98	17.11
Albite	–	–	9.22	1296	2250	1249	–
Orthoclase	0.04	–	4.71	13.16	29.73	5.99	002
Plagioclase	0.02	002	32.14	0.31	3.42	12.69	0.01
Biotite	0.10	0.46	6.24	2.25	1.71	12.56	0.09
Chlorite	–	0.31	2.13	0.29	1.30	0.06	0.08
Calcite	–	–	0.18	1.83	0.04	–	–
Rutile	0.06	0.08	–	0.04	–	–	0.02
Zircon	0.01	0.03	0.02	0.01	0.04	0.04	0.01
Actinolite	–	–	3.39	–	–	–	–
Pumpellyite	0.01	–	2.14	0.07	0.35	0.20	0.01

Kaersutite	–	–	1.49	–	–	0.03	–
Pyrrhotite	0.95	0.73	–	–	–	–	0.02
Titanite	–	–	0.32	–	0.07	0.02	–
Apatite	0.01	0.02	0.06	0.03	–	0.11	0.02
Hematite /Magnetite	–	0.01	0.01	0.12	–	–	–
Pyrope	–	0.14	0.10	0.01	–	–	–
Clay	–	–	0.10	–	0.12	–	–
Pyrite	–	0.24	–	–	–	–	0.08
Diopside	–	–	0.20	–	–	–	–
Ilmenite	–	–	0.01	0.01	0.02	0.14	–
Andradite	–	–	0.18	–	–	–	–
Monazite	0.01	0.02	–	–	–	–	0.01
Hornblende	–	–	0.06	–	0.05	0.06	–
Zoisite	–	–	0.11	–	0.05	–	–
Pentlandite	0.07	–	–	–	–	–	0.01
Grossular	–	–	0.02	0.02	0.05	0.01	–
Chalcopyrite	0.02	–	–	–	–	–	0.01
Ankerite	–	–	0.06	–	–	–	–
Ferro-Actinolite	–	–	0.03	0.01	–	–	–
Allanite-(Ce)	–	–	0.02	–	–	–	–
Kaolinite	0.01	–	–	0.01	–	–	–
Schori	–	0.02	–	0.01	–	0.02	–
Baryte	–	–	–	0.04	–	–	–
Total	**95.37**	**98.73**	**93.64**	**97.31**	**98.73**	**95.07**	**83.87**

1 = Randfontein Formation

2 = Krugersdorp Formation

Appendix 5: Tabulated average expansion results for each aggregate used, showing daily expansion results recorded for over fourteen days with reference point 945.

	SN	UT	CQ	RG*	PG	SQ
Time	Mean %	Mean %	Mean %	Mean %	Mean %	Mean %
D1	0.02	0.01	0.02	0.02	0.01	0.01
D2	0.02	0.02	0.02	0.01	0.02	0.02
D3	0.04	0.02	0.02	0.02	0.02	0.02
D4	0.05	0.03	0.02	0.03	0.03	0.04
D5	0.06	0.03	0.03	0.03	0.03	0.03
D6	0.08	0.03	0.02	0.02	0.03	0.05
D7	0.09	0.04	0.03	0.02	0.04	0.05
D8	0.10	0.04	0.03	0.03	0.05	0.06
D9	0.12	0.05	0.03	0.03	0.06	0.06
D10	0.12	0.06	0.04	0.02	0.08	0.07
D11	0.14	0.06	0.03	0.02	0.08	0.08
D12	0.15	0.07	0.04	0.03	0.09	0.09
D13	0.17	0.07	0.05	0.03	0.09	0.09
D14	0.17	0.09	0.06	0.04	0.10	0.10

Appendix 6: Mean, Minimum and Maximum expansion for AMBT results

	SN	*UT*	*CQ*	*RG**	*PG*	*SQ*
days	14	14	14	14	14	14
mean exp (%)	0.09	0.04	0.03	0.02	0.05	0.05
min exp (%)	0.02	0.01	0.02	0.01	0.01	0.01
max exp (%)	0.17	0.09	0.06	0.04	0.10	0.10

* = Temperature was a factor that affected the strain readings and thus affected the results, however, this was rectified in other samples.

Appendix 7: Range and distribution of expansion for AMBT (SANS 6245) results

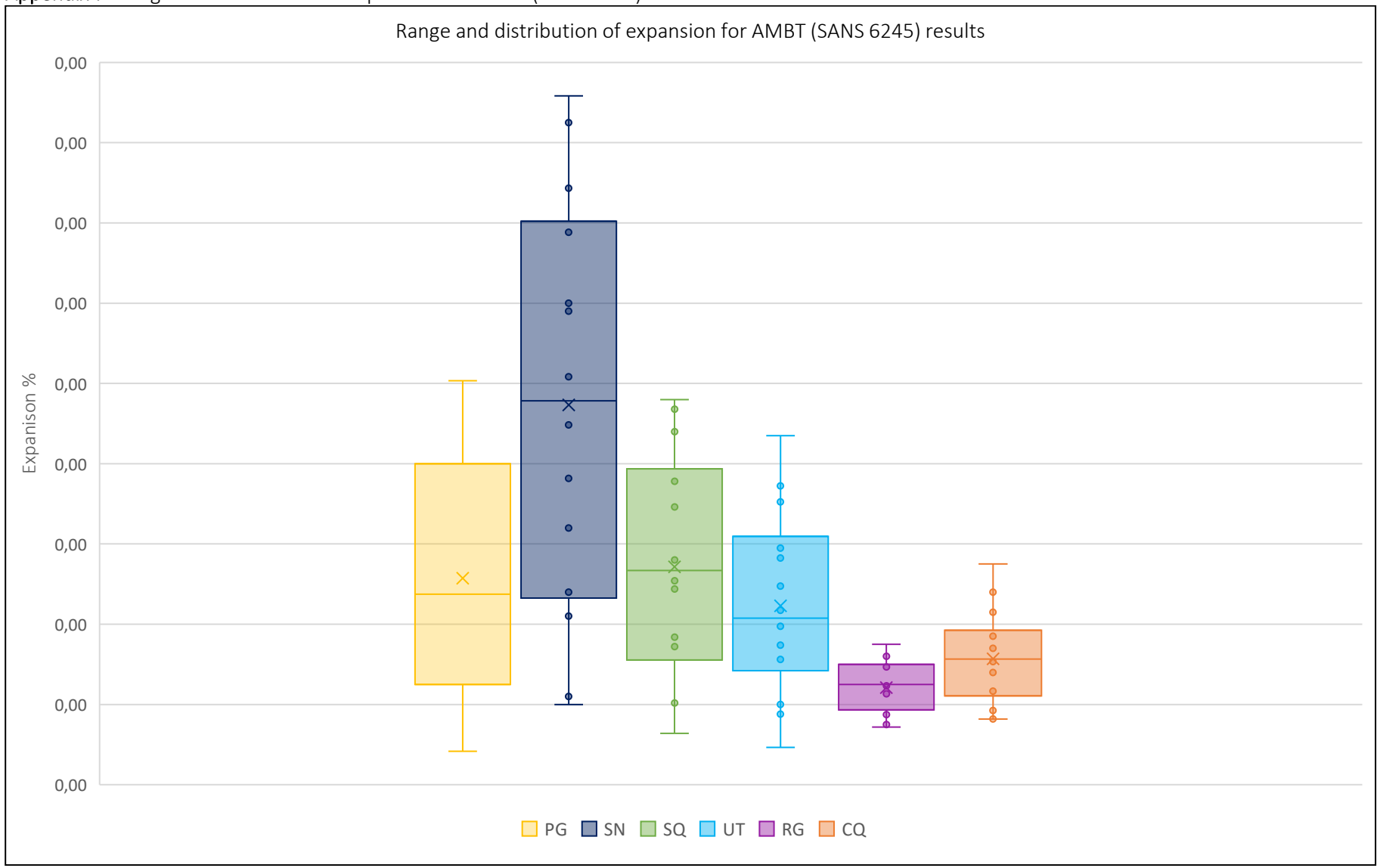

Appendix 8: Petrographic image in XPL with x4 magnification of the tillite rock, Figure 5.3

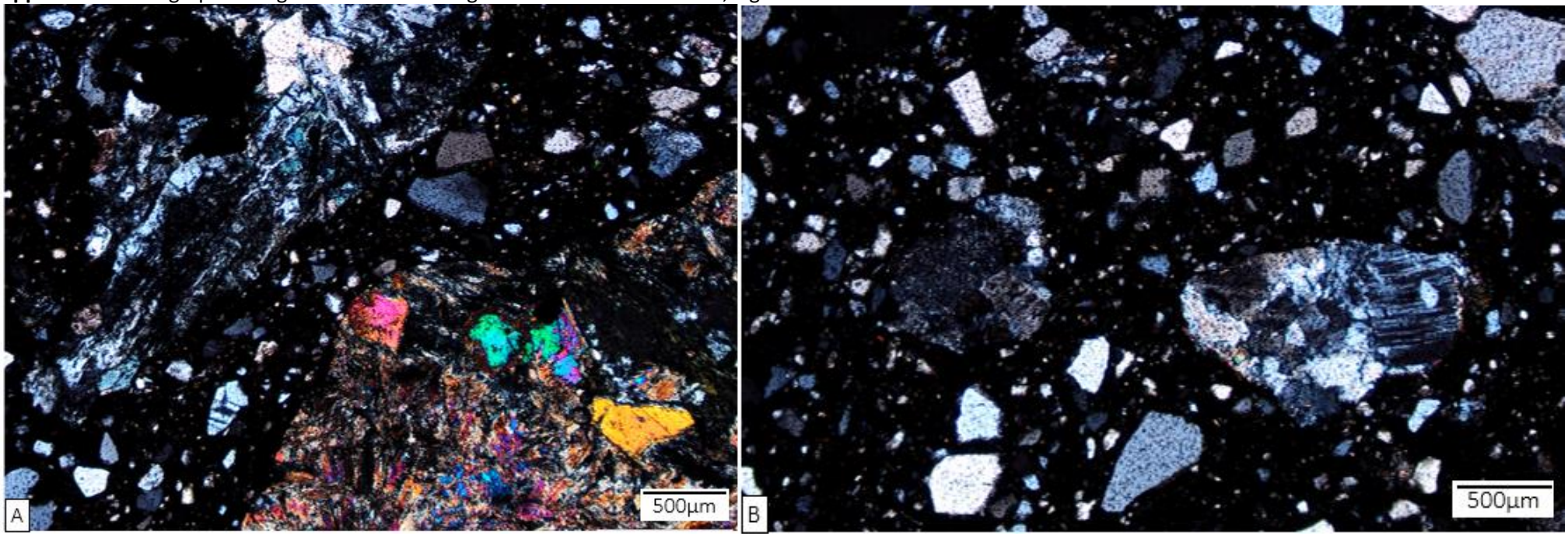

Figure 14.3*: Petrographic image in XPL with x4 magnification of the tillite rock showing lithic fragments of varying composition and with different textures. A) Image shows coarse grained actinolite contains angular muscovite. Crystals are anhedral and angular. B) Image shows plagioclase rich fragments, crystals are subangular*

Appendix 9: TIMA elemental maps showing concentrations of Ca, Fe, Mg, and Na for the tillite rock, Figure 5.4

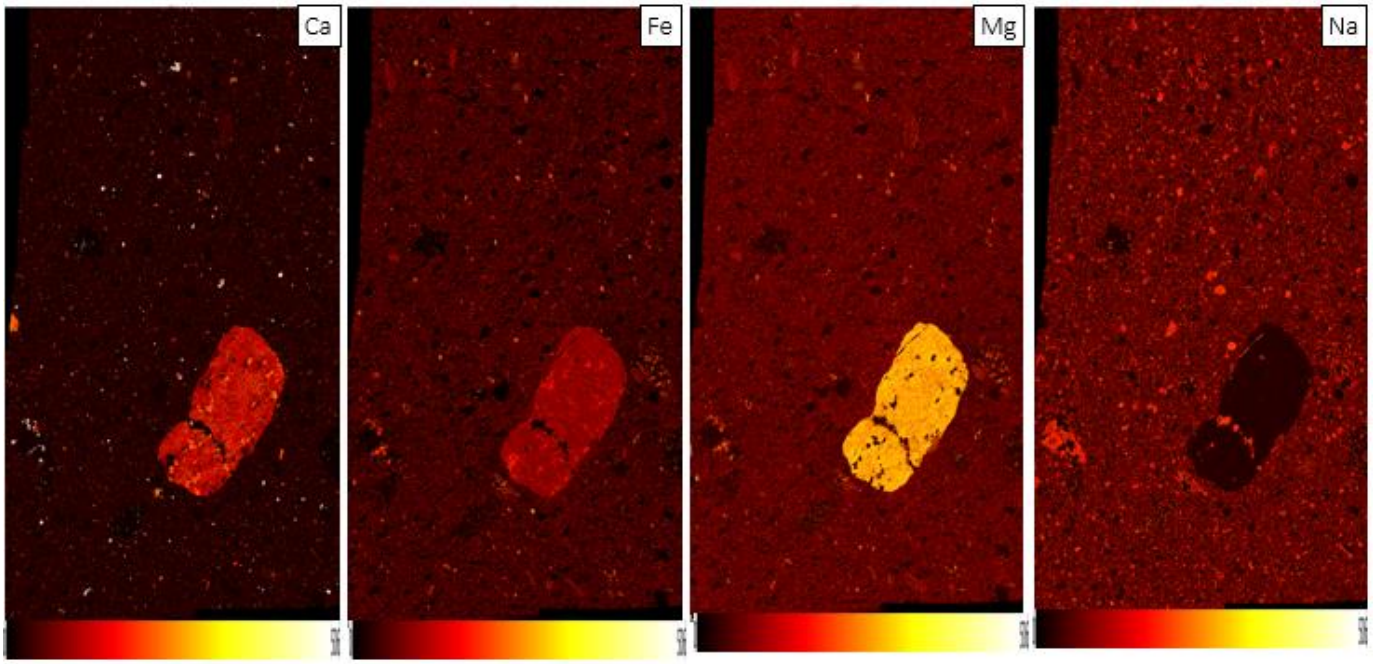

Figure 14.4: Element image showing low concentrations of Ca, Fe, Mg, and Na, however higher Mg concentrations are associated with actinolite.

Appendix 10: TIMA elemental maps showing concentrations of Ca, Fe, Mg, and Na for the Natal rock, Figure 6.5

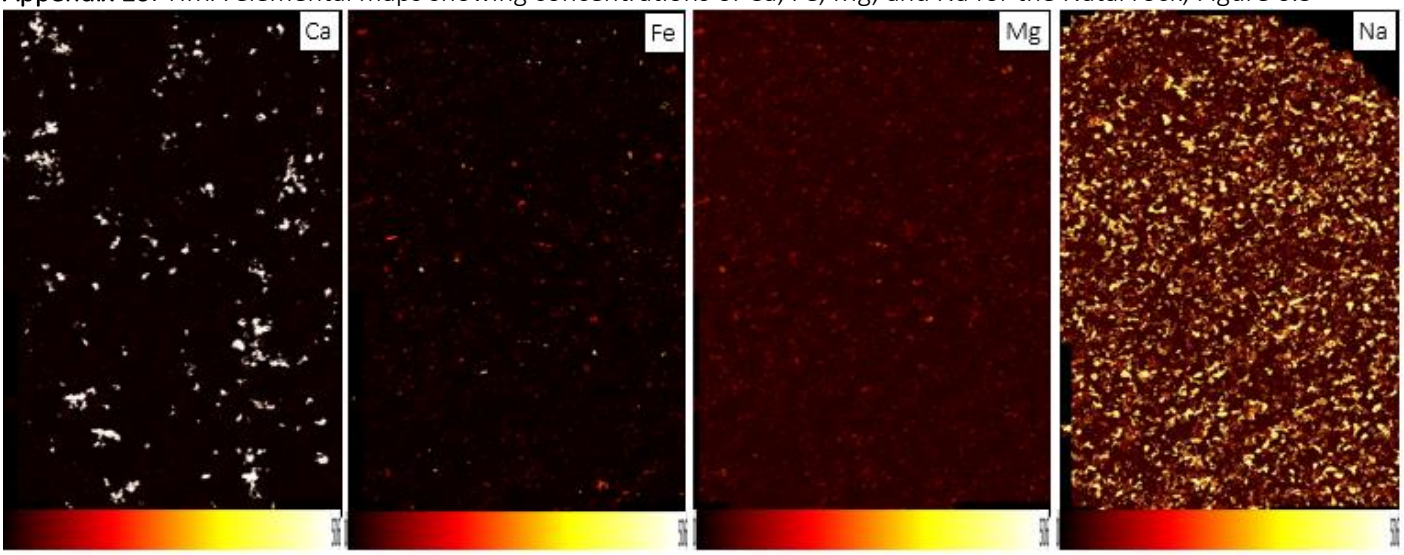

Figure 14.5: Elemental maps showing low concentrations of Fe and Mg. and higher Fe and Na concentrations, associated with albite domains

Appendix 11: Petrographic image of granite, in XPL, with x4 magnification, Figure 7.4

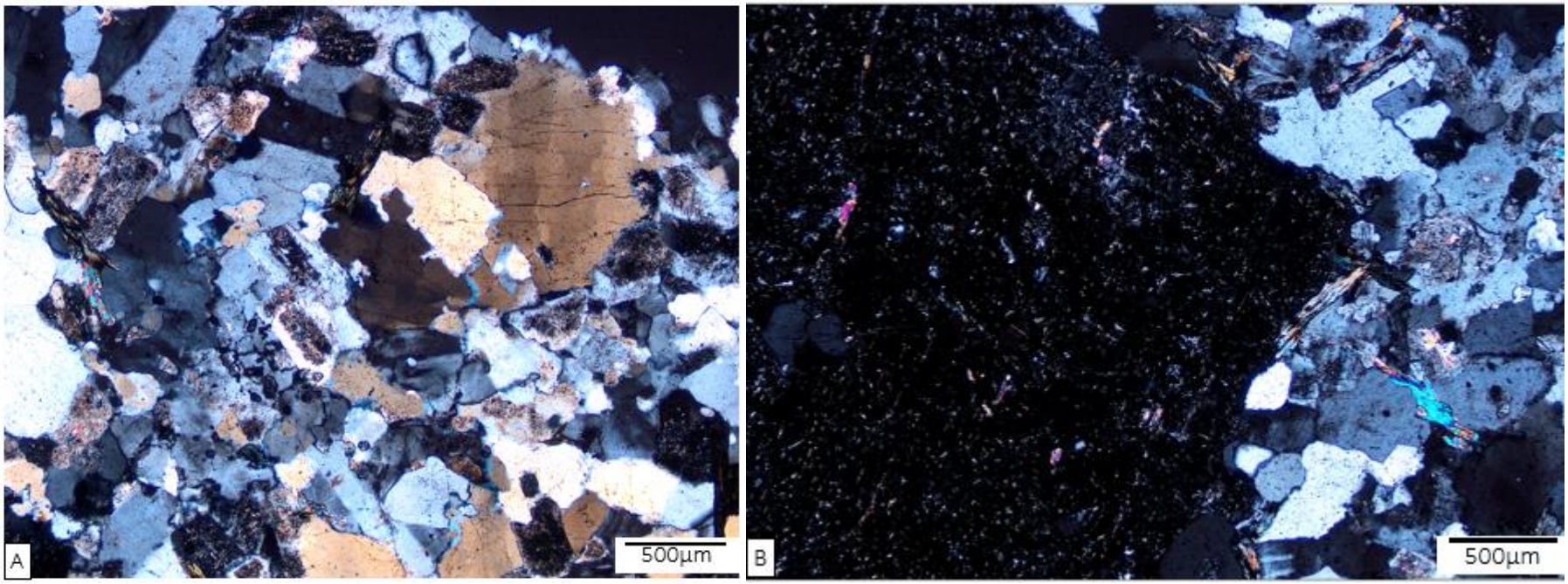

Figure 14.6: *Microscopic image of granite in XPL. A) Image reveals weak undulose extinction of quartz and microscopic material in interstitial spaces. B) Image showing microscopic material and well developed interlocking quartz, plagioclase, albite and muscovite crystals.*

Appendix 12: TIMA elemental maps showing concentrations of Ca, Fe, Mg, and Na for the granite, Figure 7.5

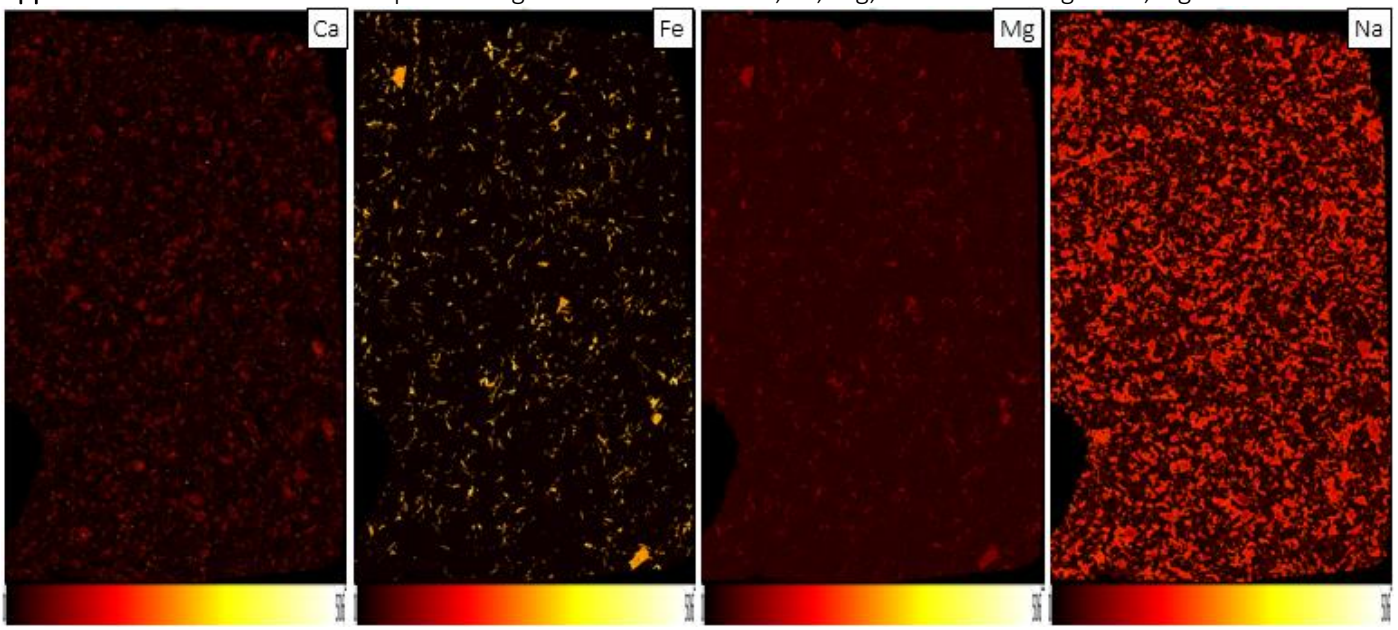

Figure 14.7: Elemental maps showing low extremely low to low concentration of Ca, Mg and Na. Fe occurs as high concentrations associated to biotite domains. Na's low concentrations are associated to albite.

Appendix 13: TIMA elemental maps showing concentrations of Ca, Fe, Mg, and Na for the wacke, Figure 8.4

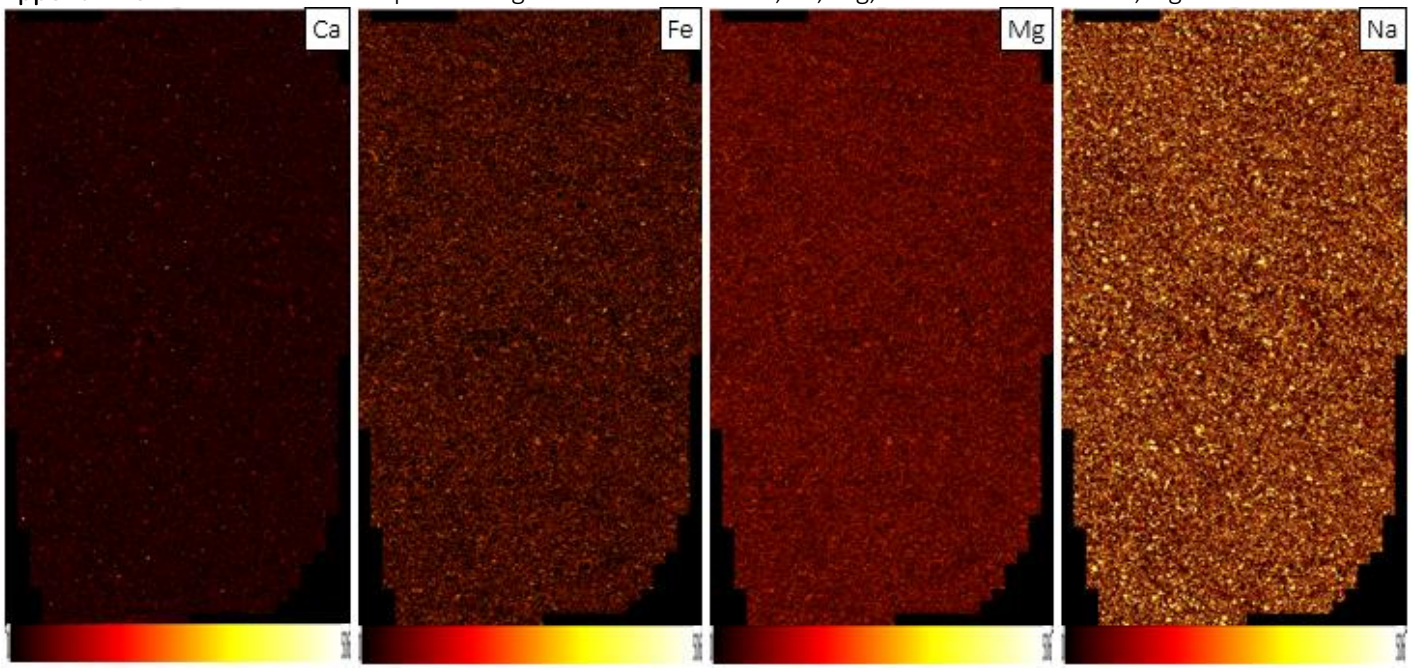

Figure 14.8: Elemental maps reveal low concentrations of Ca, Fe, and Mg. Na occurs in higher concentrations associated with feldspars

Appendix 14: TIMA elemental maps showing concentrations of Ca, Fe, Mg, and Na for the Krugersdorp quartzite, Figure 9.4

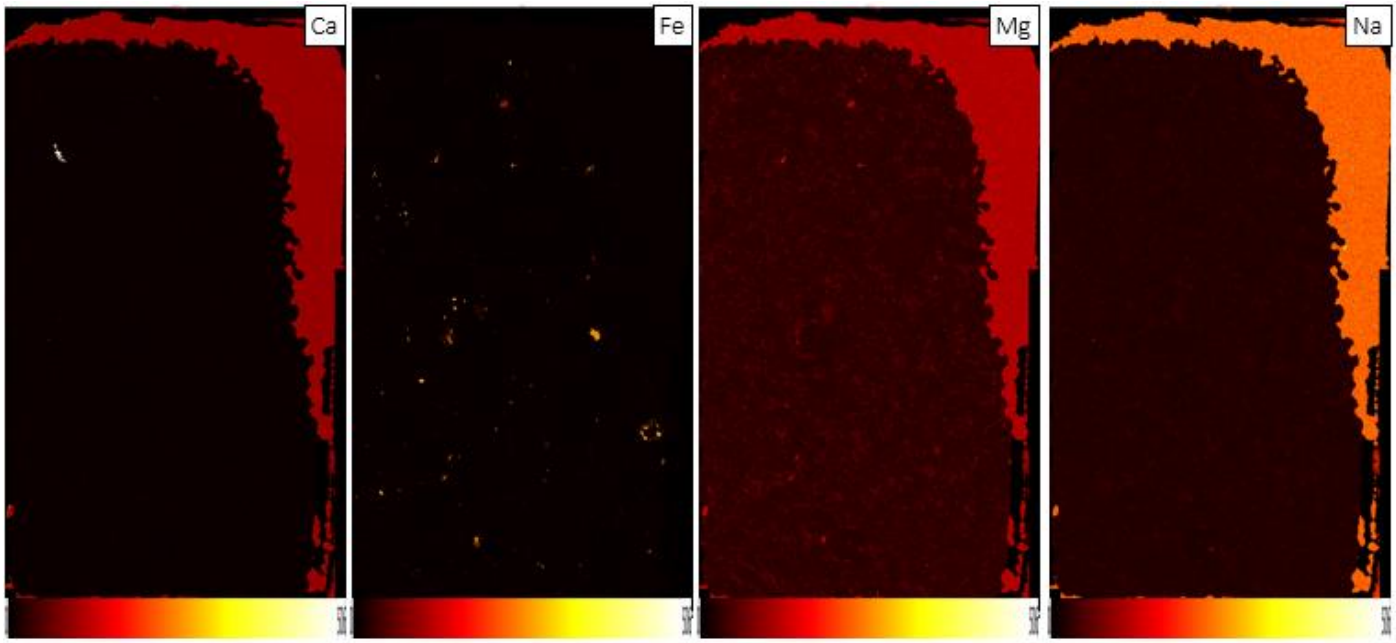

Figure 14.9*: Elemental maps reveal that Ca, Fe, Mg, and Na occurs in extremely low concentrations. No Ca content is detected, and Fe's higher content is associated with pyrite and pyrrhotite.*

Appendix 15: Tabulated results for XRD analysis showing the XRD peaks for quartz for each rock.

Rock	*XRD peaks for quartz*
Micaceous metashale (Wits- Booysens Formation)	24.2; 31; 42.8; 46.1; 47; 58.9; 64.7; 65.1 and 70.8
Quartzite (Wits-Randfontein Formation)	24.2; 31; 42.8; 46.1; 47; 58.9; 64.7; 65.1 and 70.8
Tillite (-Dwyka Group)	24.2; 31; 42.8; 46.1; 47; 58.9; 64.7; 65.1 and 70.8
Arkosic sandstone (Natal Group)	24.2; 31; 42.8; 46.1; 47; 58.9; 64.7; 65.1 and 70.8
Monzogranite (CGS)	24.2; 31; 42.8; 46.1; 47; 58.9; 64.7; 65.1 and 70.8
Wacke (Malmesbury Group)	24.2; 31; 42.8; 46.1; 47; 58.9; 64.7; 65.1 and 70.8
Quartzite (Wits-Krugersdorp Formation)	24.2; 31; 42.8; 46.1; 47; 58.9; 64.7; 65.1 and 70.8